Supporting Information

Investigation of the dynamic behavior of metallopolymers by combined experimental and theoretical methods

Milena Jäger,[a,b] Michael Freduah Agyemang,[c,d,e] Wanja T. Schulze,[c] Julian Kimmig,[a,b] Thomas Bätz,[a,b] Stefan Zechel,[a,b,g,h] Alexander Croy,[c,] Michael Schmitt,[c,d] Juergen Popp,[c,d,e] Stefanie Gräfe,[c,d,f] Martin D. Hager,*[a,b,g,h] Ulrich S. Schubert*[a,b,d,g,h]

[a] M. Jäger, J. Kimmig, T. Bätz, S. Zechel, M. D. Hager, U. S. Schubert
Laboratory of Organic and Macromolecular Chemistry (IOMC)
Friedrich Schiller University Jena
Humboldtstr. 10, 07743 Jena, Germany
E-mail: ulrich.schubert@uni-jena.de; martin.hager@uni-jena.de

[b] M. Jäger, J. Kimmig, T. Bätz, S. Zechel, M. D. Hager, U. S. Schubert
Jena Center for Soft Matter (JCSM)
Friedrich Schiller University Jena
Philosophenweg 7, 07743 Jena, Germany

[c] M. F. Agyemang, W. Schulze, A. Croy, M. Schmitt, J. Popp, S. Gräfe
Institute of Physical Chemistry (IPC)
Friedrich Schiller University Jena
Helmholzweg 4, 07743 Jena, Germany

[d] M. F. Agyemang, M. Schmitt, J. Popp, S. Gräfe, U. S. Schubert
Abbe Center of Photonics (ACP)
Friedrich Schiller University Jena
Albert-Einstein-Straße 6, 07745 Jena, Germany

[e] M. F. Agyemang, J. Popp
Leibniz Institute of Photonic Technology
Friedrich Schiller University Jena
Albert-Einstein-Straße 9, 07745 Jena, Germany

[f] S. Gräfe
Fraunhofer Institute for Applied Optics and Precision Engineering
Friedrich Schiller University Jena
Albert-Einstein-Straße 7, 07745 Jena, Germany

[g] S. Zechel, M. D. Hager, U. S. Schubert
Helmholtz-Institute for Polymers in Energy Applications Jena (HIPOLE Jena)
Lessingstr. 12-14, 07443 Jena, Germany

[h] S. Zechel, M. D. Hager, U. S. Schubert
Helmholtz Zentrum Berlin für Materialien und Energie (HZB)
Hahn-Meitner-Platz 1, 14109 Berlin, Germany

Table of contents

1 Materials and methods

All chemicals and solvents used were purchased from Acros Organics, Sigma-Aldrich, HetCat, Molekula and TCI, and if not mentioned used without further purification. Methyl methacrylate (MMA), butyl methacrylate (BMA) and 2-ethyl hexyl methacrylate (2-EHMA) were destabilized over an AlOx column (neutral AlOx). The terpyridine monomer (6-(2,2':6',2''-terpyridin-4'-yloxy)-hexyl-methacrylate; Tpy-MA) was synthesized according to a literature procedure.[1]

Column chromatography was carried out with neutral aluminum oxide (AlOx) from Molekula. The reactions were controlled by using thin-layer chromatography (aluminum sheets coated with neutral aluminum oxide 60 F_{254} by Merck).

^{1}H NMR-spectra were recorded on a Bruker AC 300 (300 MHz) spectrometer at 298 K. The chemical shift is given in parts per million (ppm on δ Scale) related to deuterated solvent.

Size exclusion chromatography (SEC) was performed with a setup consisting of a Shimadzu CBM-20A system controller, a DGU-14A degasser, a LC-20AD pump, a SIL-20AHT auto sampler, a CTO-10AC vp oven, an SPD-20A UV-detector, a RID-10A RI-detector and PSS SDV guard/1,000 Å/1,000,000 Å (5 µm particle size) columns using a chloroform, isopropanol and triethylamine eluent [94/2/4] with 1 mL min^{-1} at 40 °C and a poly (methyl methacrylate) standard.

Elemental analysis was carried out at the Vario El III (Elementar) elemental analyzer.

The thermogravimetric analysis (TGA) was carried out under a nitrogen atmosphere with a heating rate of 20 K min^{-1} on a Netzsch TG 209 F1 Iris.

Differential scanning calorimetry (DSC) was performed under a nitrogen atmosphere using a DSC 204 F1 Phoenix by Netzsch with a heating rate of 20 K min^{-1} for the first and second cycle and of 10 K min^{-1} for the third cycle.

The DSC and TGA results were evaluated with NETZSCH-Proteus-80 software.

Rheology measurements were performed according to literature[2–4] utilizing a MCR 301 rheometer from Anton Paar using the convection oven device CTD 450. The samples were measured with a solid rectangular fixture setup (SRF12-SN13529, Anton Paar) in dimensions of approximately 18 × 10 mm (length, width) and a thickness of around 3 mm. The resulting sample gap was set to 18 mm. The software RheoCompassTM V1.24.549-Release 64 bit (Anton Paar) was applied for operating the rheometer as well as the analysis. The data was exported as txt-files and evaluated with the OriginPro 2024b software.

2 Synthesis of the model complexes

The monomer Tpy-MA was dissolved in dichloromethane (2 mL). The metal salts were dissolved in methanol (0.5 mL) and combined with the monomer solution. The solvents were removed under vacuum. Subsequently, the model complexes were dried at 40 °C for 24 h under vacuum. The quantities of all substances are summarized in **Table S1**.

Table S1. Utilized masses for the synthesis of the model complexes **$[(Tpy)_2Fe]^{2+}$** and **$[(Tpy)_2Zn]^{2+}$**.

Complex	**Monomer**	**m (monomer) [g]**	**n (monomer) [mmol]**	**Metal salt**	**m (metal salt) [mg]**	**n (metal salt) [mmol]**
$[(Tpy)_2Fe]^{2+}$	Tpy-MA	0.314	0.75	$FeSO_4 \times 7\ H_2O$	104.5	0.38
$[(Tpy)_2Zn]^{2+}$	Tpy-MA	0.307	0.74	$Zn(TFMS)_2$	133.7	0.37

3 Synthesis of the polymers

All polymerizations were performed according to the standard procedure in the Schubert group, as also described in literature.[2–5] For all polymers, methyl methacrylate (MMA), butyl methacrylate (BMA) or 2-ethyl hexyl methacrylate (2-EHMA) and 6-(2,2':6',2''-terpyridin-4'-yloxy)-hexyl-methacrylate (Tpy-MA) were dissolved in anhydrous toluene. The initiator azo*bis*isobutyro-nitrile (AIBN) and the reversible addition−fragmentation chain-transfer (RAFT) reagent, 2-cyano-2-propyl benzodithioate (CPDB), were dissolved in anhydrous toluene and added to the reaction mixture. The mixture was degassed with nitrogen for 45 min and, subsequently, stirred for 17 h in a preheated oil bath at 70 °C. All polymers were purified by dialysis (THF, MWCO: 3.5 kDa). The solvent was removed under vacuum. The utilized reactants are summarized in **Table S2**. The polymers were characterized *via* NMR-spectroscopy, size-exclusion chromatography (SEC), differential scanning calorimetry (DSC), thermogravimetric analysis (TGA) and elemental analysis. The results are depicted in **Figure S1-S6** and are summarized in **Table S3**.

Table S2. Utilized masses and volumes for the synthesis of the polymers **P1**, **P2** and **P3**.

Polymer	Monomers	m (monomers) [g]	n (monomers) [mmol]	m (CPDB) [mg]	n (CPDB) [mmol]	m (AIBN) [mg]	n (AIBN) [mmol]	V (toluene) [mL]
P1	MMA Tpy-MA	10.00 4.59	99.88 10.99	196	0.89	36.4	0.22	111
P2	BMA Tpy-MA	10.00 2.94	70.32 7.03	137	0.62	25.4	0.15	77
P3	2-EHMA Tpy-MA	10.00 2.32	50.43 5.55	99	0.45	18.4	0.11	56

Table S3. Summary of the calculated composition, the determined molar masses and dispersities, the elemental composition and thermal properties of the polymers **P1-P3**.

Polymer	Tpy content [%][(a)]	SEC[(b)]			Elemental analysis					T_d[(c)] [°C]	T_g[(d)] [°C]
		M_n [g/mol]	M_w [g/mol]	Đ		C [%]	H [%]	N [%]	S [%]		
P1	9.3	12,500	15,100	1.21	calc.	63.56	7.59	3.02	-	167	76
					found	63.06	7.73	2.95	-		
P2	9.1	13,300	15,300	1.15	calc.	68.56	9.15	2.28	-	238	25
					found	65.82	8.82	2.17	-		
P3	9.4	23,500	26,300	1.12	calc.	72.55	10.35	1.80	-	298	3
					found	72.40	10.60	1.80	-		

(a) Determined *via* NMR spectroscopy (in CD_2Cl_2 at 300 MHz).
(b) Eluent: $CHCl_3$/NEt_3/*i*-PrOH (94/4/2), PMMA standard.
(c) Degradation temperatures determined *via* TGA measurements: 25 to 600 °C, 20 K min^{-1}, nitrogen atmosphere.
(d) Glass transition temperatures determined *via* DSC measurements: -110 to 150 °C, 3rd heating run, 10 K min^{-1}, nitrogen atmosphere.

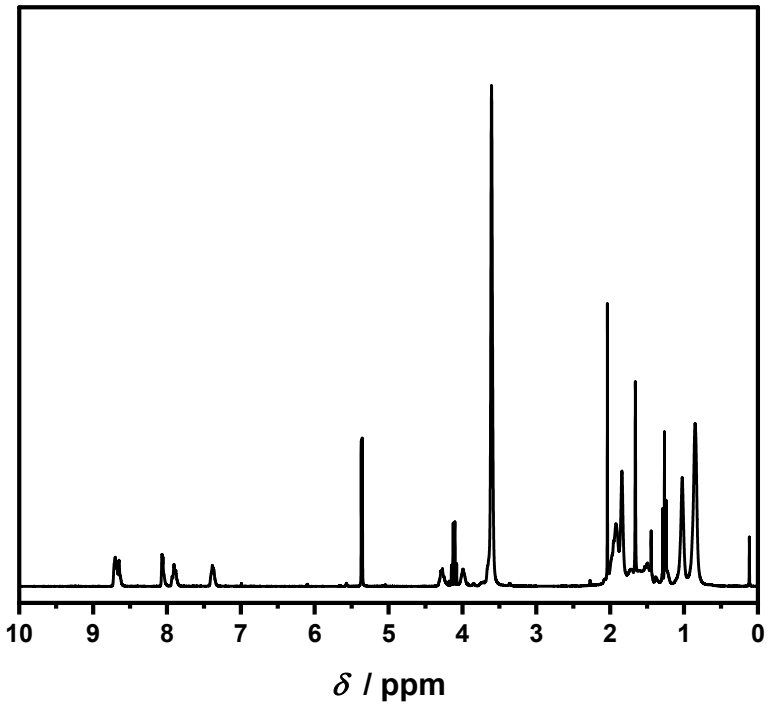

Figure S1. ^{1}H NMR spectrum of **P1** in CD_2Cl_2 at 300 MHz.

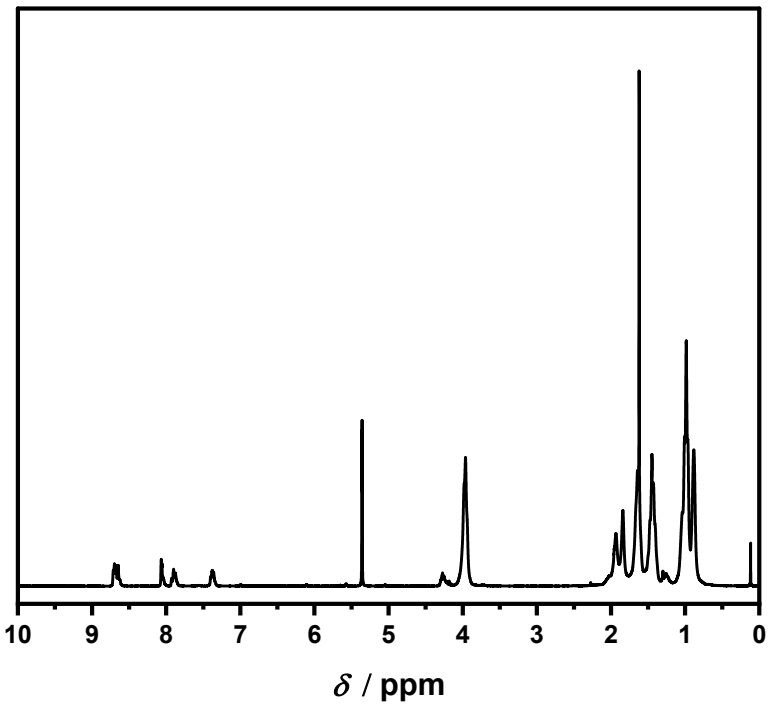

Figure S2. ^{1}H NMR spectrum of **P2** in CD_2Cl_2 at 300 MHz.

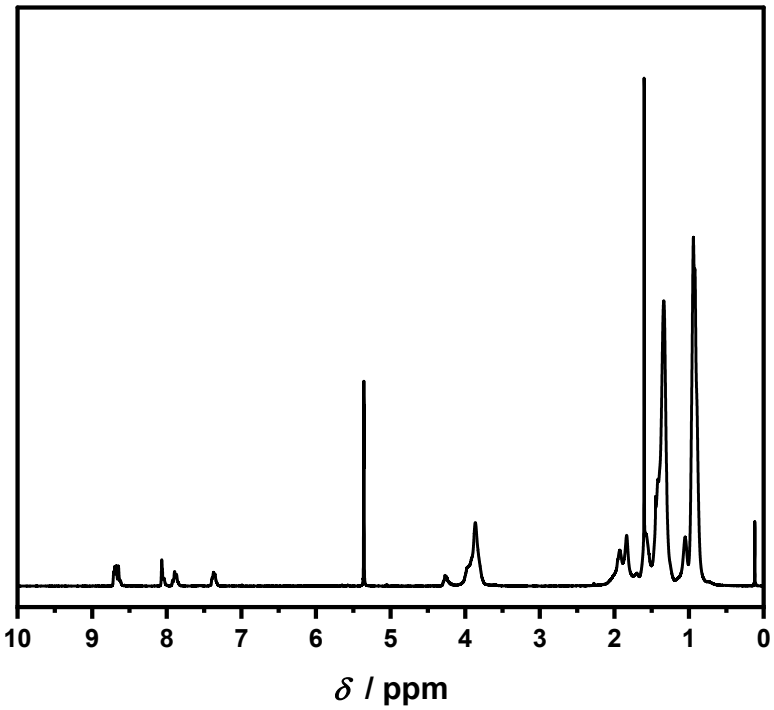

Figure S3. ^{1}H NMR spectrum of **P3** in CD_2Cl_2 at 300 MHz.

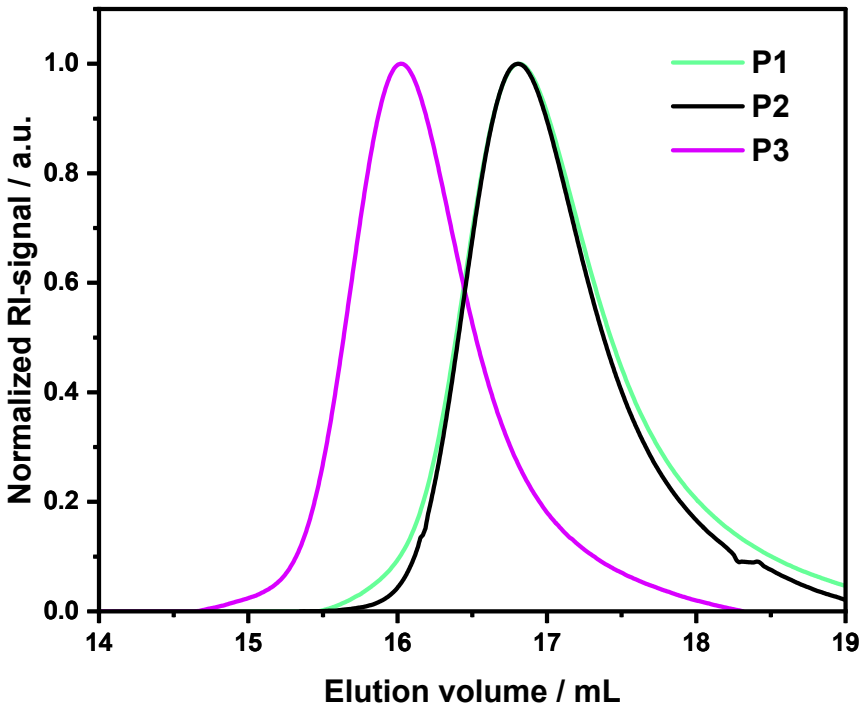

Figure S4. SEC-curves of the polymers **P1**-**P3** (eluent: $CHCl_3$/NEt_3/*iso*-propanol, 94:4:2, calibration standard: PMMA).

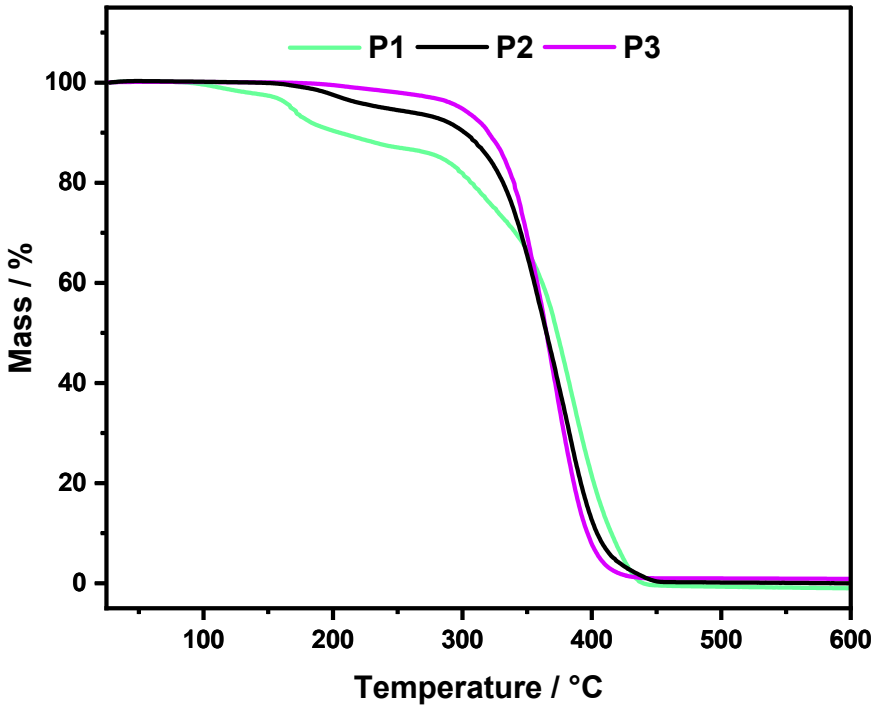

Figure S5. TGA-curves of the polymers **P1-P3** (20 K min^{-1}, nitrogen atmosphere).

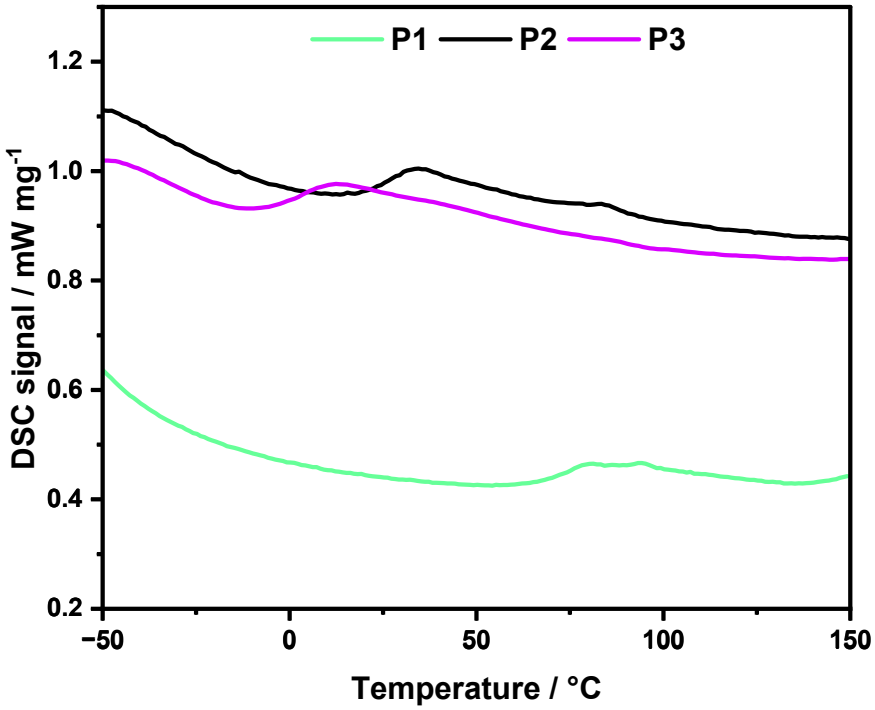

Figure S6. DSC-curves of the polymers **P1-P3** (3rd heating run, 10 K min^{-1}, nitrogen atmosphere).

For the synthesis of poly(methyl methacrylate) (**PMMA**), free radical polymerization (FRP) was used, which was adapted from the standard RAFT procedure in our group, as also described in literature.[2–5] Methyl methacrylate (MMA) was dissolved in anhydrous toluene. The initiator azo*bis*isobutyronitrile (AIBN) was dissolved in anhydrous toluene and added to the reaction mixture. The mixture was degassed with nitrogen for 45 min and, subsequently, stirred for 17 h in a preheated oil bath at 70 °C. Afterwards, the crude product was precipitated in methanol. The polymer was then separated, washed with methanol and dried in a vacuum oven at 50 °C for 24 h. The utilized reactants are summarized in **Table S4**.

Table S4. Utilized masses and volumes for the synthesis of the polymer **PMMA**.

Polymer	**Monomer**	**m (monomer) [g]**	**n (monomer) [mmol]**	**m (AIBN) [mg]**	**n (AIBN) [mmol]**	**V (toluene) [mL]**
PMMA	MMA	10.00	99.88	136.7	0.83	50

4 Synthesis of the metallopolymers

All metallopolymers were synthesized according to the standard procedure in our group, as also described in literature.[2,6,7] The respective polymer (**P1**, **P2** or **P3**) was dissolved in dichloromethane (6 mL). The metal salt was dissolved in methanol (1 mL) and combined with the polymer solution. The solvents were removed under vacuum. Subsequently, the metallopolymers were washed with methanol and dried at 40 °C for 48 h under vacuum. The quantities of all substances are summarized in **Table S5**. The resulting metallopolymers (MP) were characterized *via* TGA, DSC and elemental analysis. The results are shown in **Figure S7** to **S12** and **Table S6**.

Table S5. Utilized masses and volumes for the synthesis of the metallopolymers **P1-Fe** to **P3-Zn**.

Polymer	MP	m (polymer) [g]	Metal salt	m (metal salt) [mg]	n (metal salt) [mmol]
P1	**P1-Fe**	2.002	$FeSO_4 \times 7\ H_2O$	200	0.718
	P1-Zn	2.008	$Zn(TFMS)_2$	262	0.720
P2	**P2-Fe**	2.00	$FeSO_4 \times 7\ H_2O$	151	0.544
	P2-Zn	2.001	$Zn(TFMS)_2$	198	0.544
P3	**P3-Fe**	2.002	$FeSO_4 \times 7\ H_2O$	119	0.428
	P3-Zn	2.001	$Zn(TFMS)_2$	156	0.428

Table S6. Summary of the elemental analysis and thermal properties of the metallopolymers **P1-Fe** to **P3-Zn**.

MP	Elemental analysis					T_d[(a)] [°C]	T_g[(b)] [°C]
		C [%]	H [%]	N [%]	S [%]		
P1-Fe	calc.	57.80	7.37	2.74	1.06	148	108
	found	52.57	6.49	2.48	0.97		
P1-Zn	calc.	57.57	6.79	2.69	2.06	162	121
	found	51.27	6.22	2.40	2.18		
P2-Fe	calc.	63.74	8.86	2.12	0.81	210	50
	found	63.96	8.78	2.17	0.87		
P2-Zn	calc.	63.49	8.39	2.10	1.60	215	89
	found	61.97	8.39	2.05	1.76		
P3-Fe	calc.	68.47	10.05	1.70	0.65	223	50
	found	71.53	10.37	1.73	0.29		
P3-Zn	calc.	68.22	9.66	1.68	1.28	268	71
	found	65.45	9.55	1.59	1.51		

(a) Degradation temperatures determined *via* TGA measurements: 25 to 600 °C, 20 K min^{-1}, nitrogen atmosphere.
(b) Glass transition temperatures determined *via* DMTA: 25 to 100, 130 or 150 °C, 2 K min^{-1}, 1 Hz.

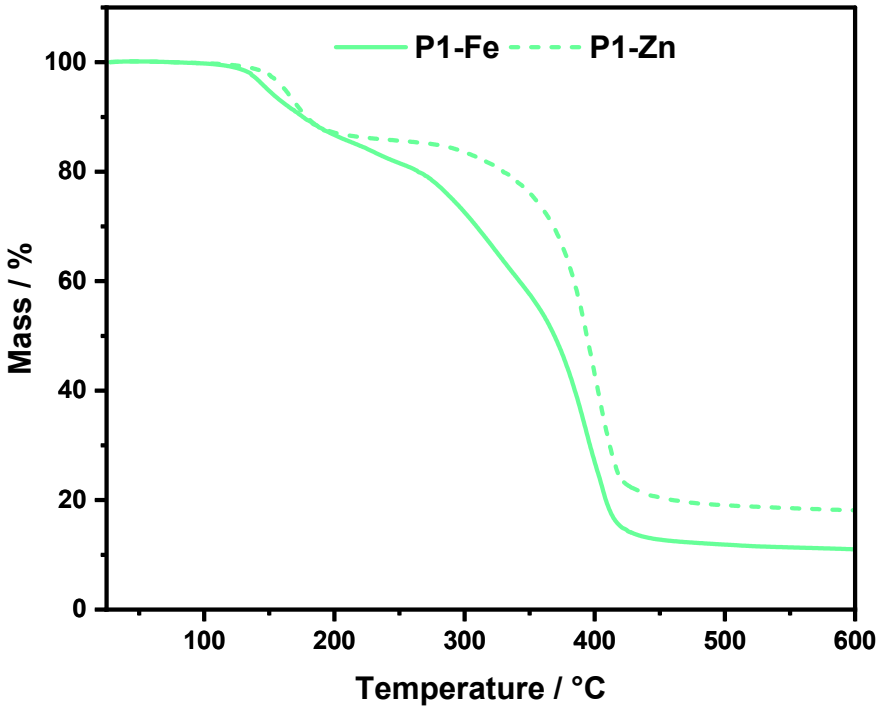

Figure S7. TGA-curves of the metallopolymers **P1-Fe** and **P1-Zn** (20 K min^{-1}, nitrogen atmosphere).

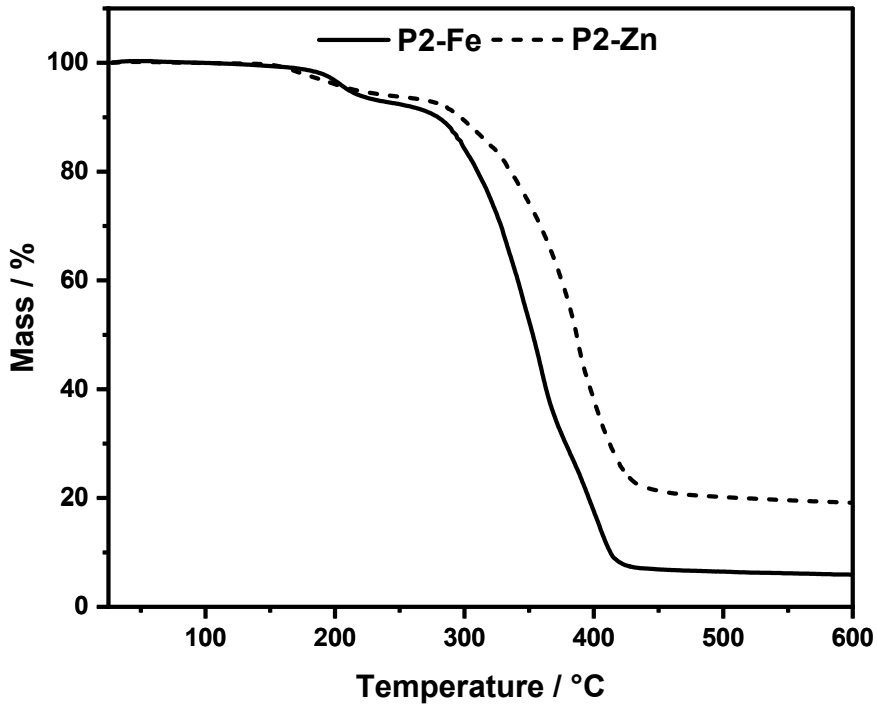

Figure S8. TGA-curves of the metallopolymers **P2-Fe** and **P2-Zn** (20 K min^{-1}, nitrogen atmosphere).

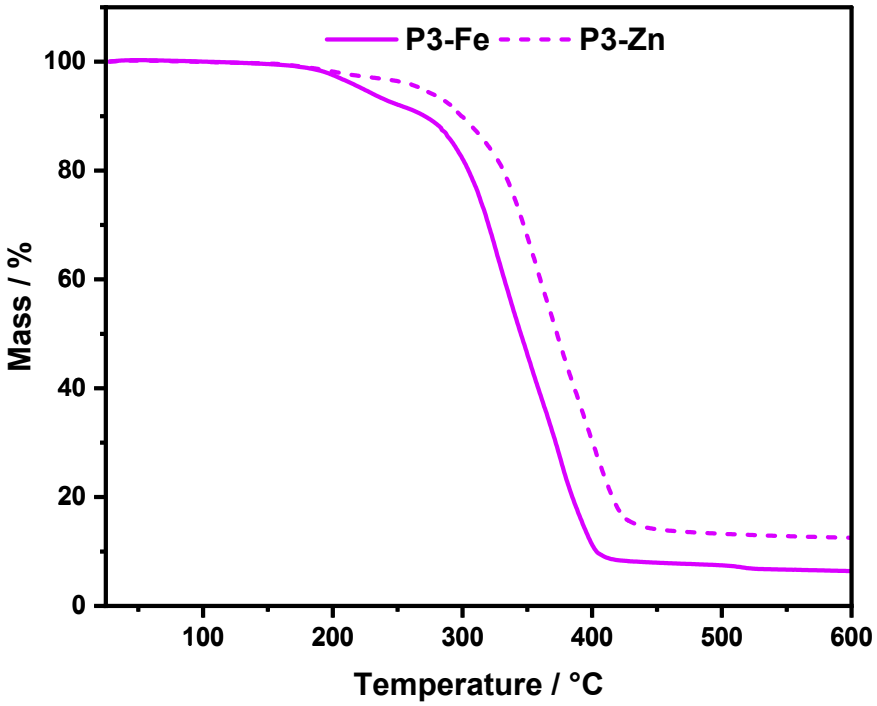

Figure S9. TGA-curves of the metallopolymers **P3-Fe** and **P3-Zn** (20 K min^{-1}, nitrogen atmosphere).

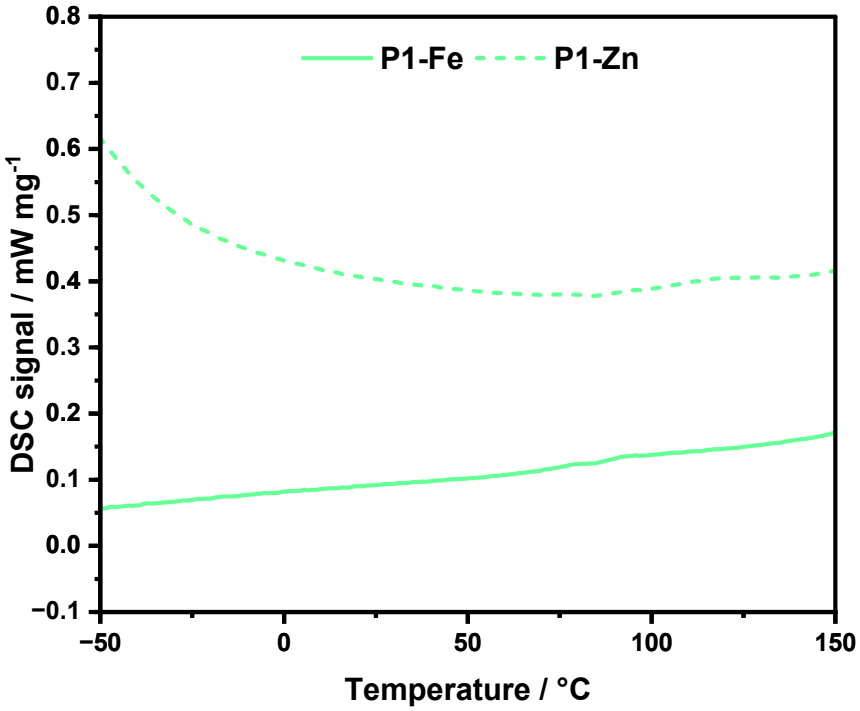

Figure S10. DSC-curves of the metallopolymers **P1-Fe** and **P1-Zn** (3rd heating run, 10 K min^{-1}, nitrogen atmosphere).

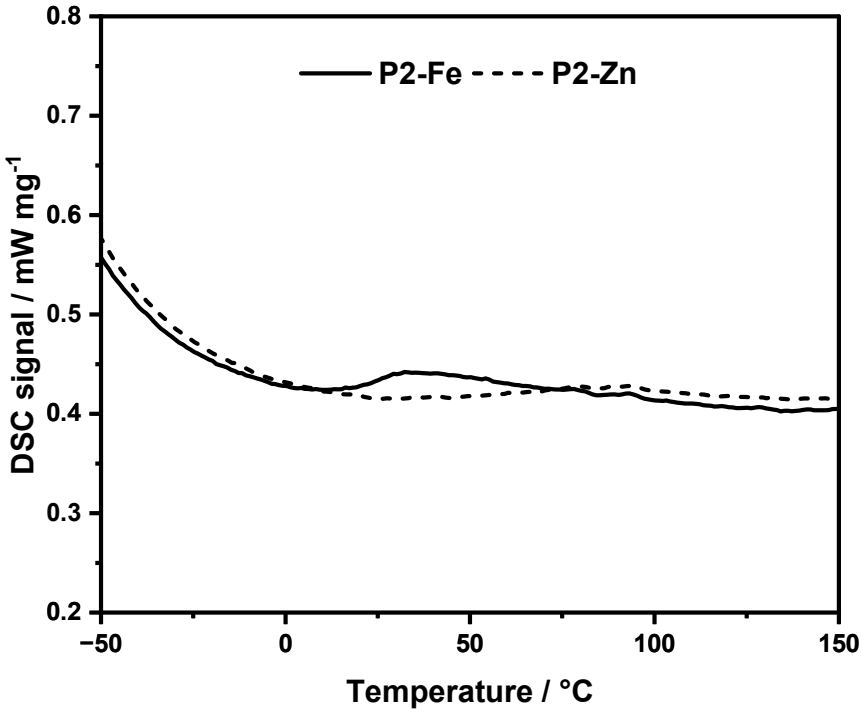

Figure S11. DSC-curves of the metallopolymers **P2-Fe** and **P2-Zn** (3rd heating run, 10 K min^{-1}, nitrogen atmosphere).

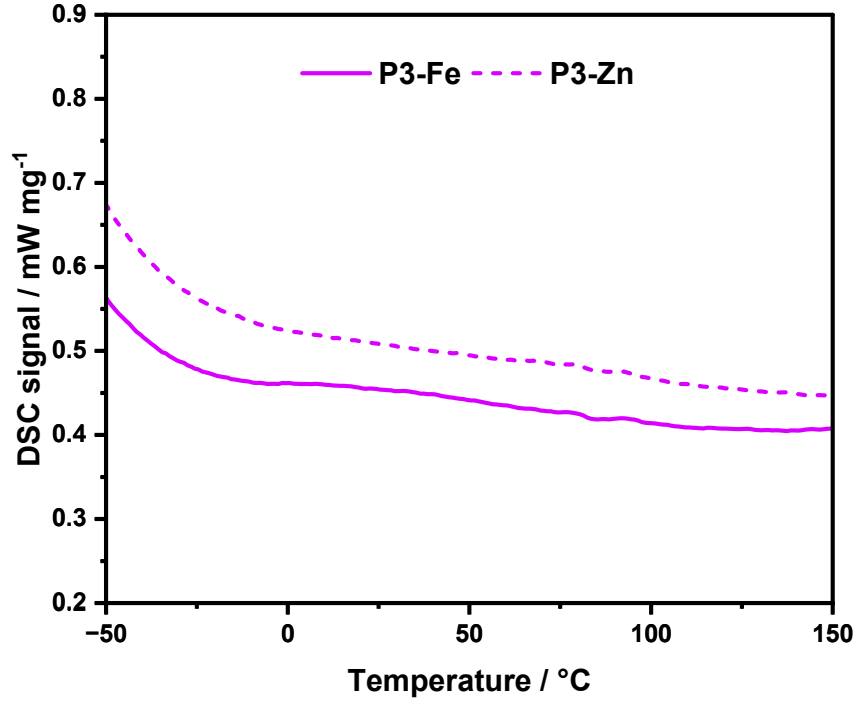

Figure S12. DSC-curves of the metallopolymers **P3-Fe** and **P3-Zn** (3rd heating run, 10 K min^{-1}, nitrogen atmosphere).

5 Synthesis of the covalent-crosslinked polymer networks

For the synthesis of the covalent-crosslinked polymer networks, free radical polymerization (FRP) was used**,** which was adapted from the standard RAFT procedure in the Schubert group, as also described in literature.[2–5] For all polymer networks, methyl methacrylate (MMA), butyl methacrylate (BMA) or 2-ethyl hexyl methacrylate (2-EHMA) and 1,6-hexanediol dimethacrylate (HDMA) were dissolved in anhydrous toluene. The initiator AIBN was dissolved in anhydrous toluene and added to the reaction mixture. The mixture was degassed with nitrogen for 45 min and, subsequently, stirred for 17 h in a preheated oil bath at 70 °C. The solvent was removed under vacuum, and the polymers were washed with water, acetone and chloroform. The utilized reactants are summarized in **Table S7**. The polymers were characterized *via* DSC, TGA and elemental analysis. The results are depicted in **Figure S13-S14** and **Table S8**.

Table S7. Utilized masses and volumes for the synthesis of the polymer networks **P4**, **P5** and **P6**.

Polymer	Monomers	m (monomers) [g]	n (monomers) [mmol]	m (AIBN) [mg]	n (AIBN) [mmol]	V (toluene) [mL]
P1-cc	MMA HDMA	10.00 1.27	99.88 4.99	143.5	0.87	53
P2-cc	BMA HDMA	10.00 0.89	70.32 3.52	121.3	0.74	37
P3-cc	2-EHMA HDMA	10.00 0.64	50.43 2.52	62.1	0.38	27

Table S8. Summary of the elemental analysis and thermal properties of the polymer networks **P4-P6**.

Polymer	Elemental analysis					T_d[(a)] [°C]	T_g[(b)] [°C]
		C [%]	H [%]	N [%]	S [%]		
P1-cc	calc.	60.71	8.13	-	-	200	71
	found	60.81	7.77	-	-		
P2-cc	calc.	67.45	9.82	-	-	228	36
	found	67.82	9.70	-	-		
P3-cc	calc.	72.27	11.03	-	-	252	10
	found	72.31	10.96	-	-		

(a) Degradation temperatures determined *via* TGA measurements: 25 to 600 °C, 20 K min^{-1}, nitrogen atmosphere.
(b) Glass transition temperatures determined *via* DSC measurements: -110 to 150 °C, 3rd heating run, 10 K min^{-1}, nitrogen atmosphere.

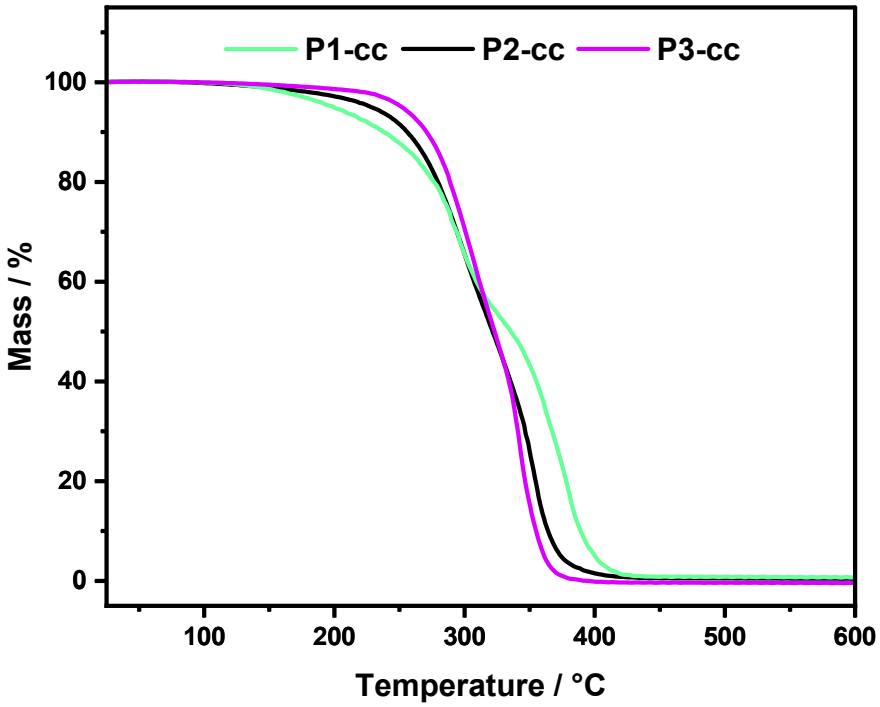

Figure S13. TGA-curves of the polymers **P1-cc** to **P3-cc** (20 K min^{-1}, nitrogen atmosphere).

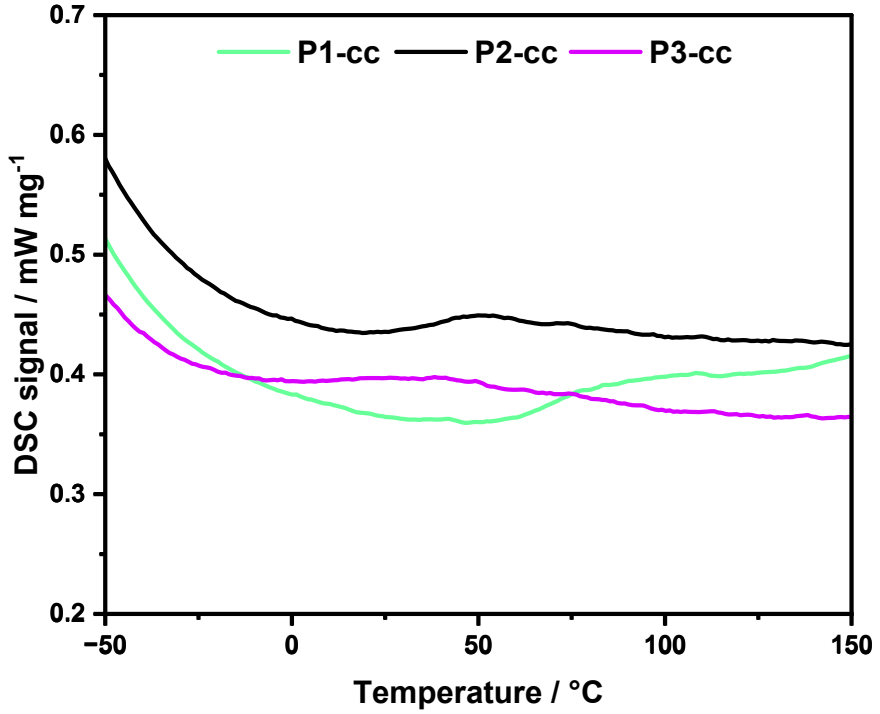

Figure S14. DSC-curves of the polymers **P1-cc** to **P3-cc** (10 K min^{-1}, nitrogen atmosphere).

6 Dynamic mechanical thermal analysis (DMTA)

For the dynamic mechanical thermal analysis (DMTA), the temperature was increased from 25 °C to 100, 110, 130 or 150 °C with a heating rate of 2 K min^{-1} at a constant oscillating shear strain of 0.05% and a constant frequency of 1 Hz. The results are shown in **Figure S15** to **S22**. Furthermore, the plots of the complex viscosity to determine T_v are shown in **Figure S23** to **S28**.

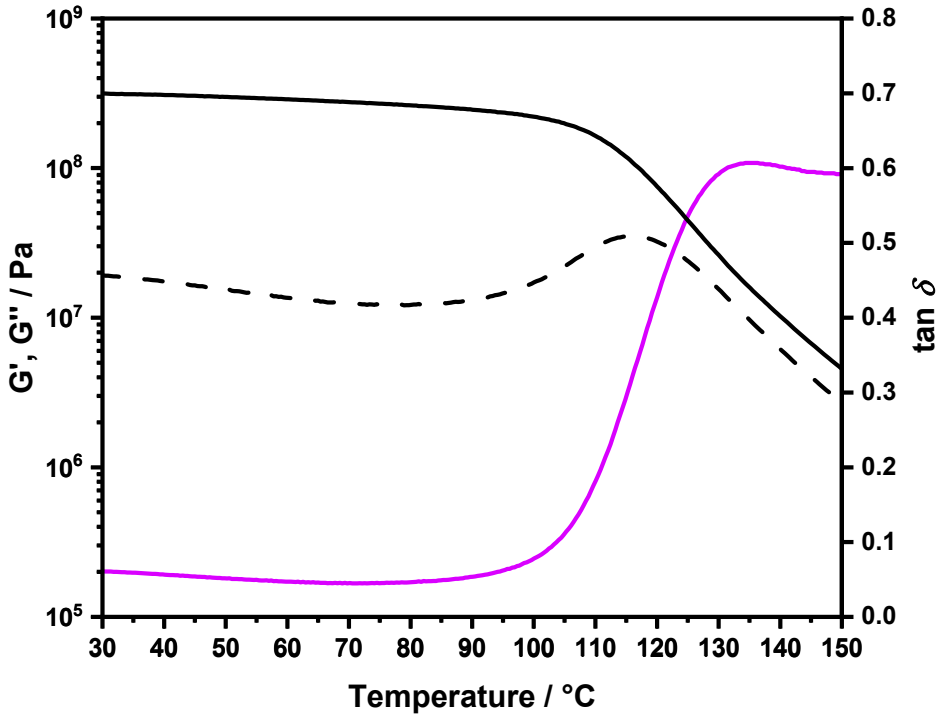

Figure S15. Results of the DMTA-measurement of **P1-Fe** with the storage modulus G' (black), the loss modulus G'' (black dotted) and the loss factor tan δ (violet).

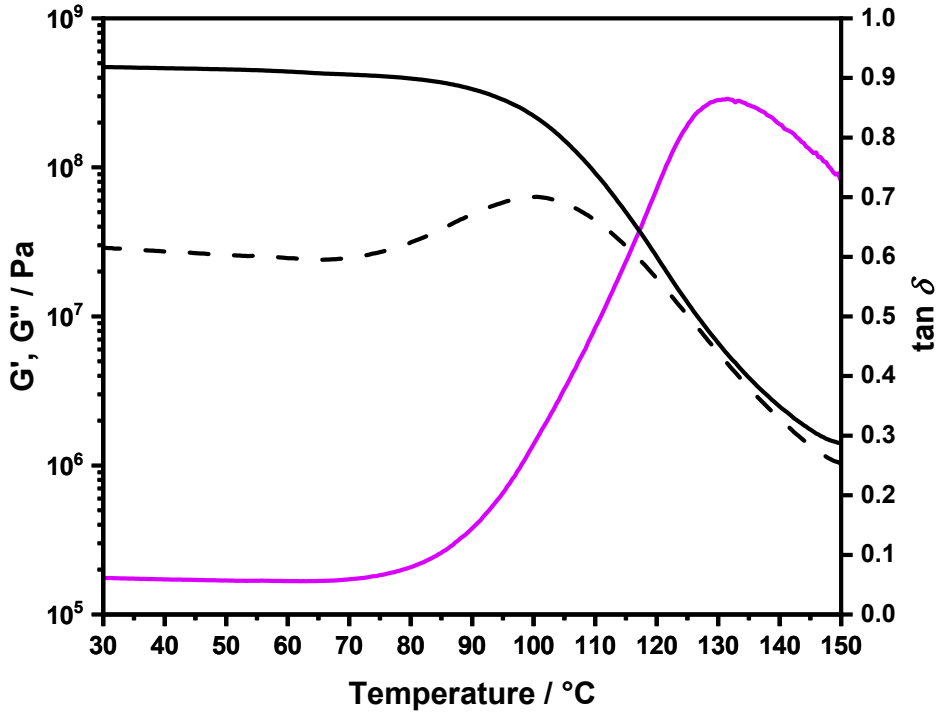

Figure S16. Results of the DMTA-measurement of **P1-Zn** with the storage modulus G' (black), the loss modulus G'' (black dotted) and the loss factor tan *δ* (violet).

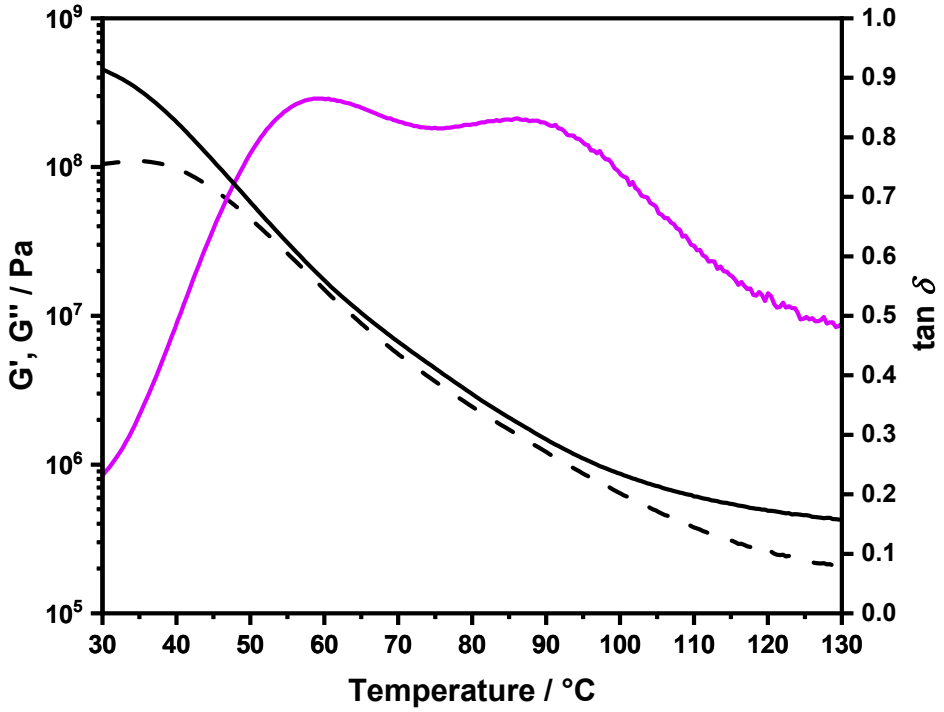

Figure S17. Results of the DMTA-measurement of **P2-Fe** with the storage modulus G**'** (black), the loss modulus G**''** (black dotted) and the loss factor tan *δ* (violet).

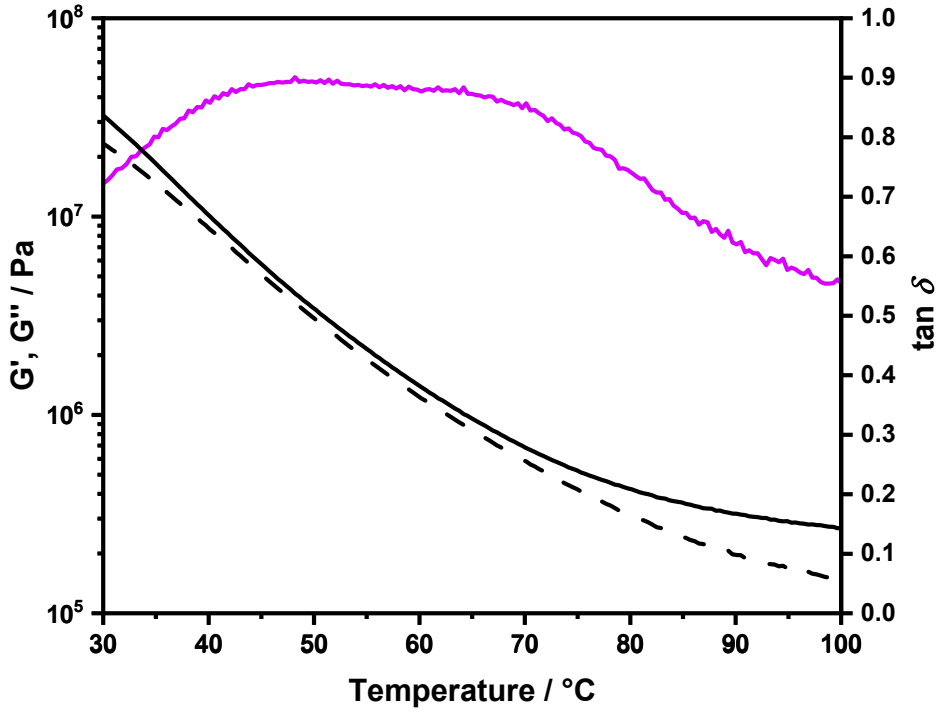

Figure S18. Results of the DMTA-measurement of **P3-Fe** with the storage modulus G' (black), the loss modulus G'' (black dotted) and the loss factor tan δ (violet).

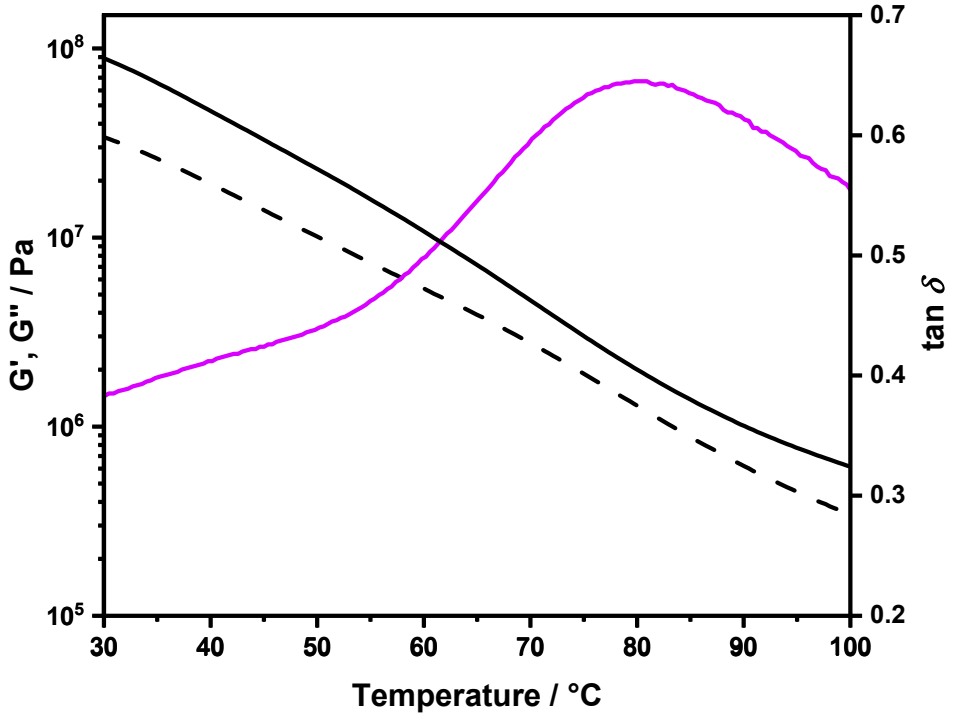

Figure S19. Results of the DMTA-measurement of **P3-Zn** with the storage modulus G' (black), the loss modulus G'' (black dotted) and the loss factor tan δ (violet).

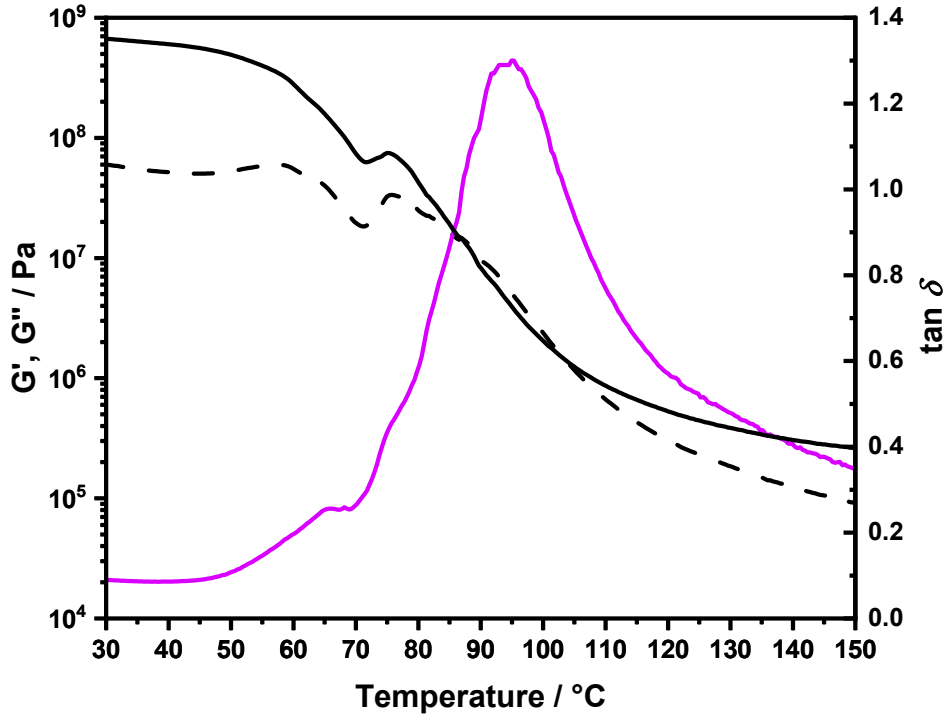

Figure S20. Results of the DMTA-measurement of **P1-cc** with the storage modulus G' (black), the loss modulus G'' (black dotted) and the loss factor tan *δ* (violet).

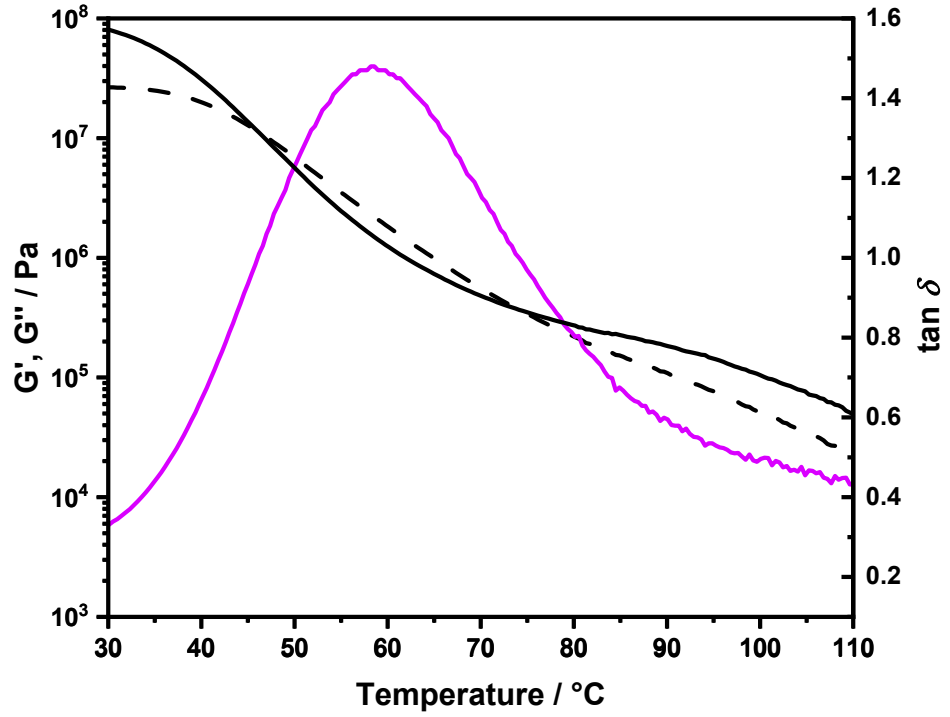

Figure S21. Results of the DMTA-measurement of **P2-cc** with the storage modulus G**'** (black), the loss modulus G**''** (black dotted) and the loss factor tan *δ* (violet).

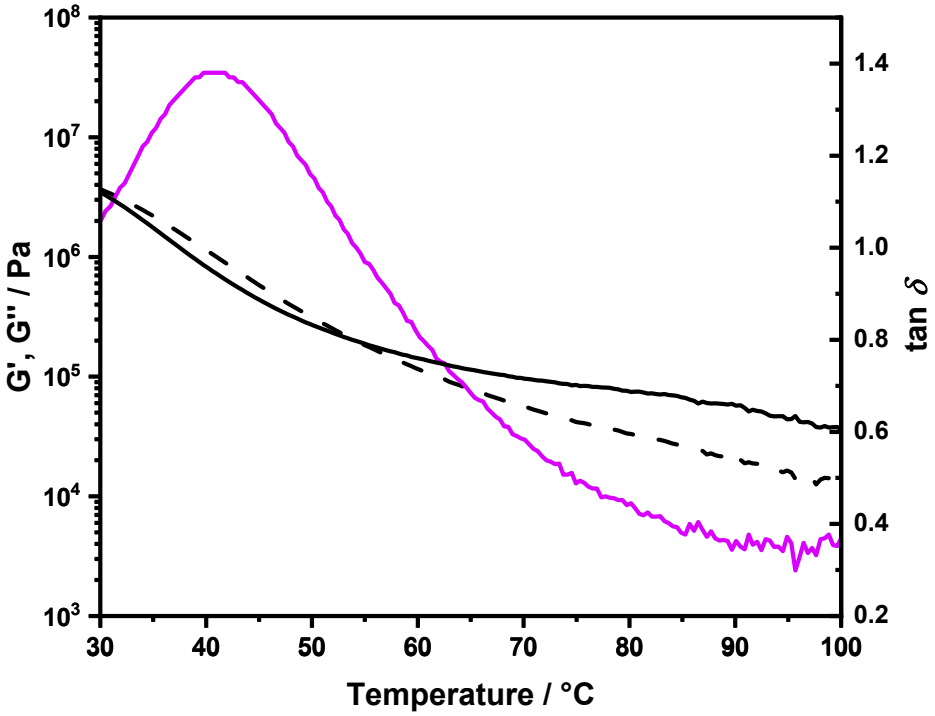

Figure S22. Results of the DMTA-measurement of **P3-cc** with the storage modulus G' (black), the loss modulus G'' (black dotted) and the loss factor tan *δ* (violet).

7 Frequency sweeps

For the frequency sweeps, the temperature was set to a specific value. After annealing the sample at this temperature for five minutes, a constant oscillating shear of 0.05% was applied. The shear strain and temperature were maintained constant afterwards, while the frequency was decreased in a logarithmic profile from 628 to 0.00628 rad s^{-1}. Subsequently, the next measurements were performed at different temperatures. It should be noted that the first measurement point at 628 rad s^{-1} may be affected by measurement inaccuracies leading to a noticeable kink in the plot. The results are shown in **Figure S22** to **S29**.

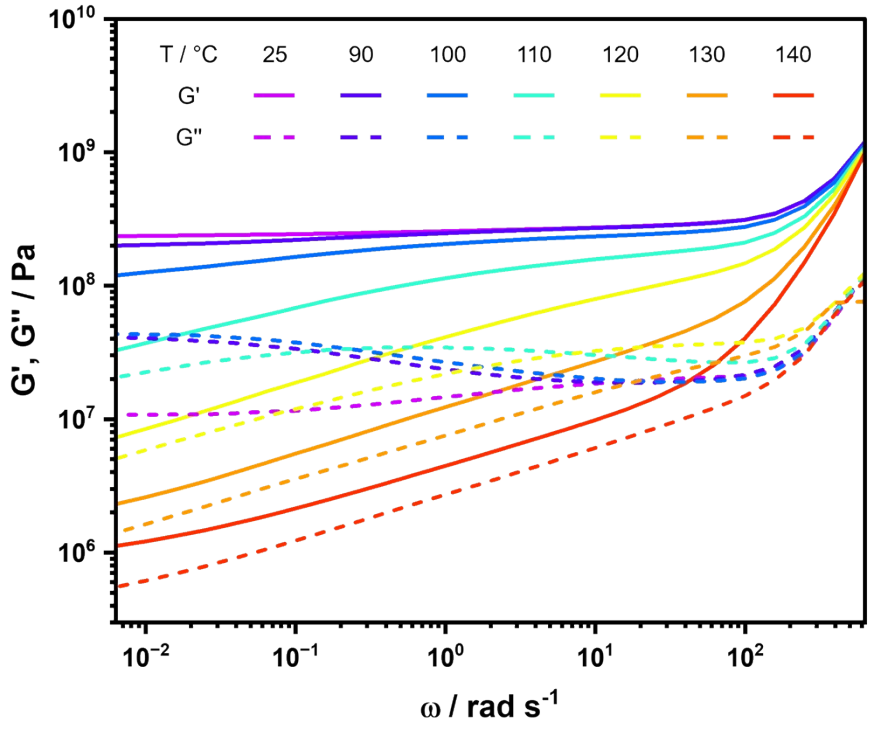

Figure S22. Results of the frequency sweeps of **P1-Fe** at different temperatures.

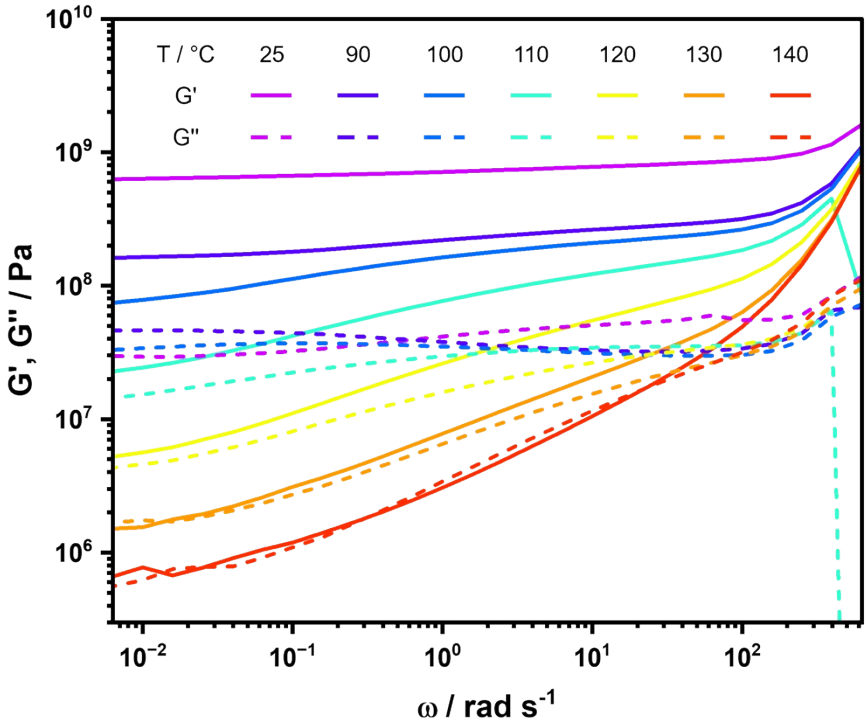

Figure S23. Results of the frequency sweeps of **P1-Zn** at different temperatures.

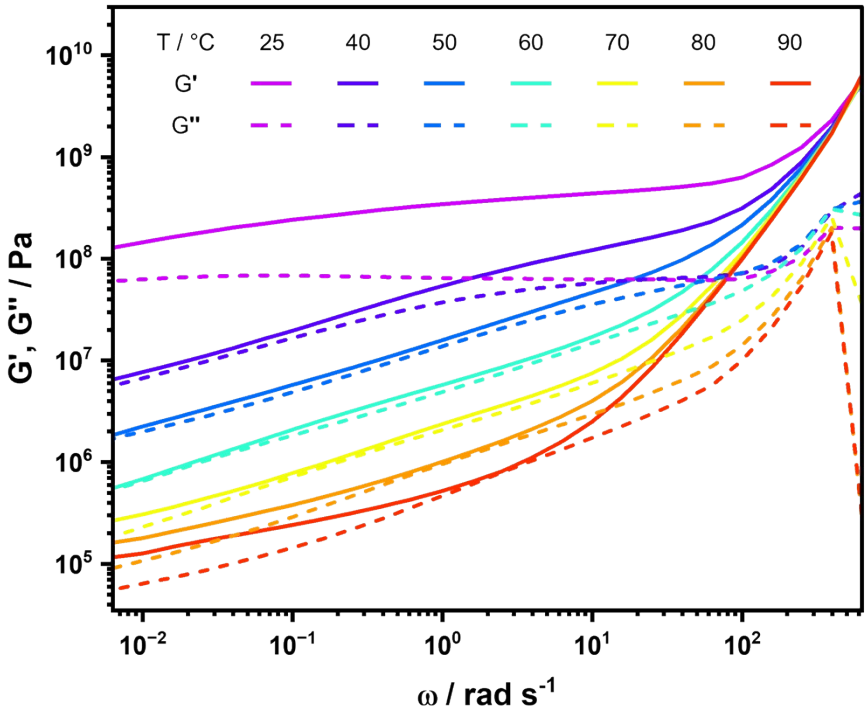

Figure S24. Results of the frequency sweeps of **P2-Fe** at different temperatures.

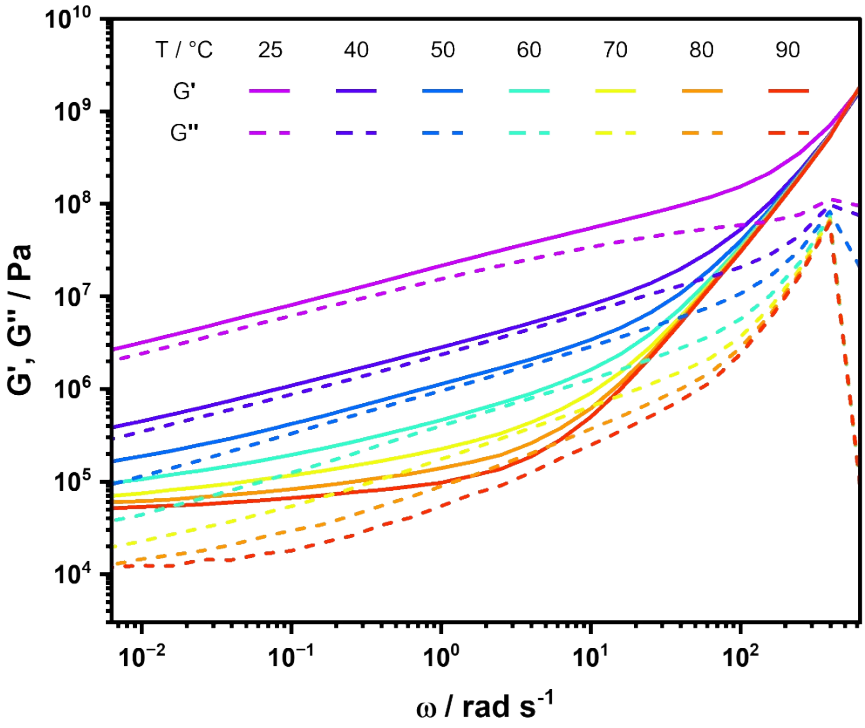

Figure S25. Results of the frequency sweeps of **P3-Fe** at different temperatures.

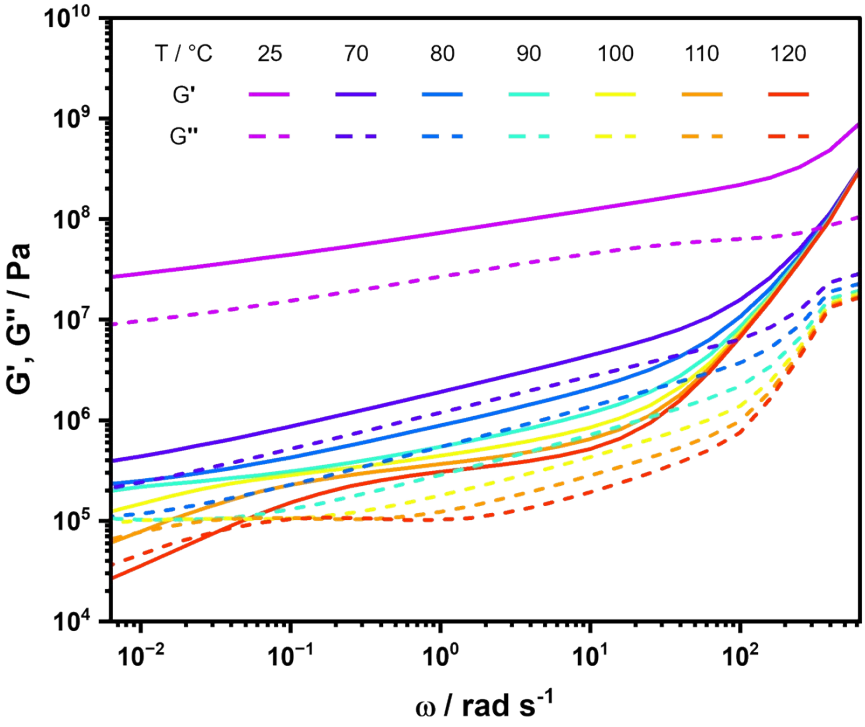

Figure S26. Results of the frequency sweeps of **P3-Zn** at different temperatures.

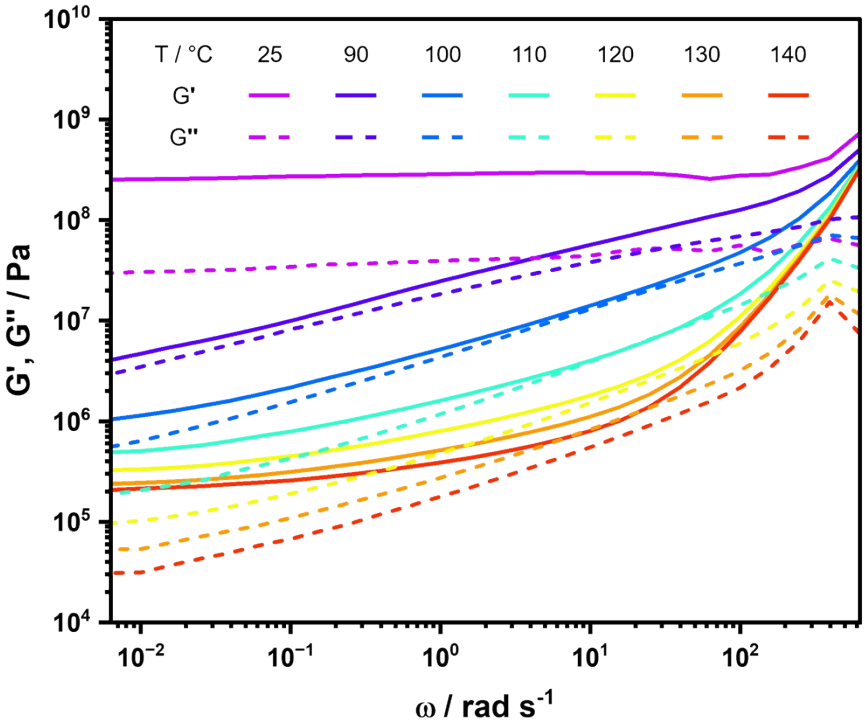

Figure S27. Results of the frequency sweeps of **P1-cc** at different temperatures.

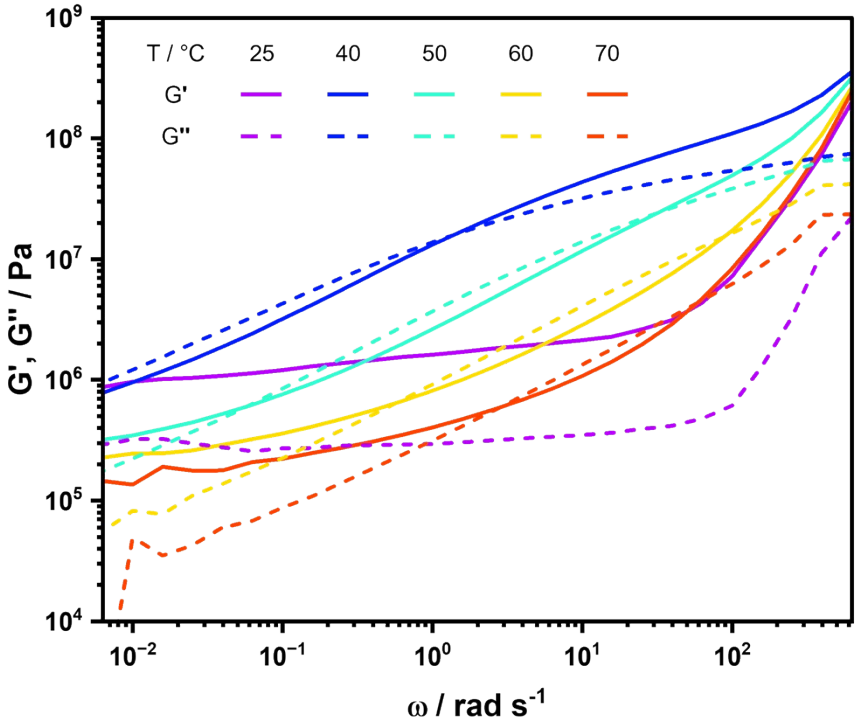

Figure S28. Results of the frequency sweeps of **P2-cc** at different temperatures.

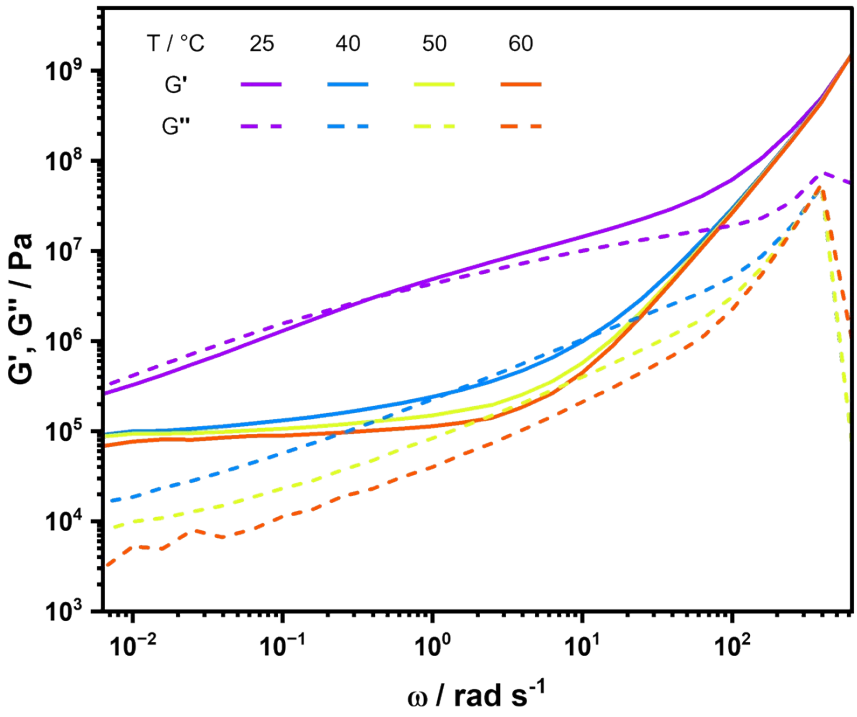

Figure S29. Results of the frequency sweeps of **P3-cc** at different temperatures.

8 Stress relaxation measurements

For the stress relaxation measurements, the temperature was set to a specific value. After annealing the sample at this temperature for 10 minutes, it was subjected to a linear ramp until a shear strain of 2% was achieved. The shear strain and temperature were then maintained constant for 900 seconds. Subsequently, measurements were conducted at other temperatures. The results of these measurements, the normalized plots and their fits using the Maxwell[8] and Kohlrausch-Williams-Watts (KWW)[9,10] models are shown in **Figure S30** to **S52**. Furthermore, the activation energies could be calculated using the Arrhenius equation and the values obtained from the Maxwell and KWW fits. The linear plots are depicted in **Figure S53** to **S58**. For **P3-Fe** and **P3-cc** the Maxwell and KWW models could not be applied, therefore no fits using these models and no Arrhenius fits are shown.

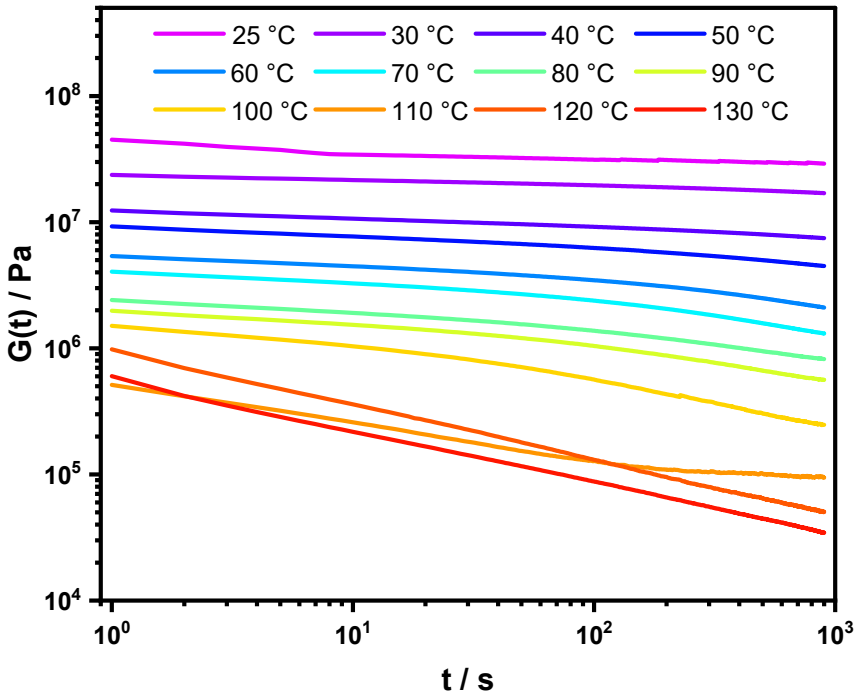

Figure S30. Results of the stress relaxation measurements of **P1-Fe** at different temperatures.

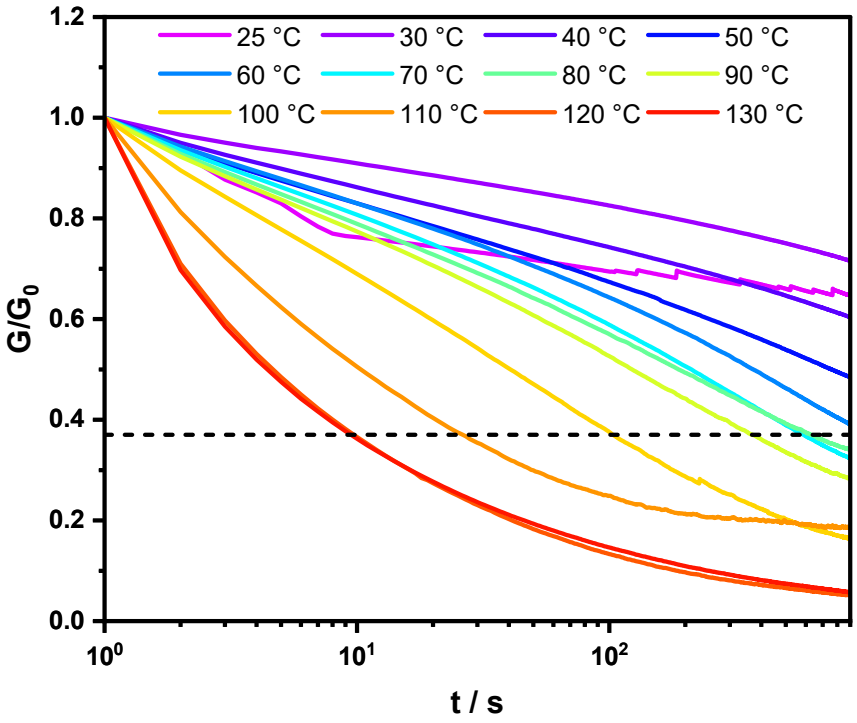

Figure S31. Normalized plot of the stress relaxation measurements of **P1-Fe**.

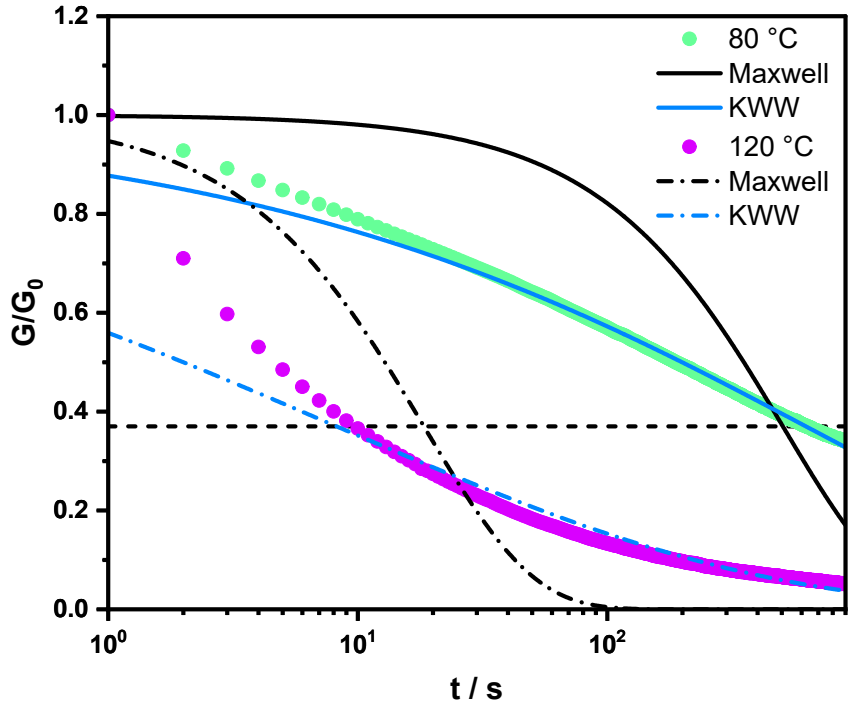

Figure S32. Normalized plot of the stress relaxation measurements of **P1-Fe** at 80 and 120 °C fitted using the Maxwell and KWW models.

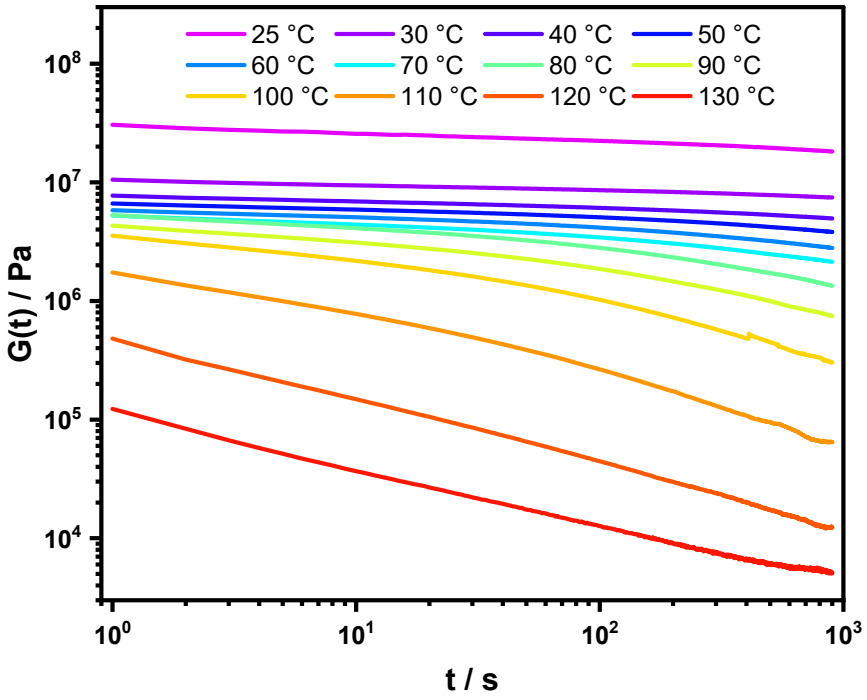

Figure S33. Results of the stress relaxation measurements of **P1-Zn** at different temperatures.

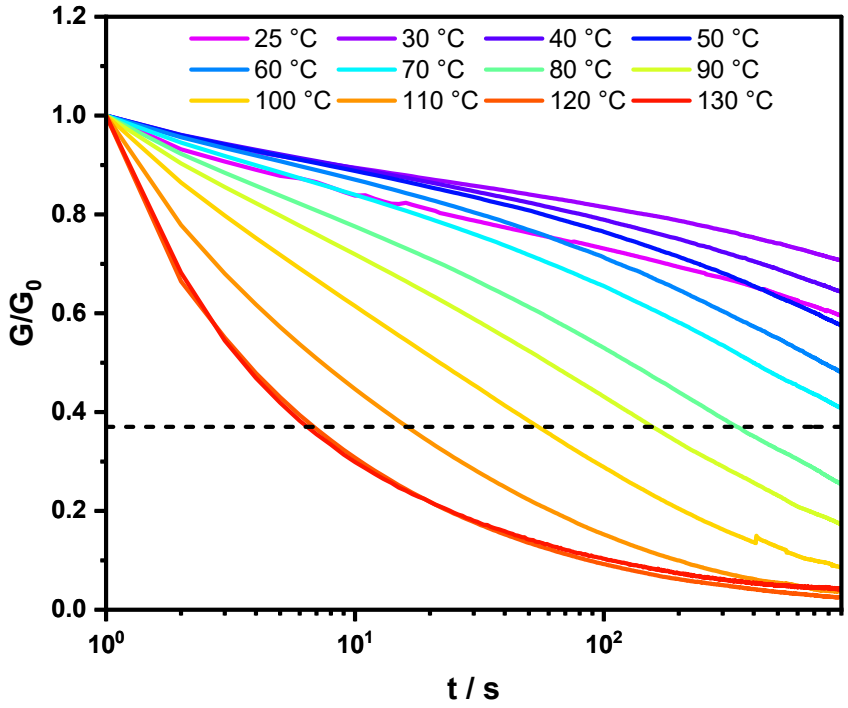

Figure S34. Normalized plot of the stress relaxation measurements of **P1-Zn**.

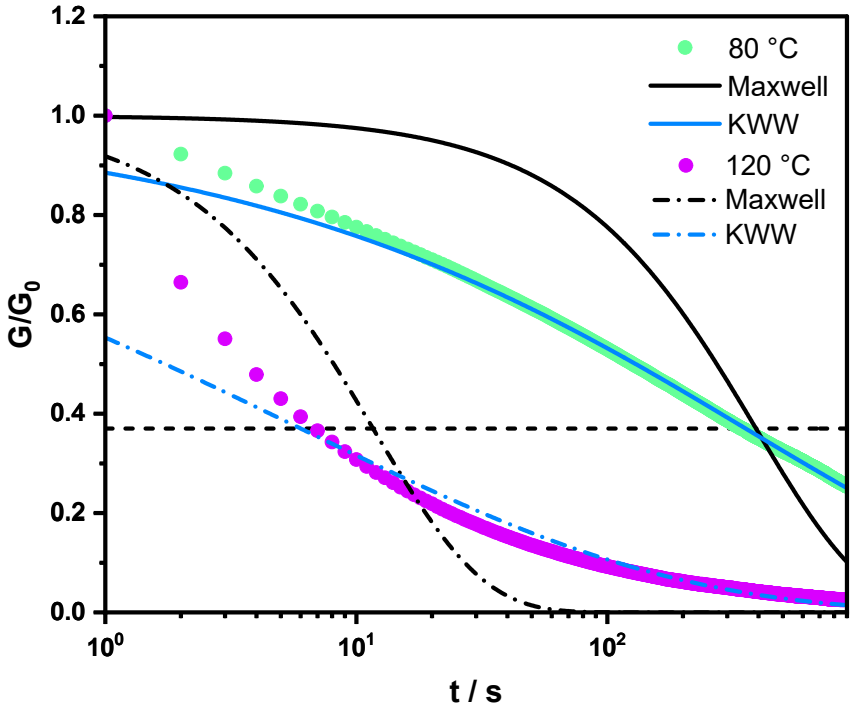

Figure S35. Normalized plot of the stress relaxation measurements of **P1-Zn** at 80 and 120 °C fitted using the Maxwell and KWW models.

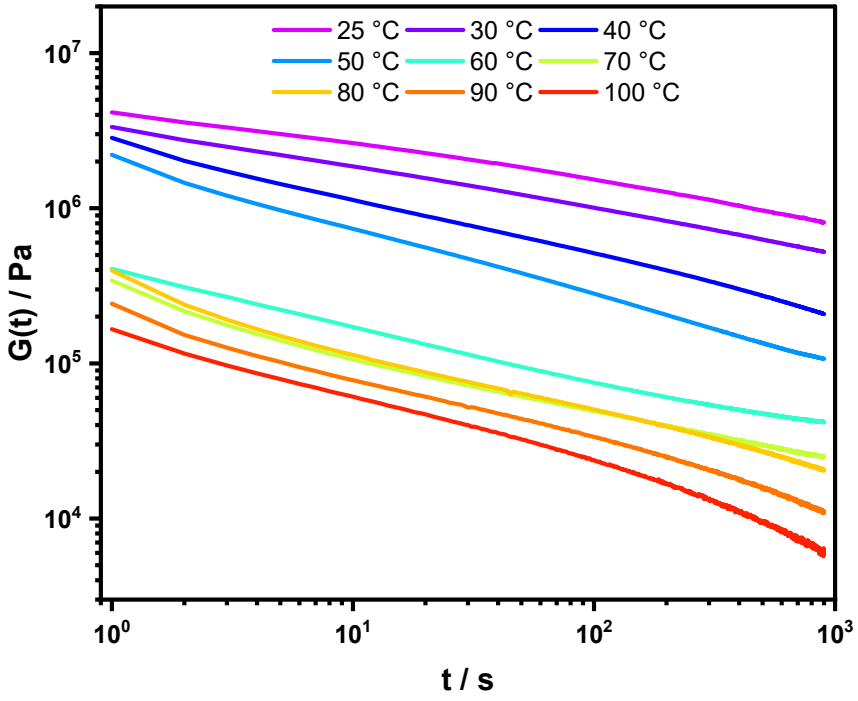

Figure S36. Results of the stress relaxation measurements of **P2-Fe** at different temperatures.

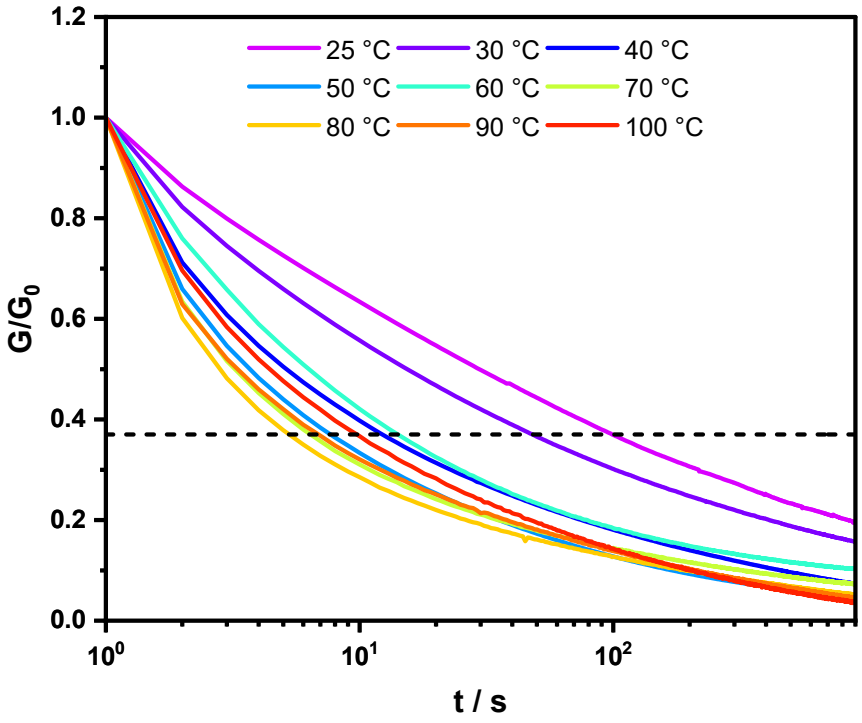

Figure S37. Normalized plot of the stress relaxation measurements of **P2-Fe**.

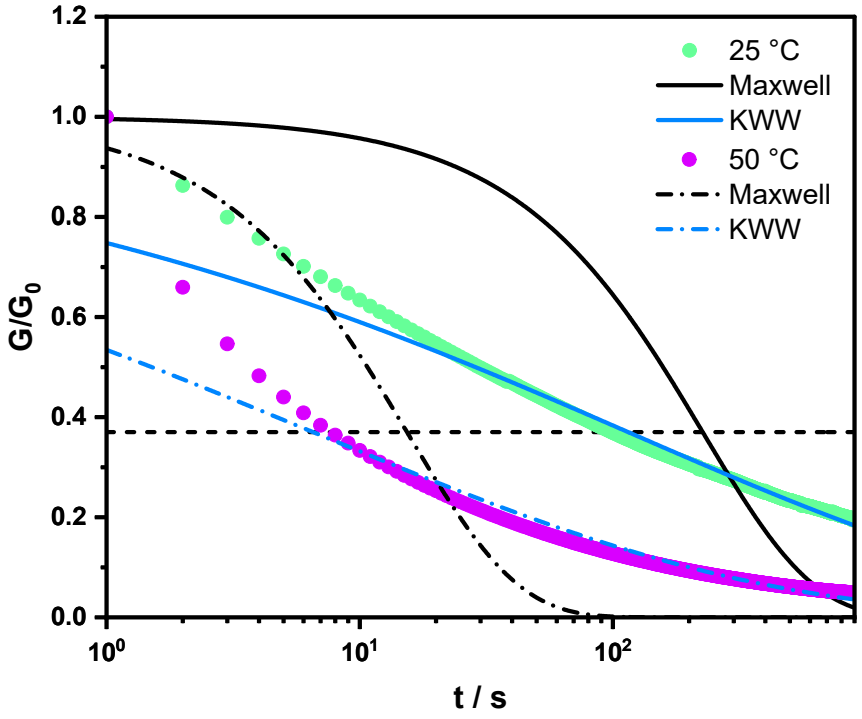

Figure S38. Normalized plot of the stress relaxation measurements of **P2-Fe** at 25 and 50 °C fitted using the Maxwell and KWW models.

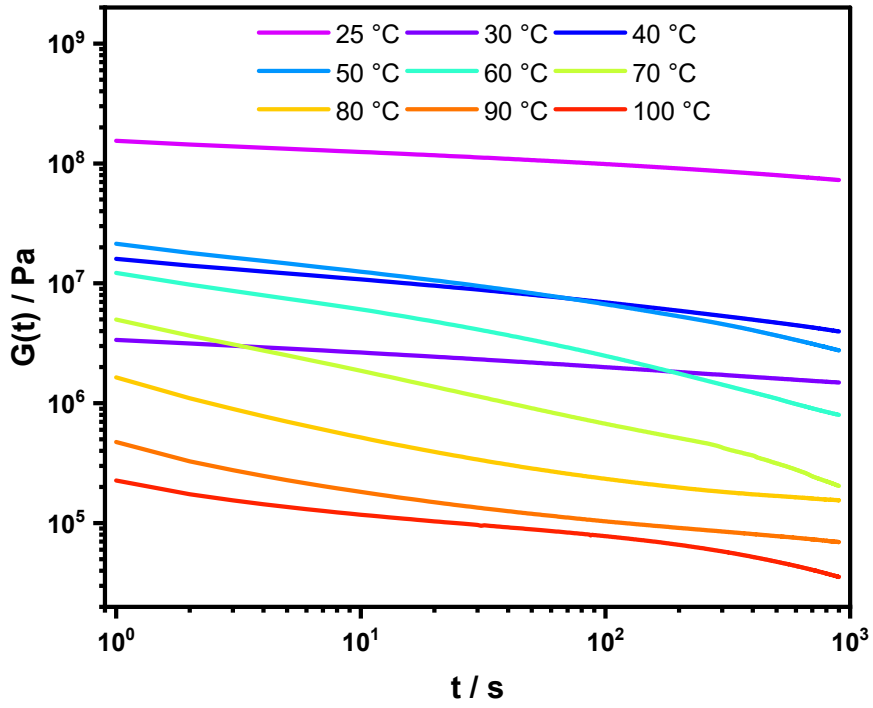

Figure S39. Results of the stress relaxation measurements of **P2-Zn** at different temperatures.

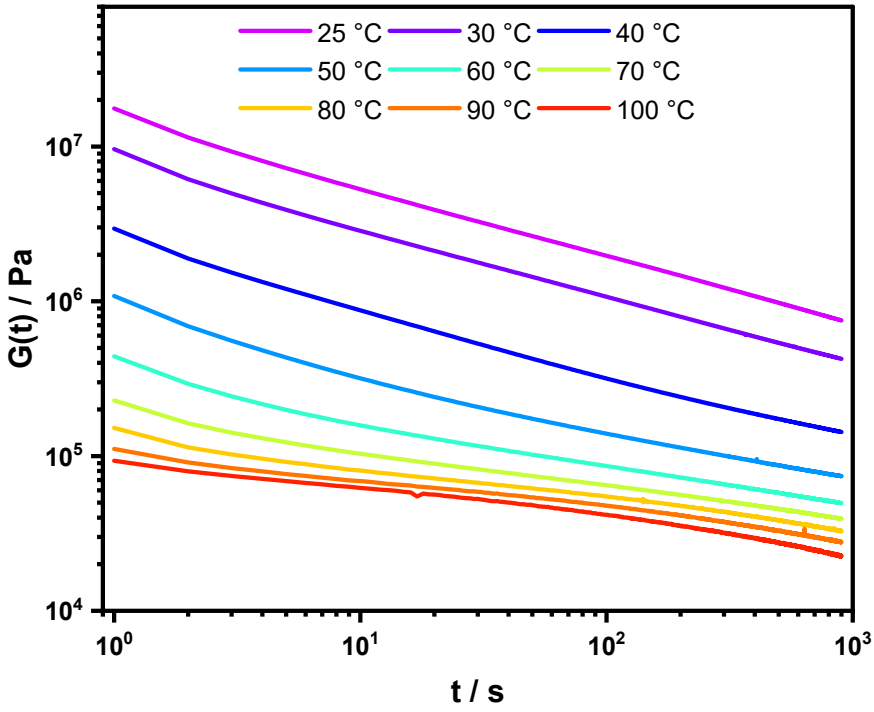

Figure S40. Results of the stress relaxation measurements of **P3-Fe** at different temperatures.

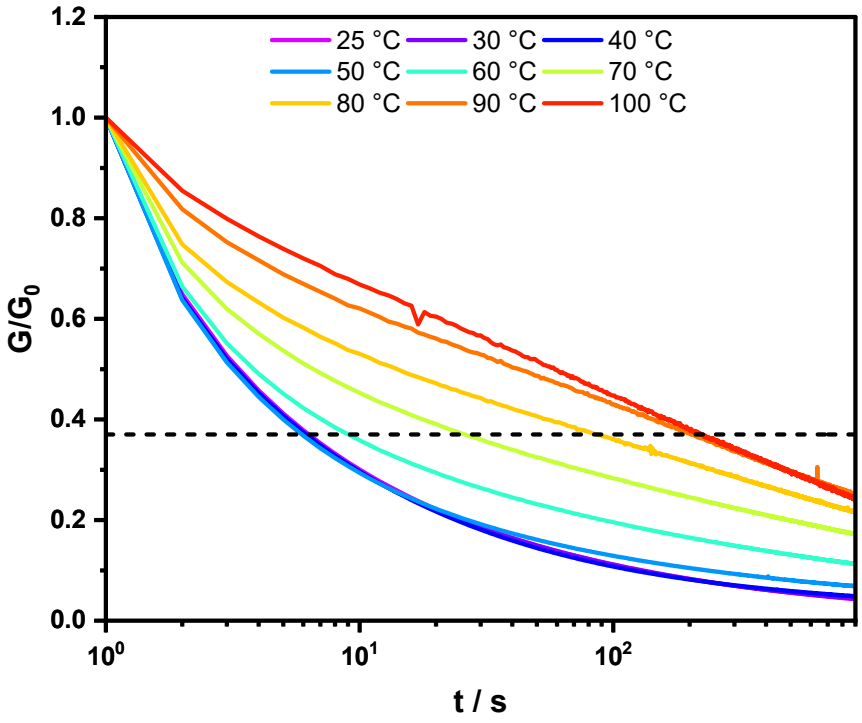

Figure S41. Normalized plot of the stress relaxation measurements of **P3-Fe**.

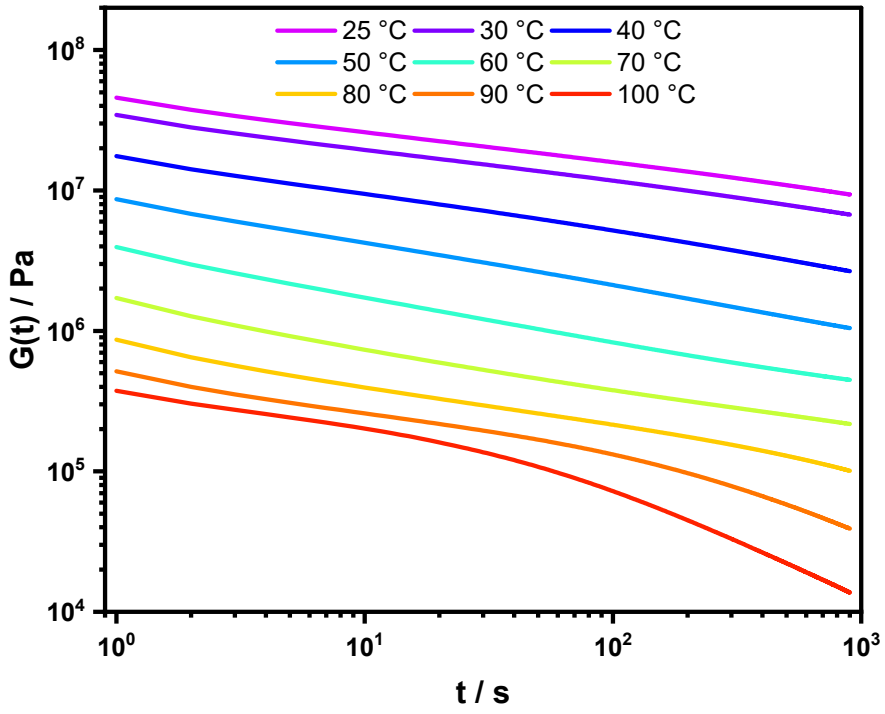

Figure S42. Results of the stress relaxation measurements of **P3-Zn** at different temperatures.

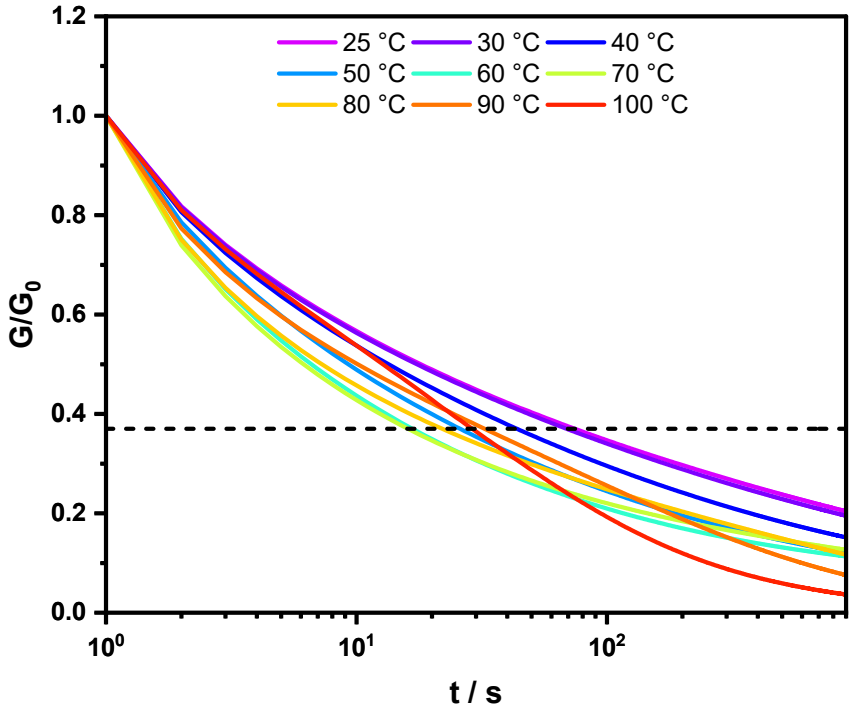

Figure S43. Normalized plot of the stress relaxation measurements of **P3-Zn**.

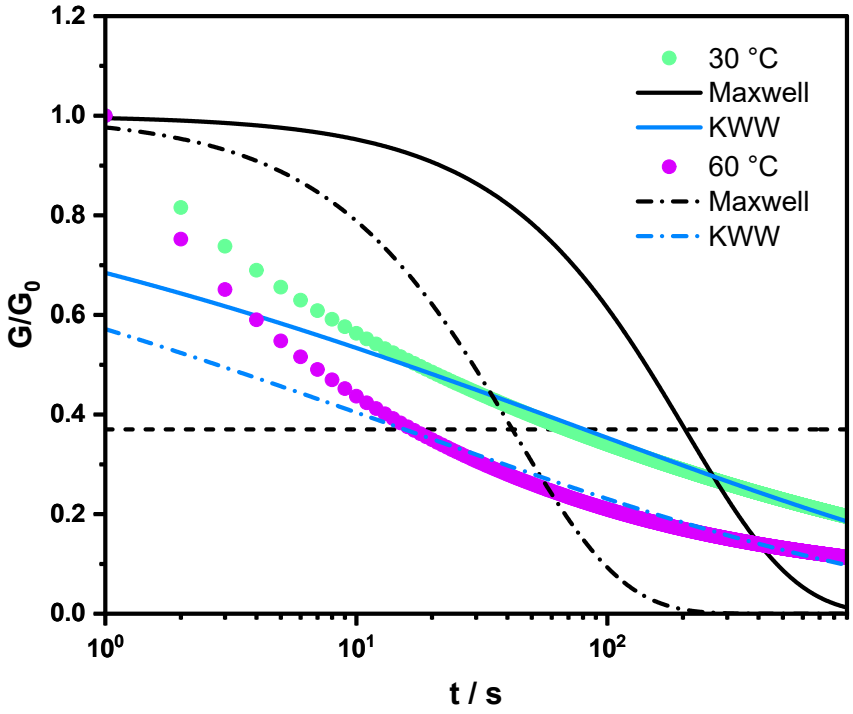

Figure S44. Normalized plot of the stress relaxation measurements of **P3-Zn** at 30 and 60 °C fitted using the Maxwell and KWW models.

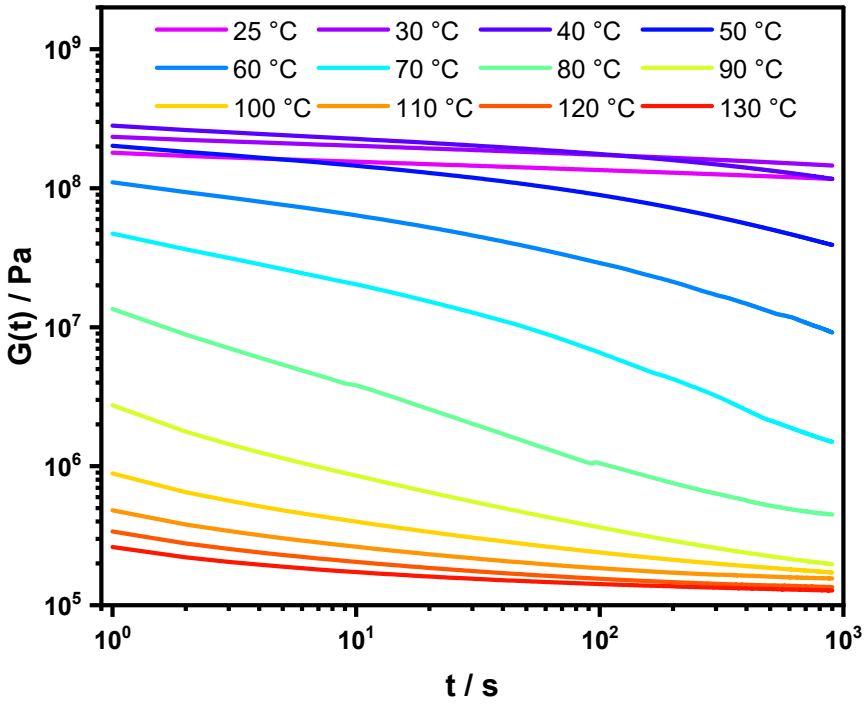

Figure S45. Results of the stress relaxation measurements of **P1-cc** at different temperatures.

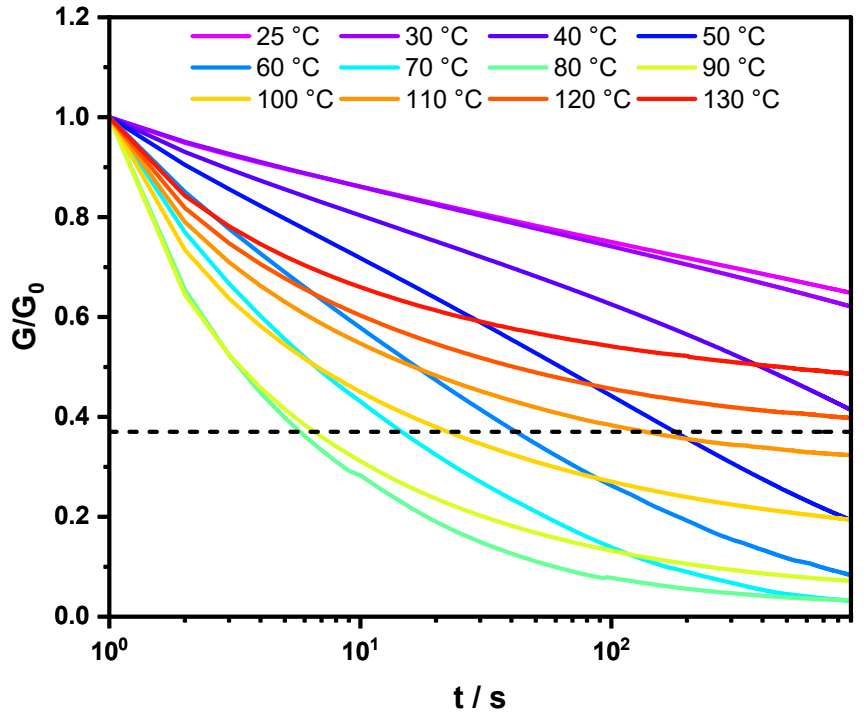

Figure S46. Normalized plot of the stress relaxation measurements of **P1-cc**.

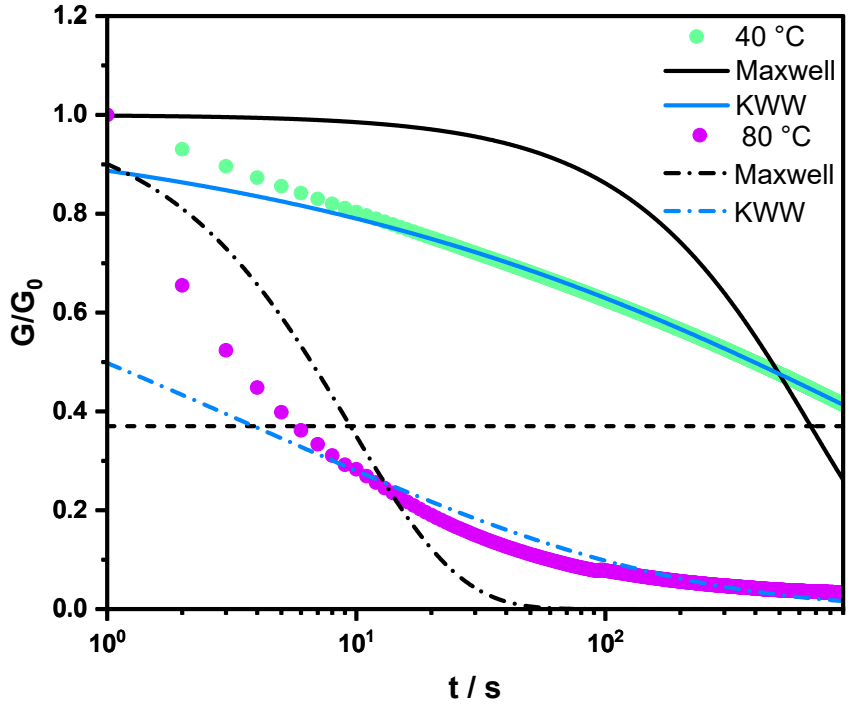

Figure S47. Normalized plot of the stress relaxation measurements of **P1-cc** at 40 and 80 °C fitted using the Maxwell and KWW models.

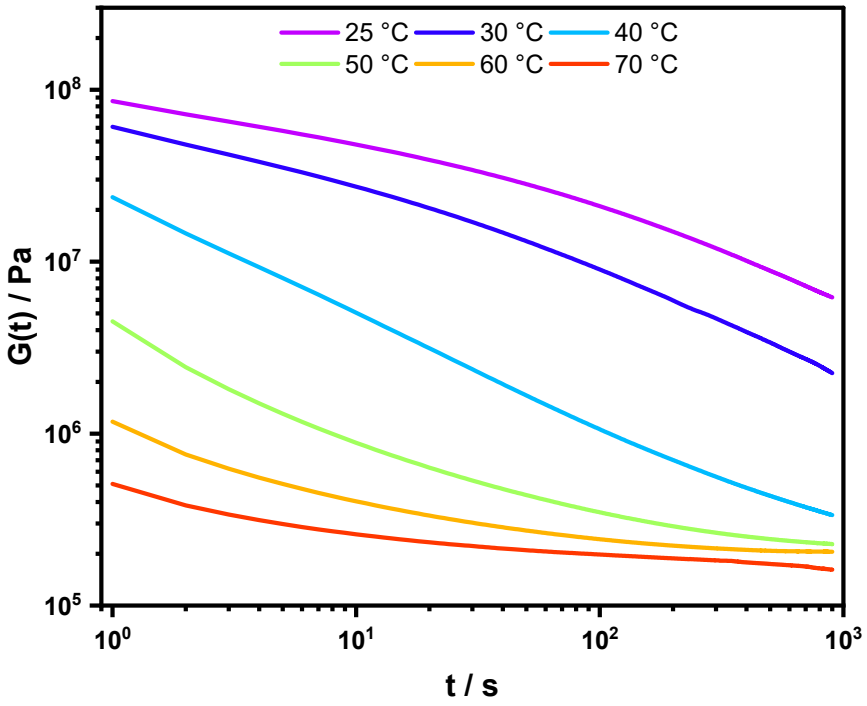

Figure S48. Results of the stress relaxation measurements of **P2-cc** at different temperatures.

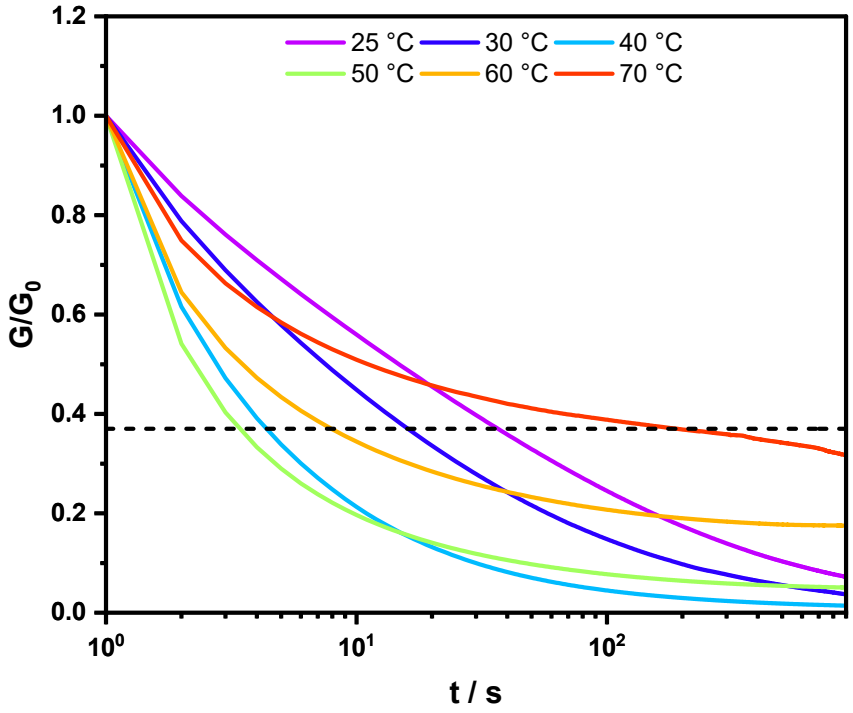

Figure S49. Normalized plot of the stress relaxation measurements of **P2-cc**.

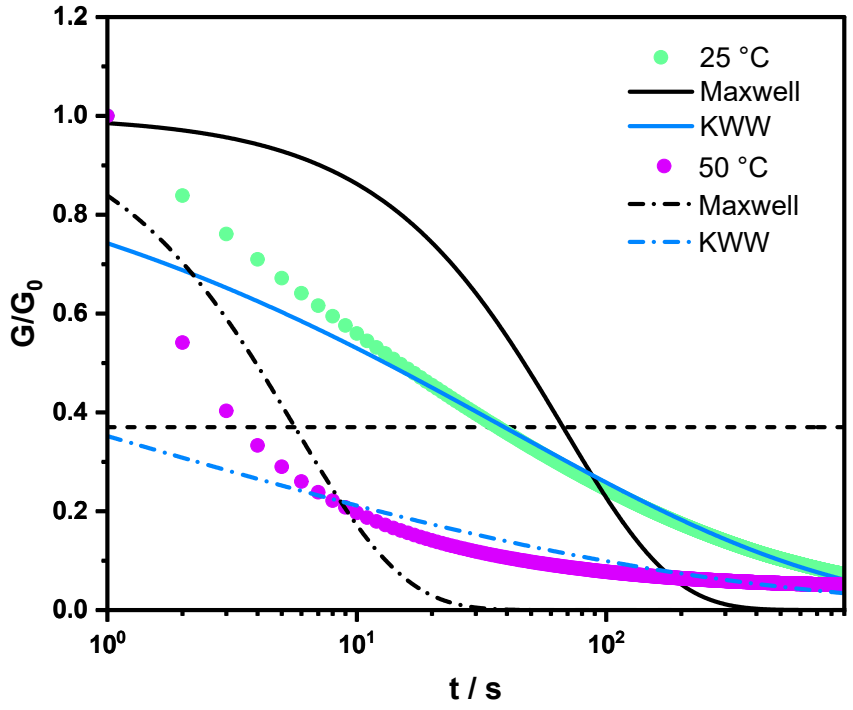

Figure S50. Normalized plot of the stress relaxation measurements of **P2-cc** at 25 and 50 °C fitted using the Maxwell and KWW models.

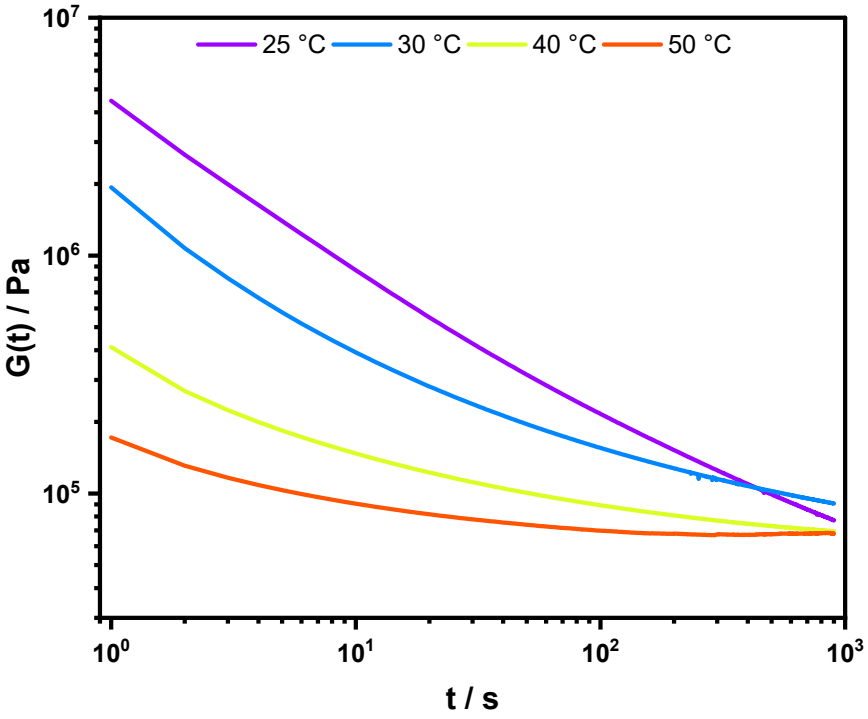

Figure S51. Results of the stress relaxation measurements of **P3-cc** at different temperatures.

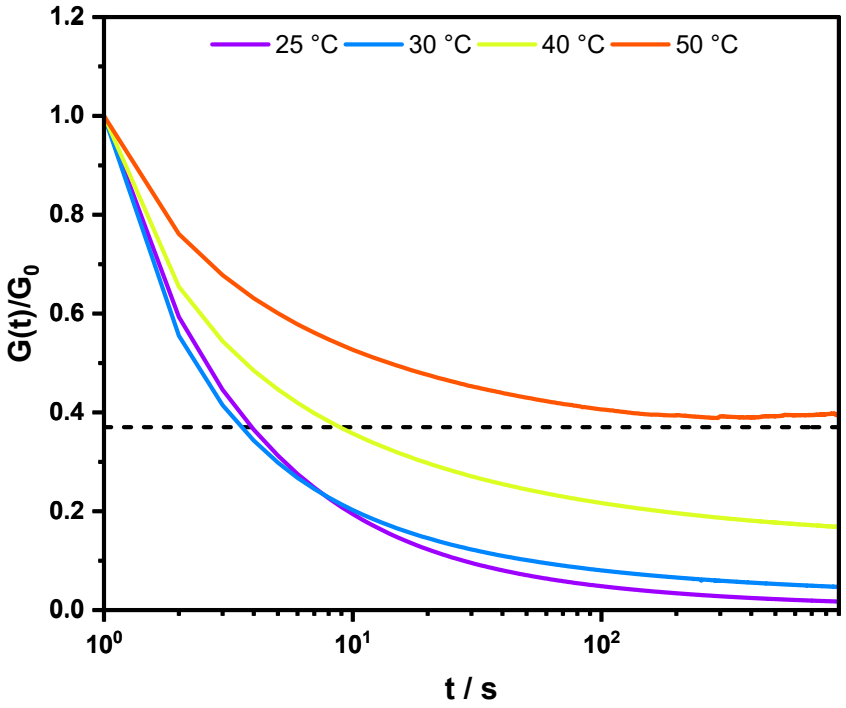

Figure S52. Normalized plot of the stress relaxation measurements of **P3-cc**.

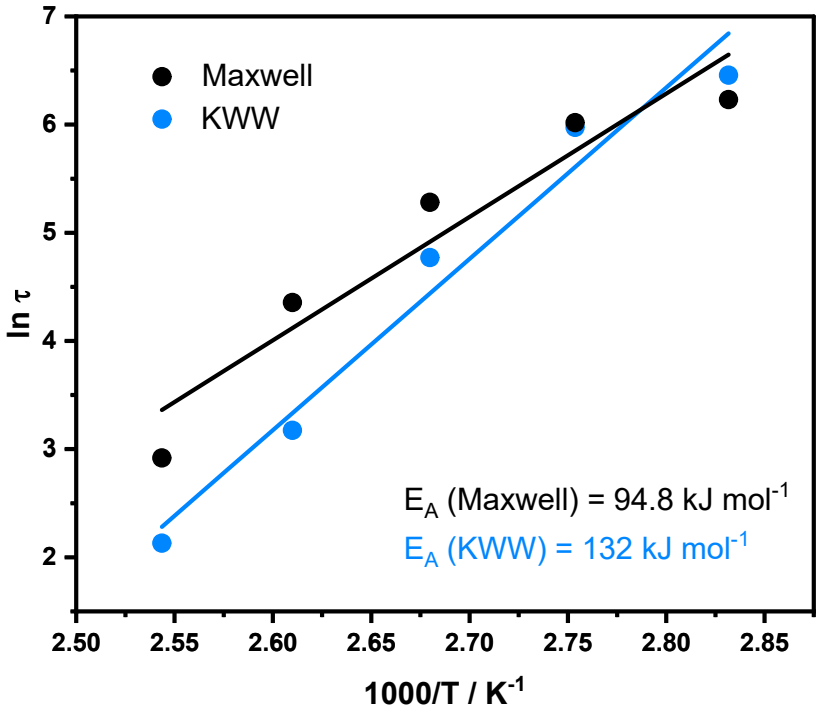

Figure S53. Arrhenius plot of the stress relaxation measurements of **P1-Fe**.

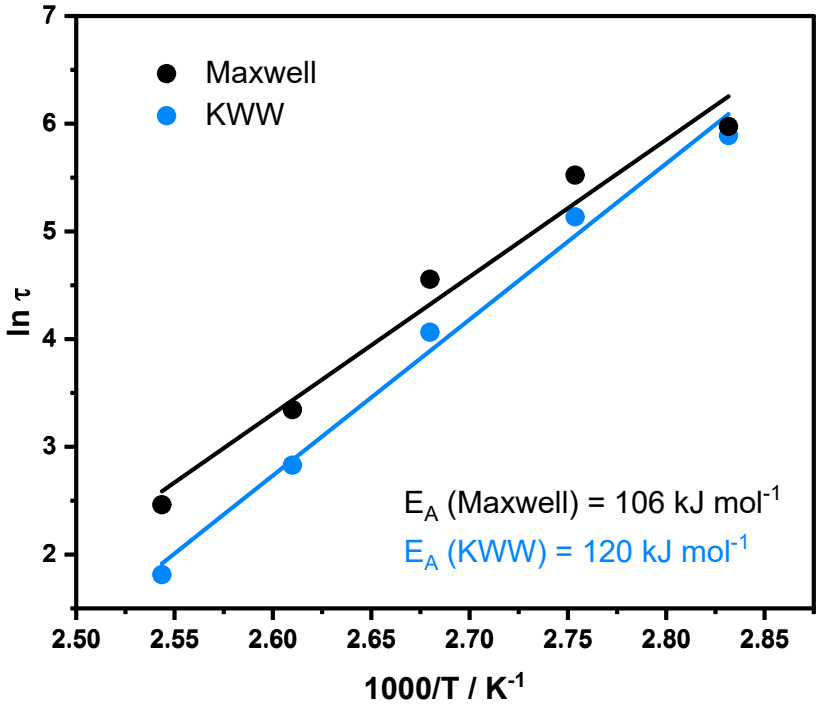

Figure S54. Arrhenius plot of the stress relaxation measurements of **P1-Zn**.

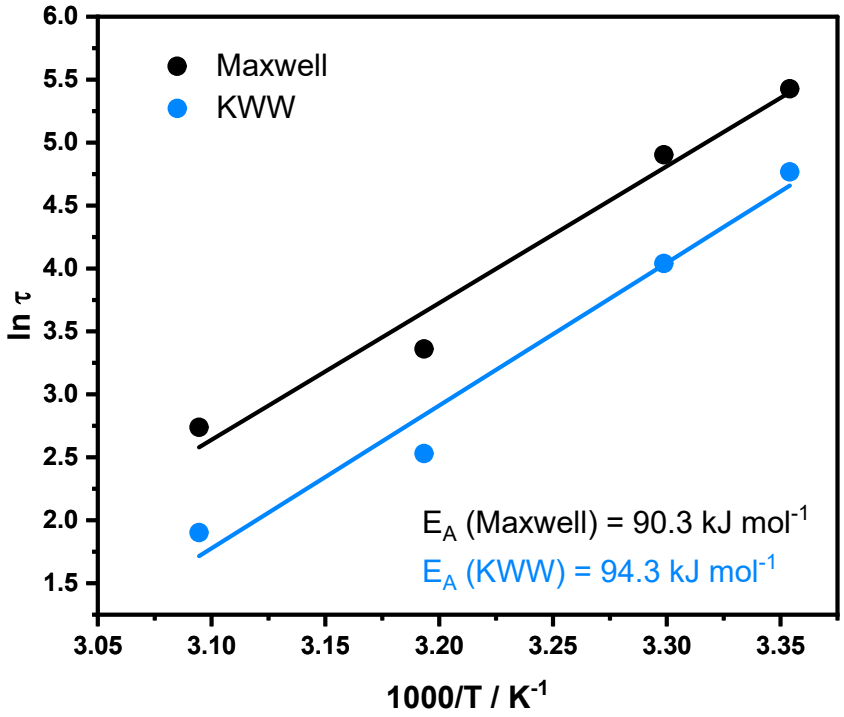

Figure S55. Arrhenius plot of the stress relaxation measurements of **P2-Fe**.

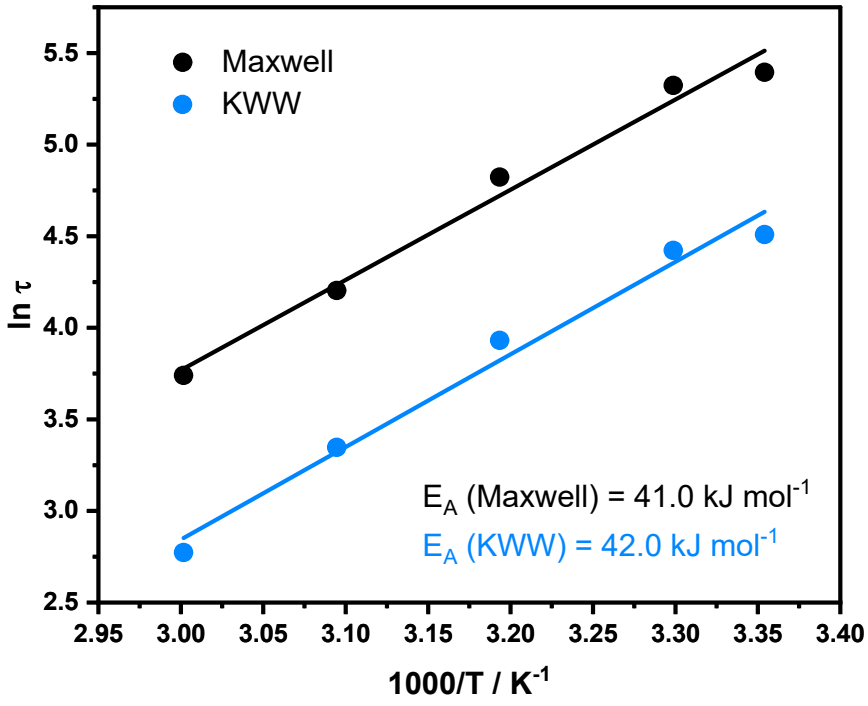

Figure S56. Arrhenius plot of the stress relaxation measurements of **P3-Zn**.

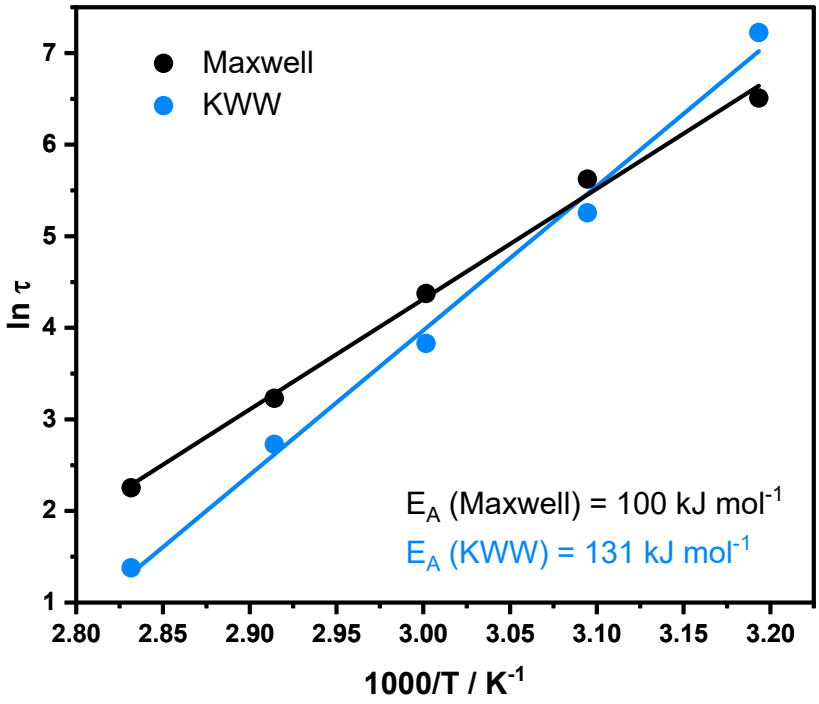

Figure S57. Arrhenius plot of the stress relaxation measurements of **P1-cc**.

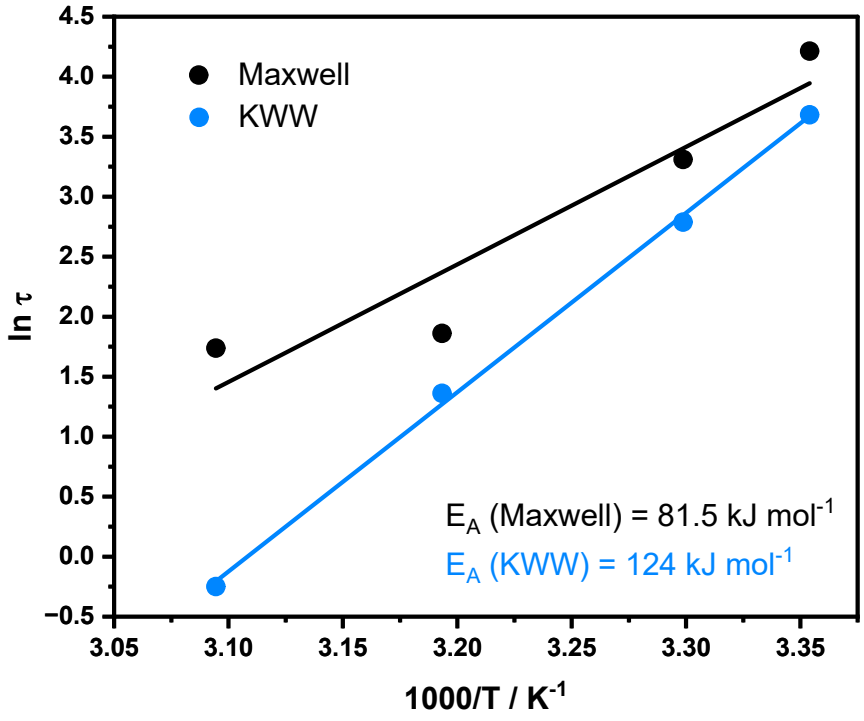

Figure S58. Arrhenius plot of the stress relaxation measurements of **P2-cc**.

Another method to analyze the stress relaxation data is the construction of master curves using the time-temperature superposition principle and applying the KWW model to fit the resulting curves. The resulting plots of the metallopolymers are presented in **Figure S59** to **S64**. Furthermore, the activation energies could be calculated using the Arrhenius equation and the values obtained from the KWW fit. The linear plots are depicted in **Figure S65** to **S69**. For **P3-Fe** the KWW model could not be applied, therefore, no Arrhenius fit is shown. The resulting activation energies are summarized in **Table S9**.

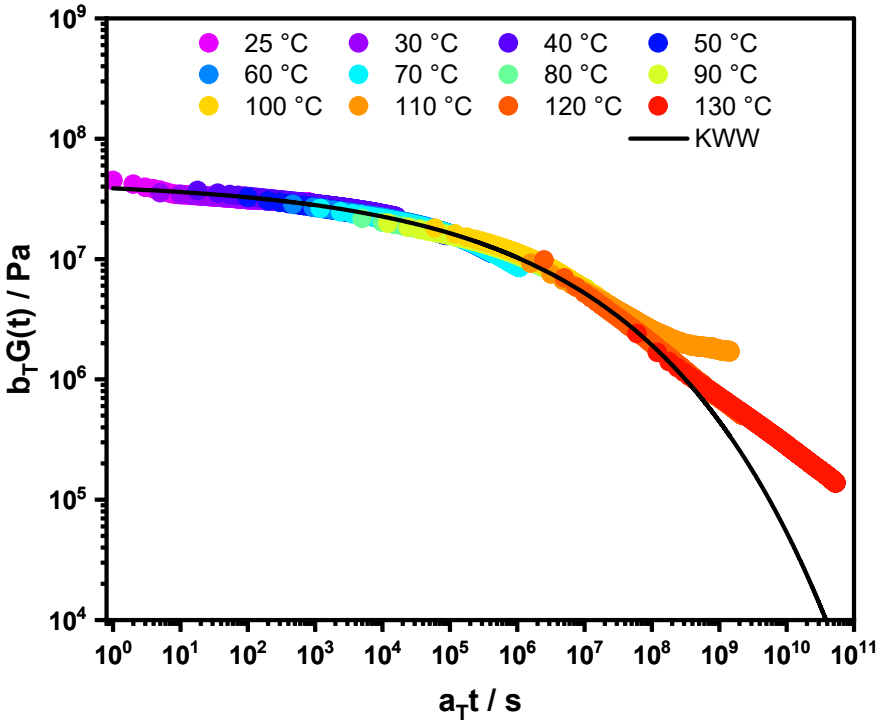

Figure S59. Master curve of **P1-Fe** at T_{ref} = 25 °C.

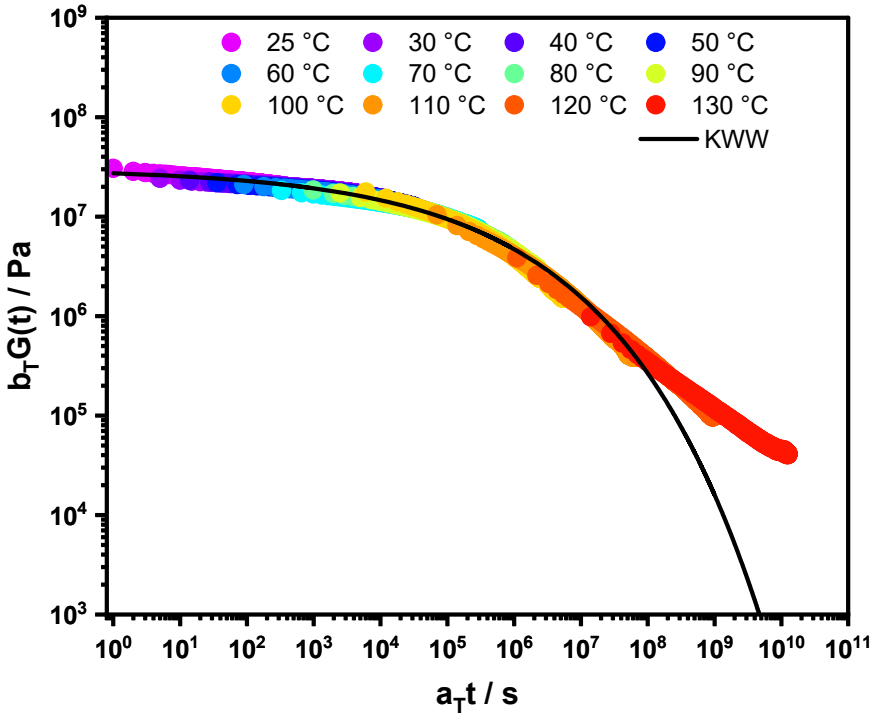

Figure S60. Master curve of **P1-Zn** at T_{ref} = 25 °C.

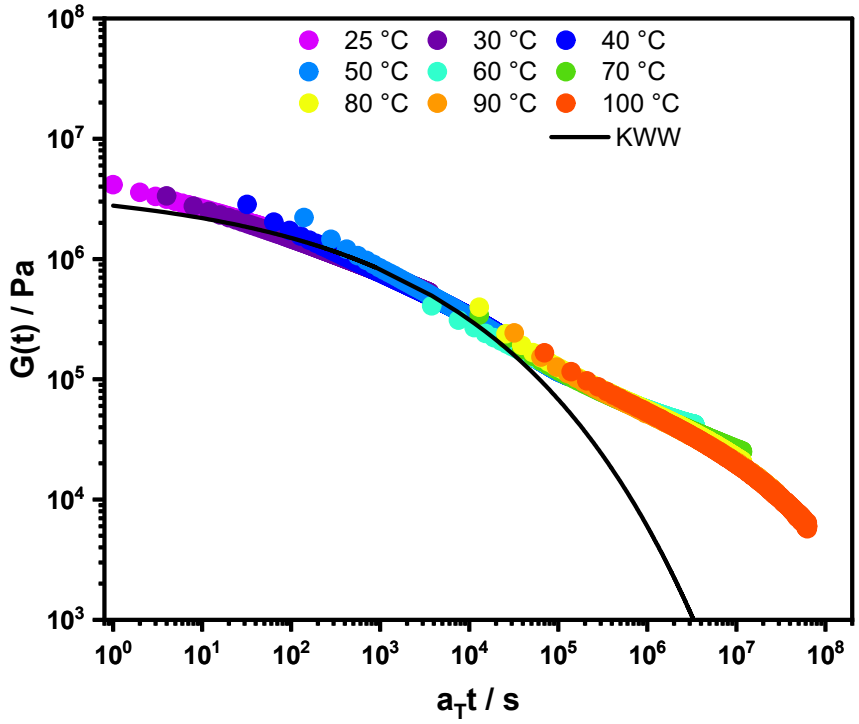

Figure S61. Master curve of **P2-Fe** at T_{ref} = 25 °C.

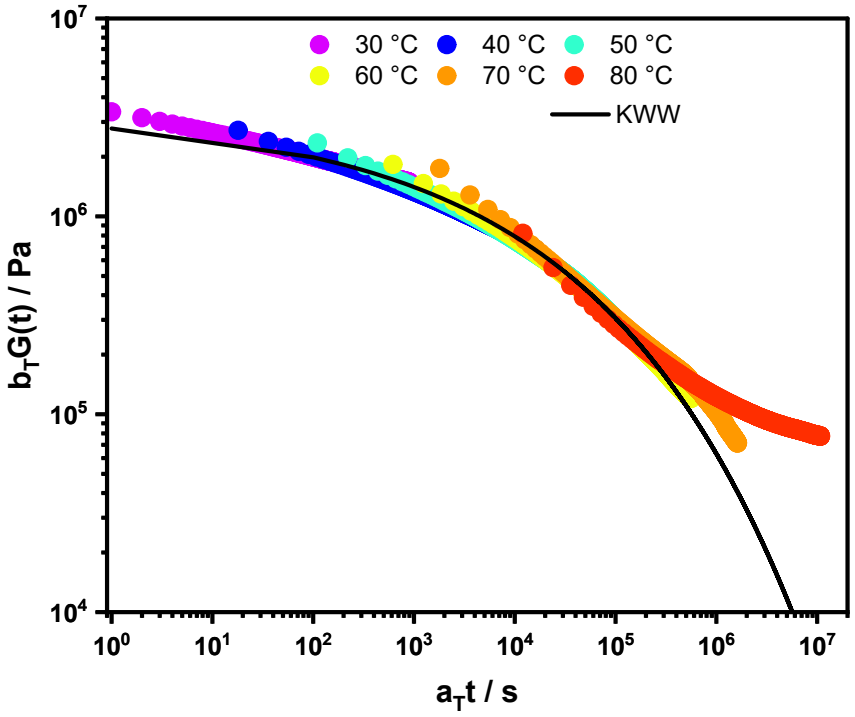

Figure S62. Master curve of **P2-Zn** at T_{ref} = 30 °C.

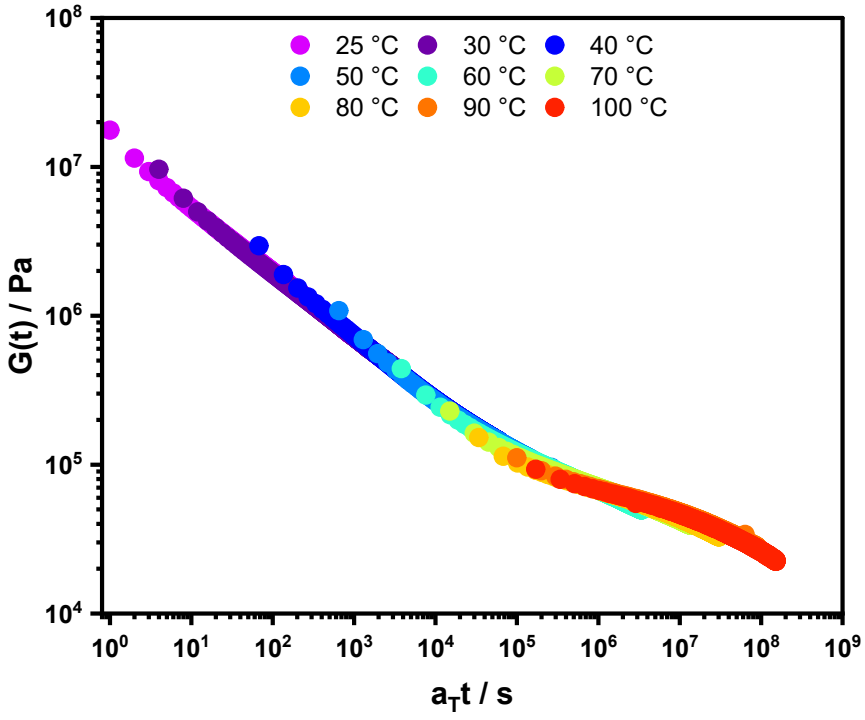

Figure S63. Master curve of **P3-Fe** at T_{ref} = 25 °C.

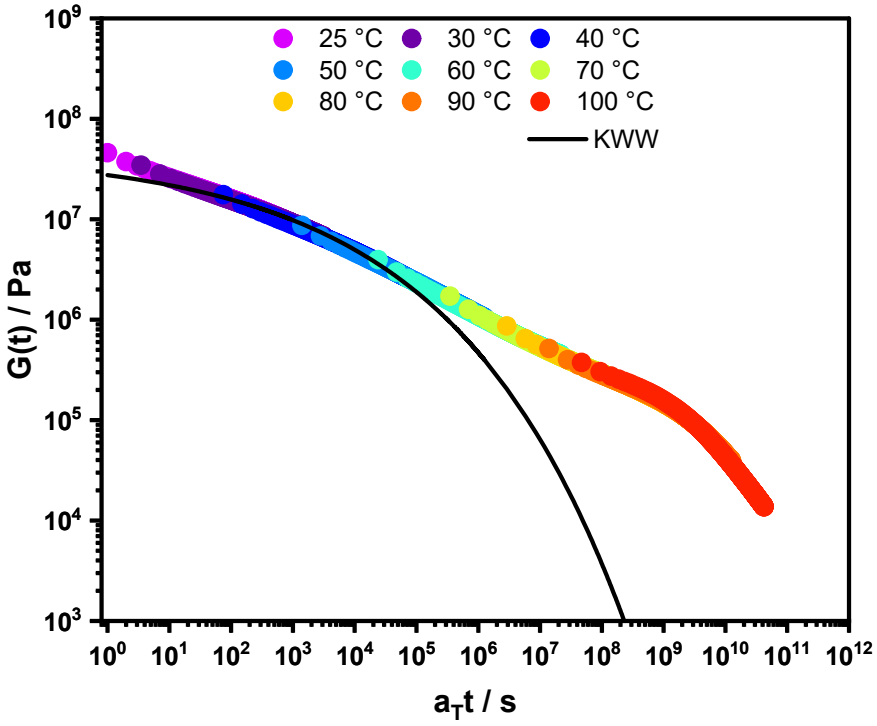

Figure S64. Master curve of **P3-Zn** at T_{ref} = 25 °C.

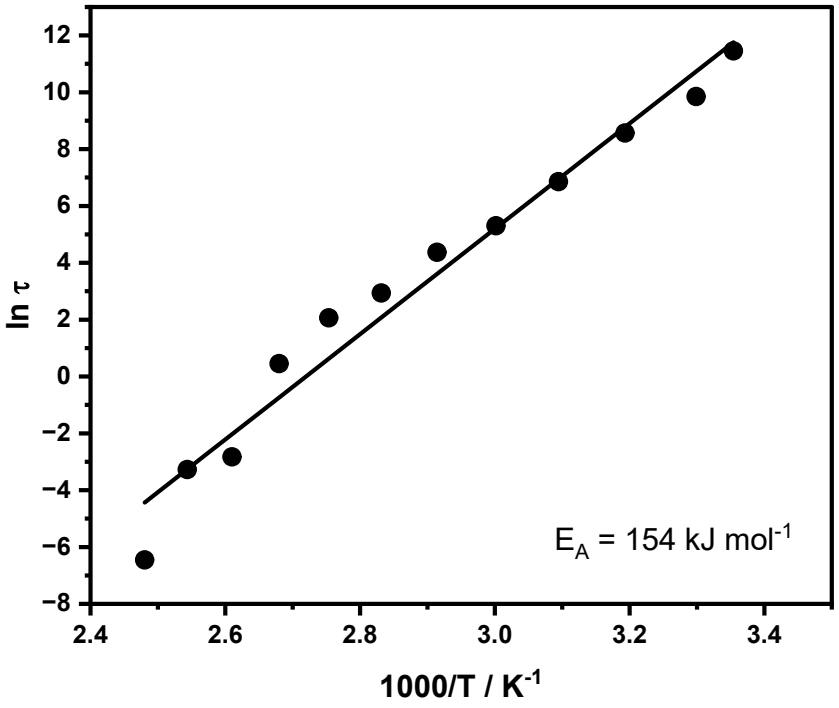

Figure S65. Arrhenius plot of the stress relaxation measurements of **P1-Fe**.

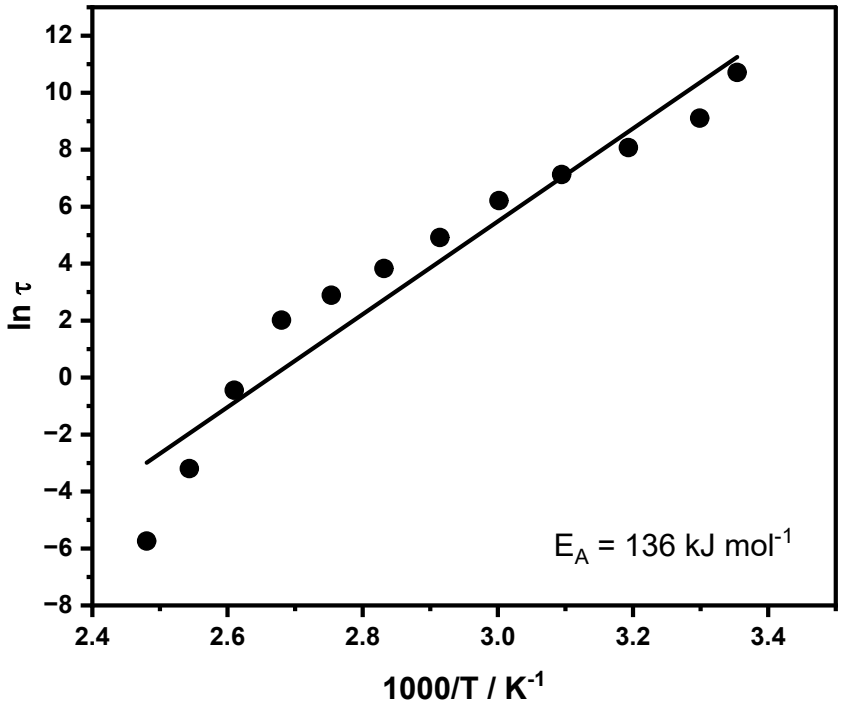

Figure S66. Arrhenius plot of the stress relaxation measurements of **P1-Zn**.

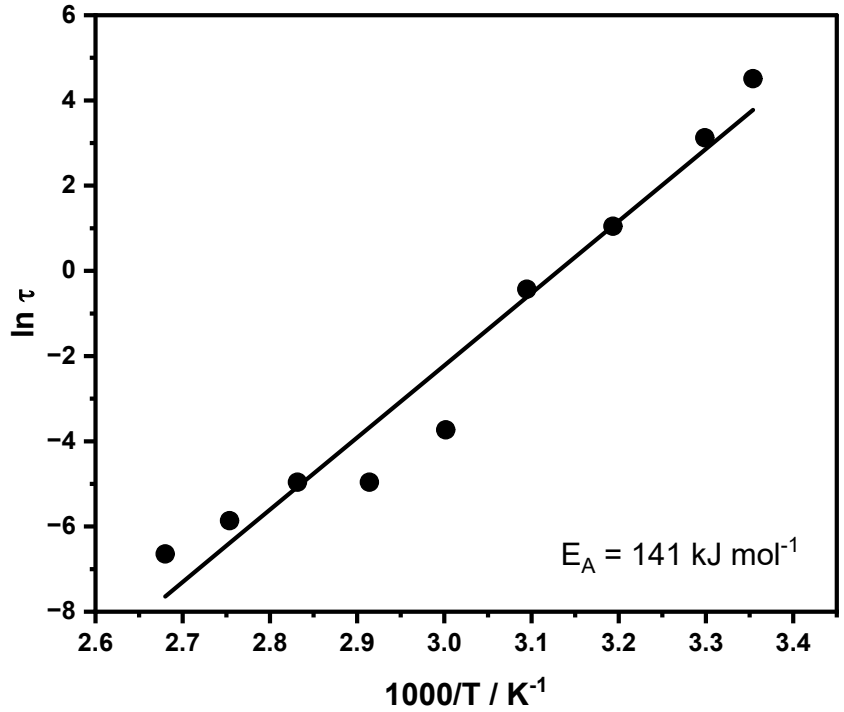

Figure S67. Arrhenius plot of the stress relaxation measurements of **P2-Fe**.

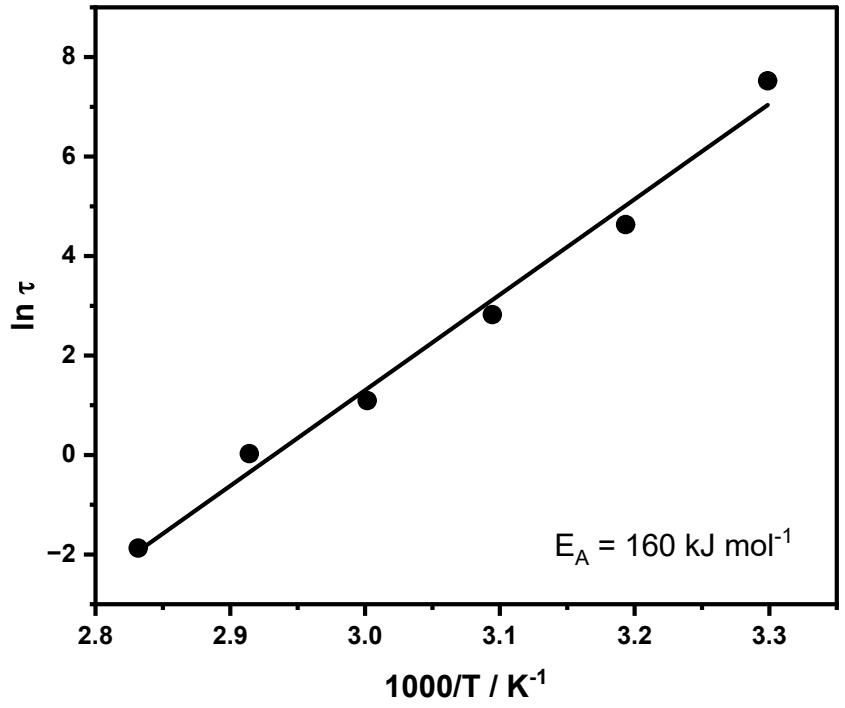

Figure S68. Arrhenius plot of the stress relaxation measurements of **P2-Zn**.

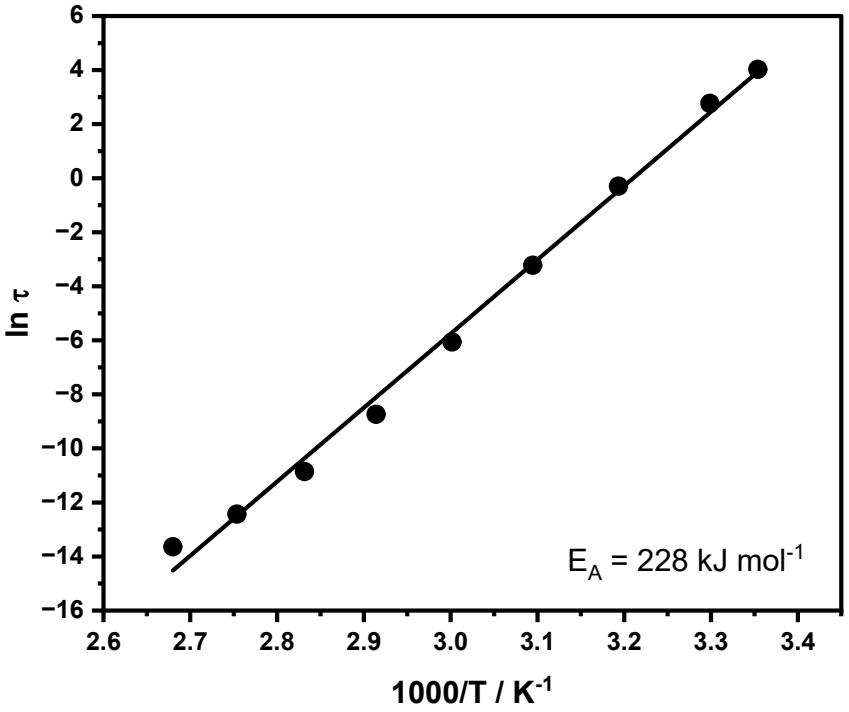

Figure S69. Arrhenius plot of the stress relaxation measurements of **P3-Zn**.

Table S9. Summary of the calculated activation energies (E_A) of the metallopolymers using the TTS approach.

Sample	E_A / kJ mol^{-1}
P1-Fe	154
P1-Zn	136
P2-Fe	141
P2-Zn	160
P3-Zn	228

9 Time temperature superposition (TTS)

The results of the frequency sweep measurements were utilized for time temperature superposition (TTS). First, the resulting data was plotted in a modified Cole-Cole format. The results are shown in **Figure S70** to **S77**. These plots indicate temperature-independent behavior and make TTS applicable. For the master curves a reference temperature (T_{ref}) was chosen at the middle temperature of the measured temperature range. The horizontal and/or vertical shift factors (a_T and b_T) were determined by shifting the data to achieve overlap. As good superposition was observed primarily in the low-frequency region, only this range (typically 0.00628 to 6.28 rad s^{-1}) was used for plotting. The resulting master curves are shown in **Figure S78** to **S85**. The utilized reference temperatures and shift factors are summarized in **Table S10**. Data processing and analysis were carried out using Origin 2024b. To validate the master curves, van Gurp-Palmen plots were constructed. The resulting plots are presented in **Figure S86** to **S94**.

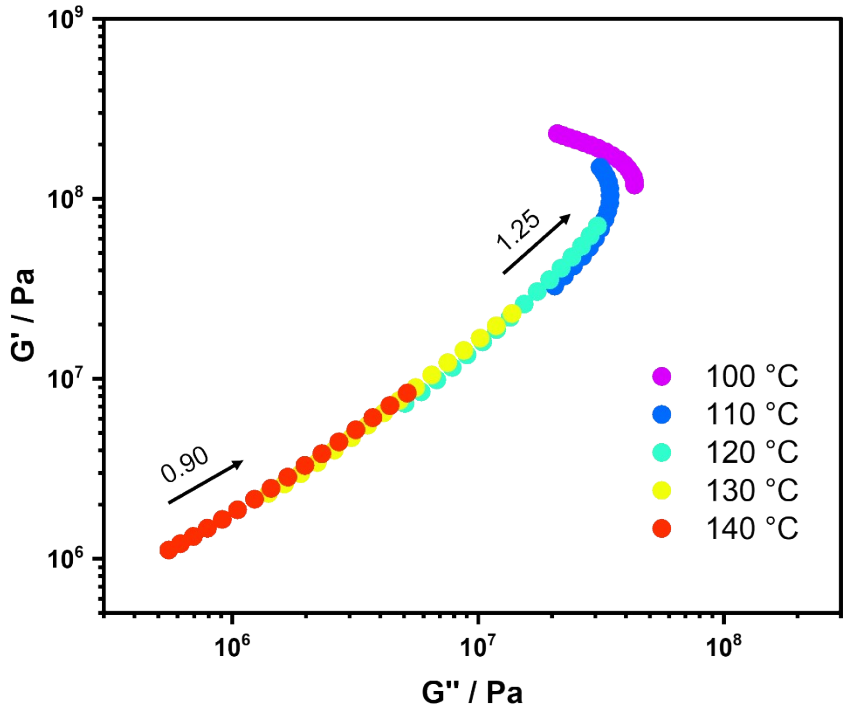

Figure S70. G' to G'' of **P1-Fe** at different temperatures from 0.00628 to 6.28 rad s^{-1} plotted in a modified Cole-Cole format.

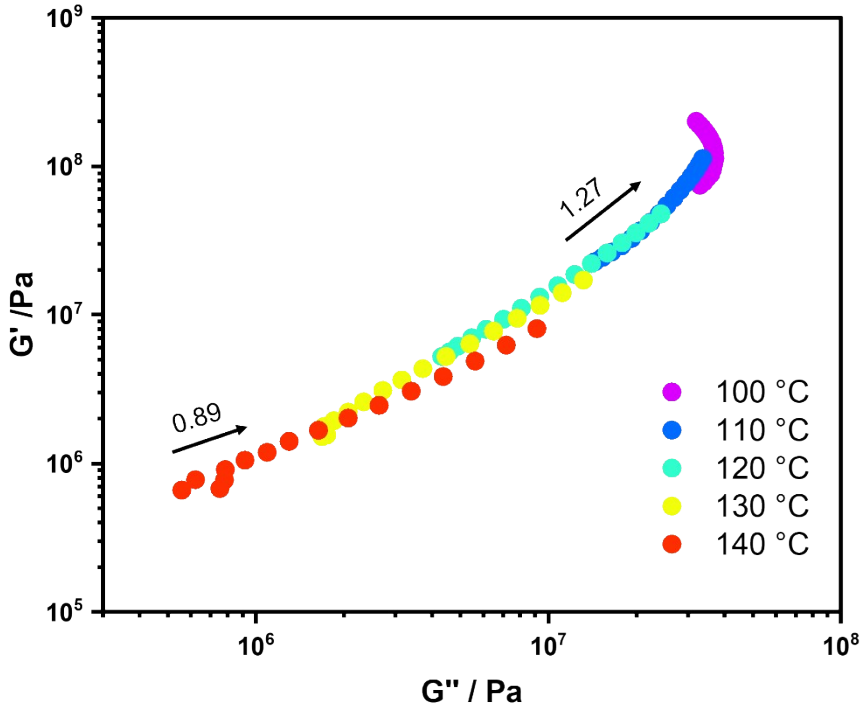

Figure S71. G' to G'' of **P1-Zn** at different temperatures from 0.00628 to 6.28 rad s^{-1} plotted in a modified Cole-Cole format.

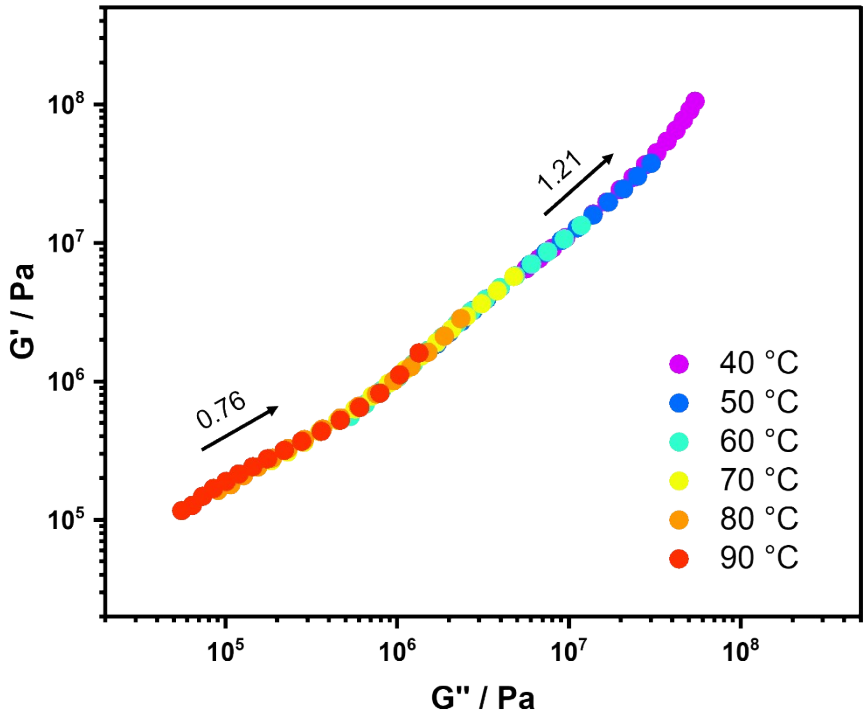

Figure S72. G' to G'' of **P2-Fe** at different temperatures from 0.00628 to 6.28 rad s^{-1} plotted in a modified Cole-Cole format.

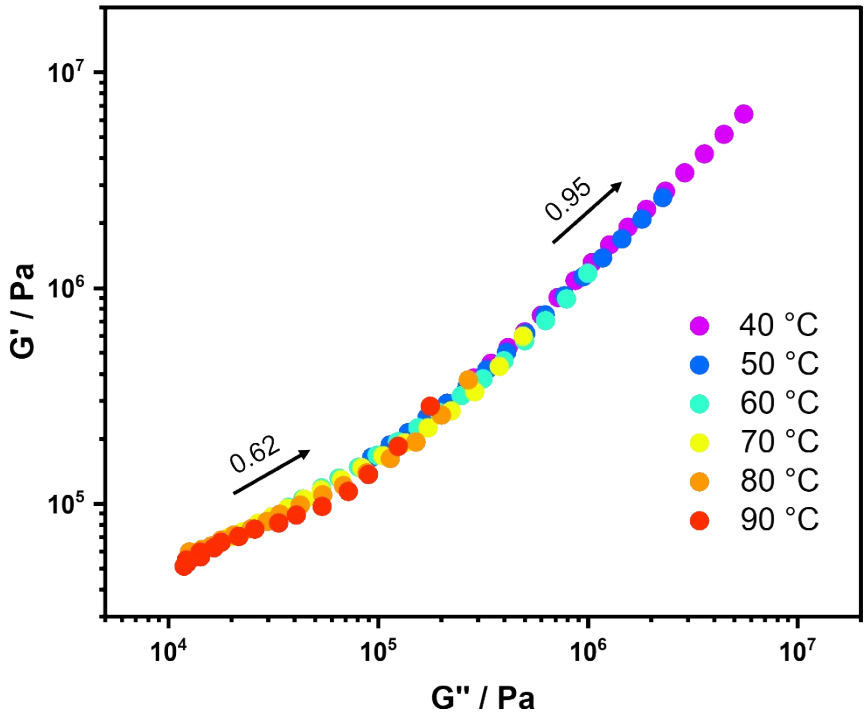

Figure S73. G' to G'' of **P3-Fe** at different temperatures from 0.00628 to 6.28 rad s^{-1} plotted in a modified Cole-Cole format.

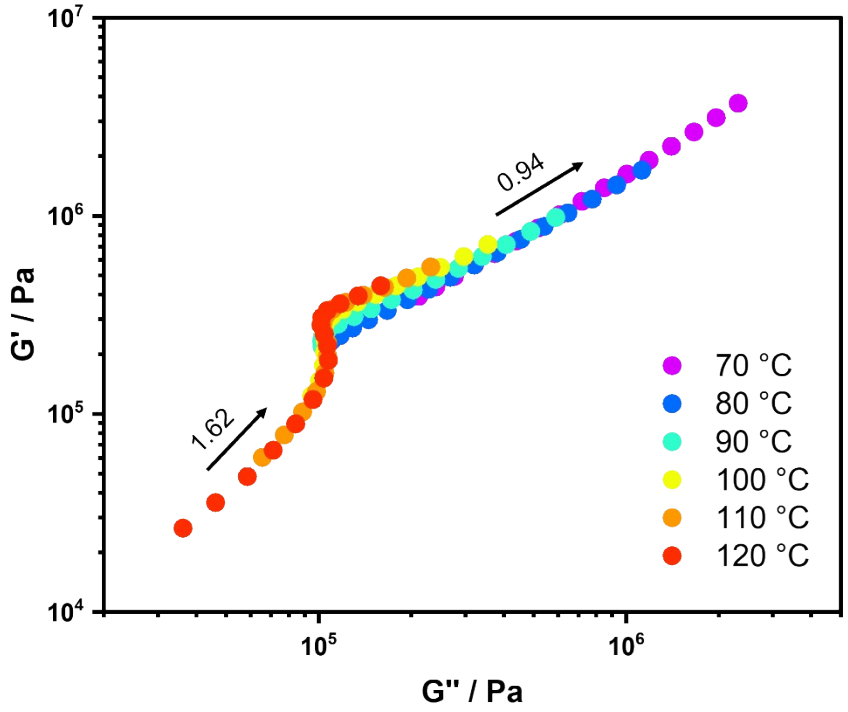

Figure S74. G' to G'' of **P3-Zn** at different temperatures from 0.00628 to 6.28 rad s^{-1} plotted in a modified Cole-Cole format.

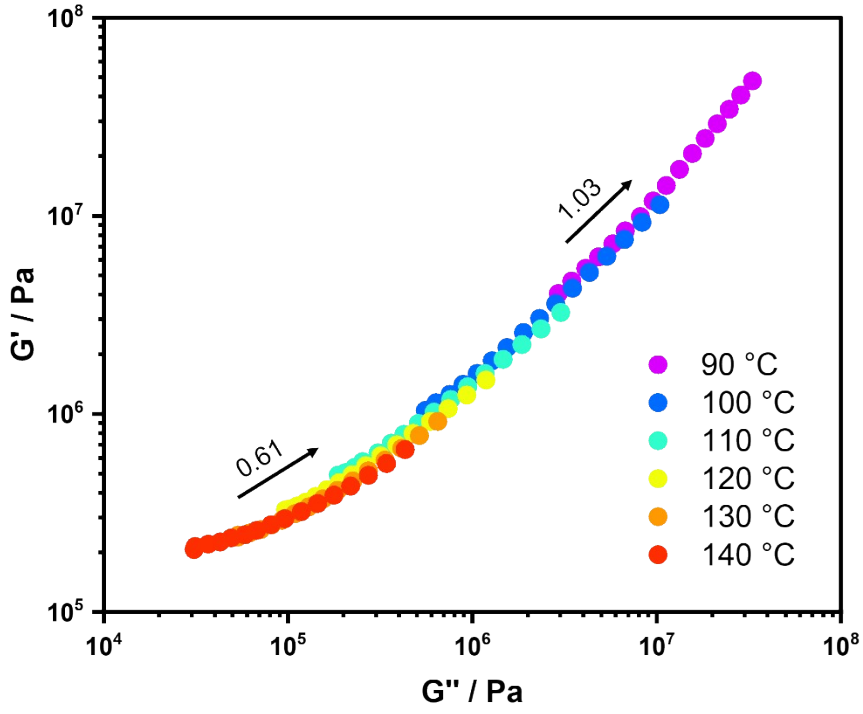

Figure S75. G' to G'' of **P1-cc** at different temperatures from 0.00628 to 6.28 rad s^{-1} plotted in a modified Cole-Cole format.

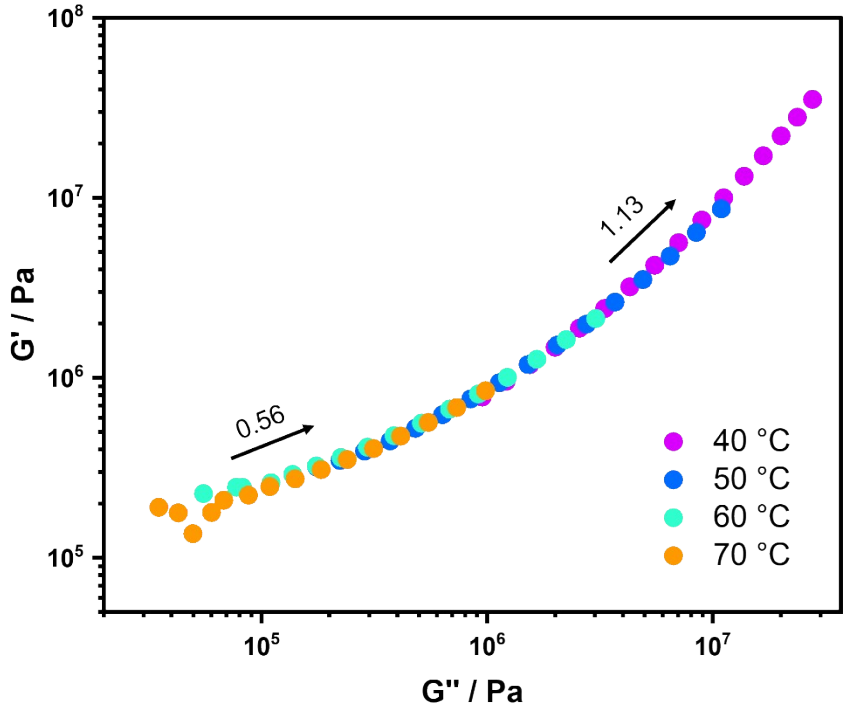

Figure S76. G' to G'' of **P2-cc** at different temperatures from 0.00628 to 6.28 rad s^{-1} plotted in a modified Cole-Cole format.

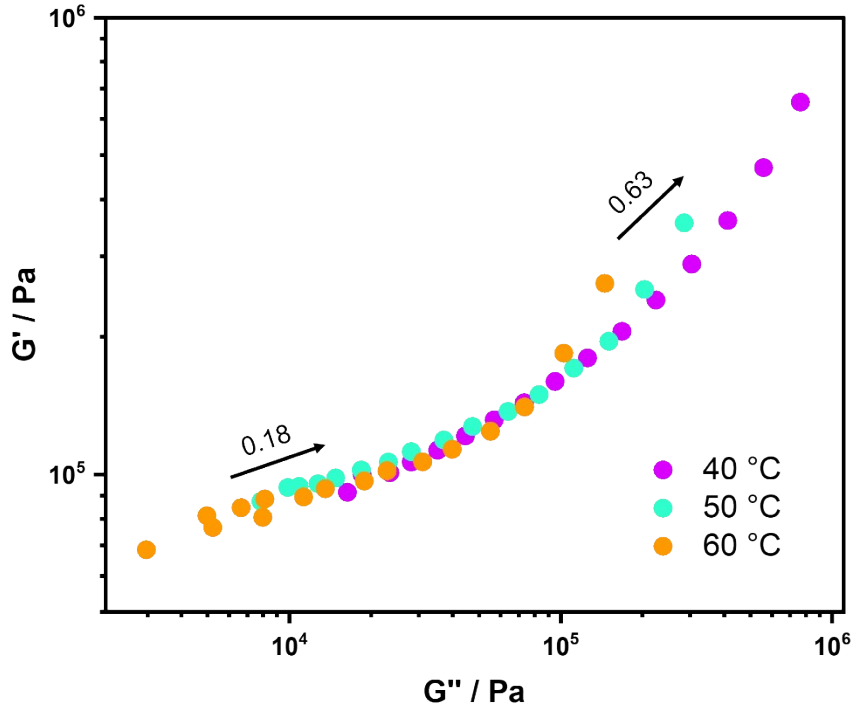

Figure S77. G' to G'' of **P3-cc** at different temperatures from 0.00628 to 6.28 rad s^{-1} plotted in a modified Cole-Cole format.

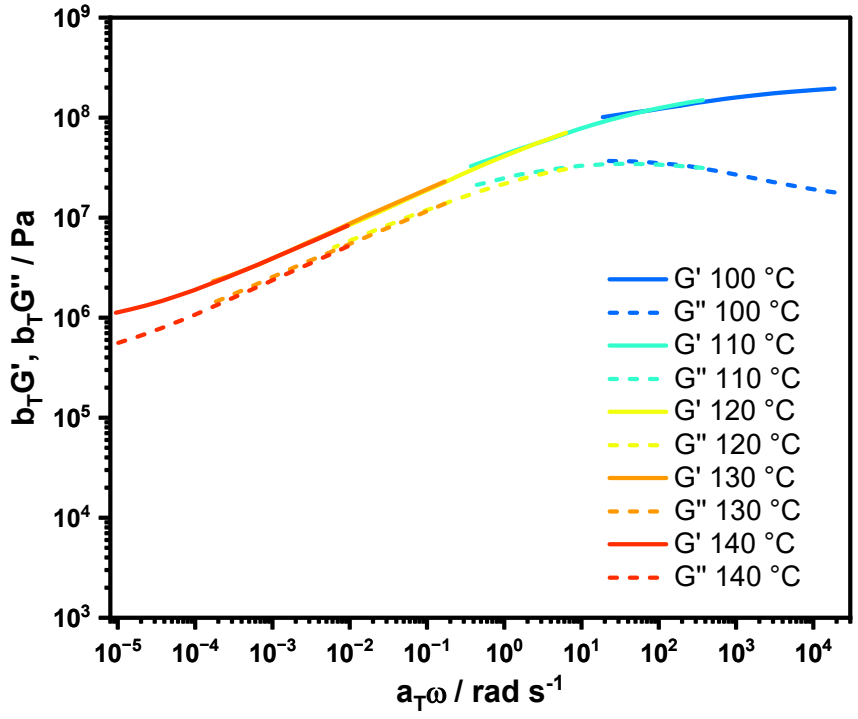

Figure S78. Master curve of **P1-Fe** at T_{ref} = 120 °C from 0.00628 to 6.28 rad s^{-1}.

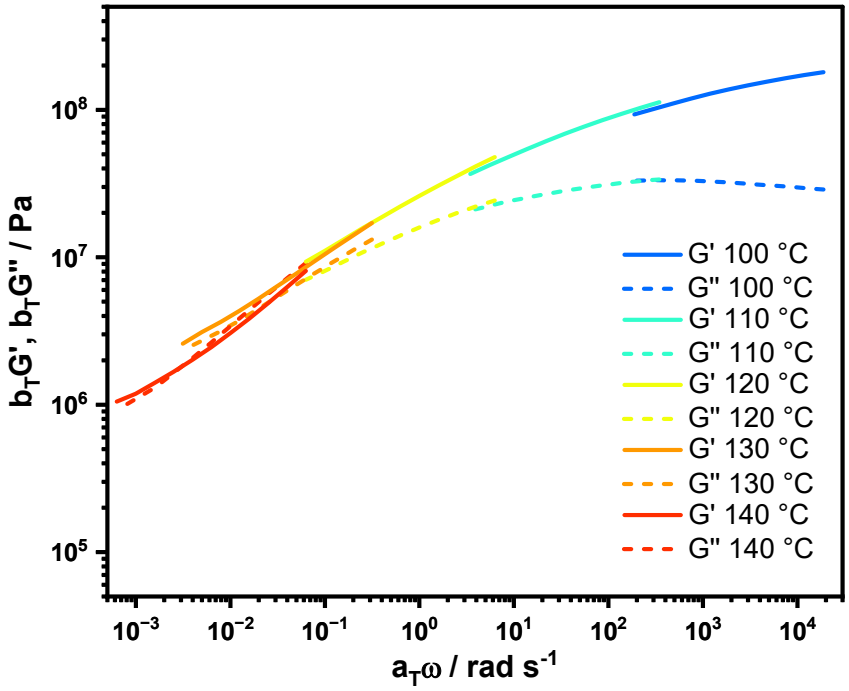

Figure S79. Master curve of **P1-Zn** at T_{ref} = 120 °C from 0.0628 to 6.28 rad s^{-1}.

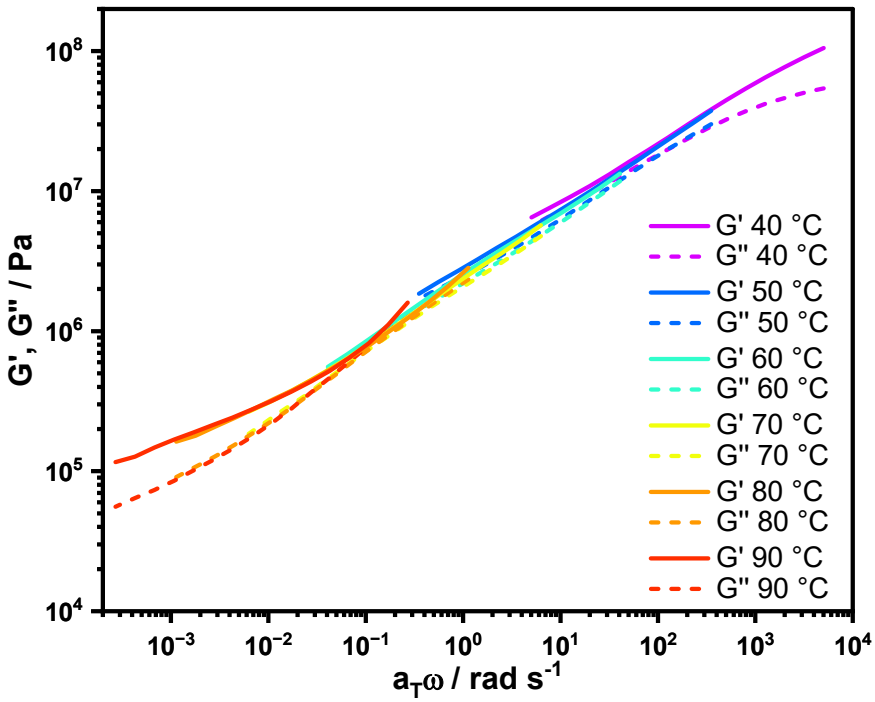

Figure S80. Master curve of **P2-Fe** at T_{ref} = 70 °C from 0.00628 to 6.28 rad s^{-1}.

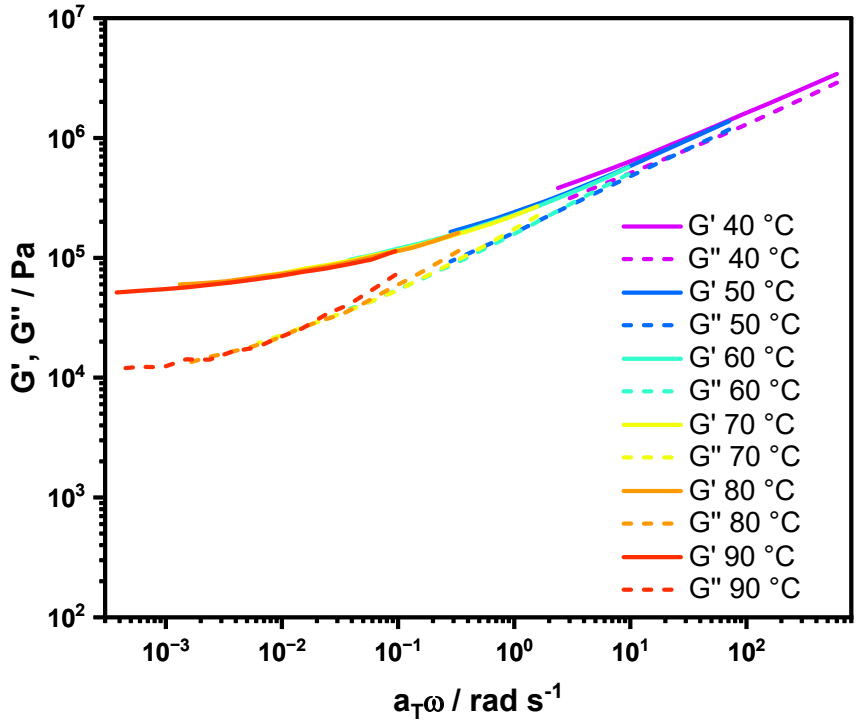

Figure S81. Master curve of **P3-Fe** at T_{ref} = 70 °C from 0.00628 to 1.58 rad s^{-1}.

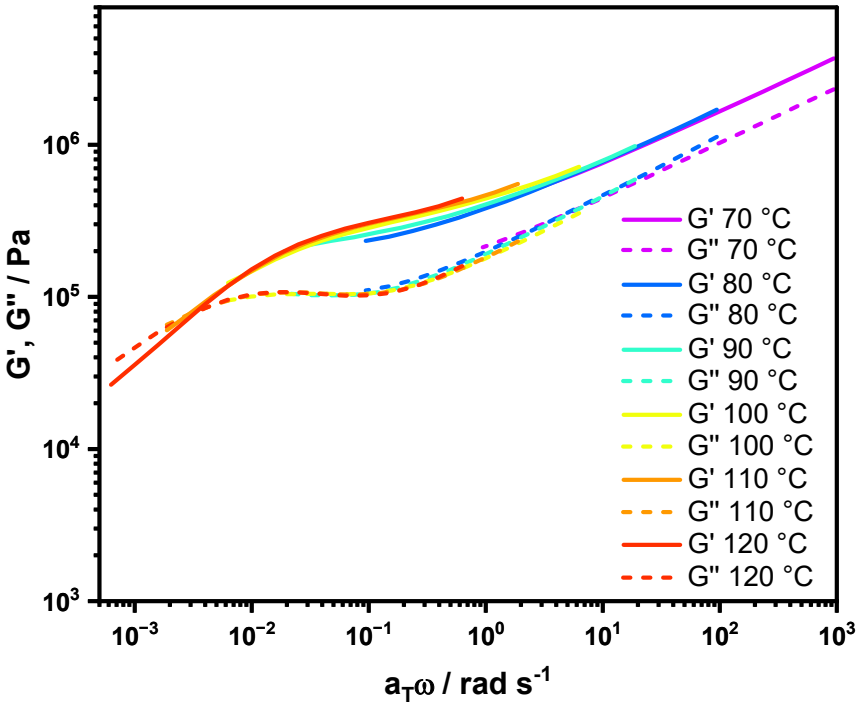

Figure S82. Master curve of **P3-Zn** at T_{ref} = 100 °C from 0.00628 to 6.28 rad s^{-1}.

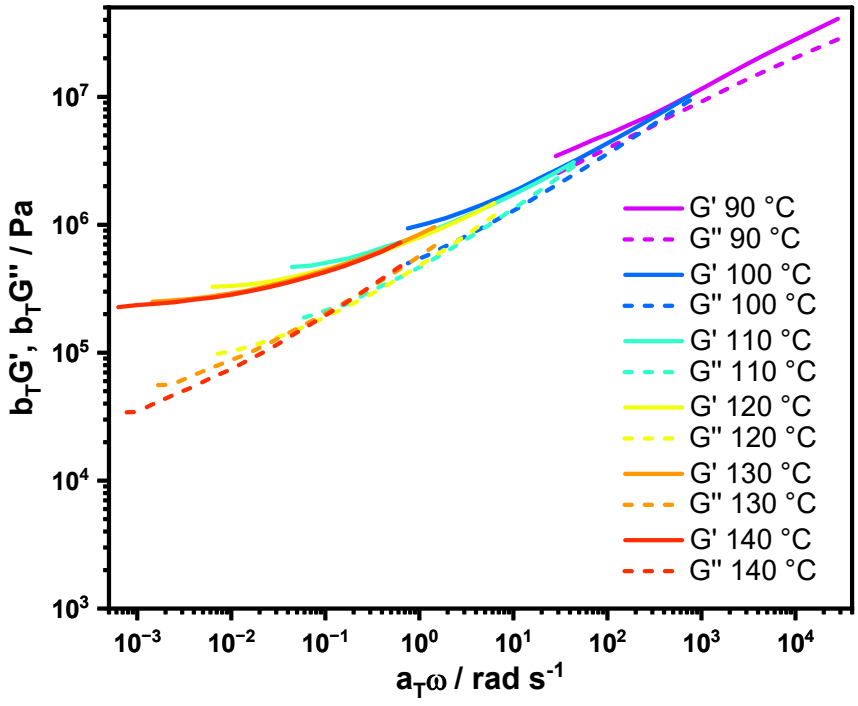

Figure S83. Master curve of **P1-cc** at T_{ref} = 120 °C from 0.00628 to 6.28 rad s^{-1}.

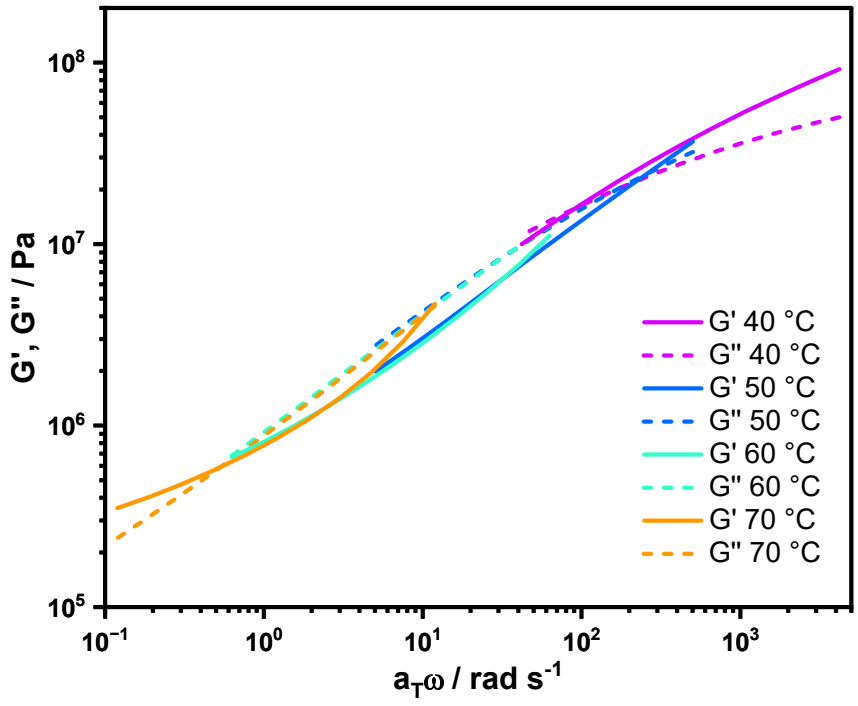

Figure S84. Master curve of **P2-cc** at T_{ref} = 60 °C from 0.628 to 62.8 rad s^{-1}.

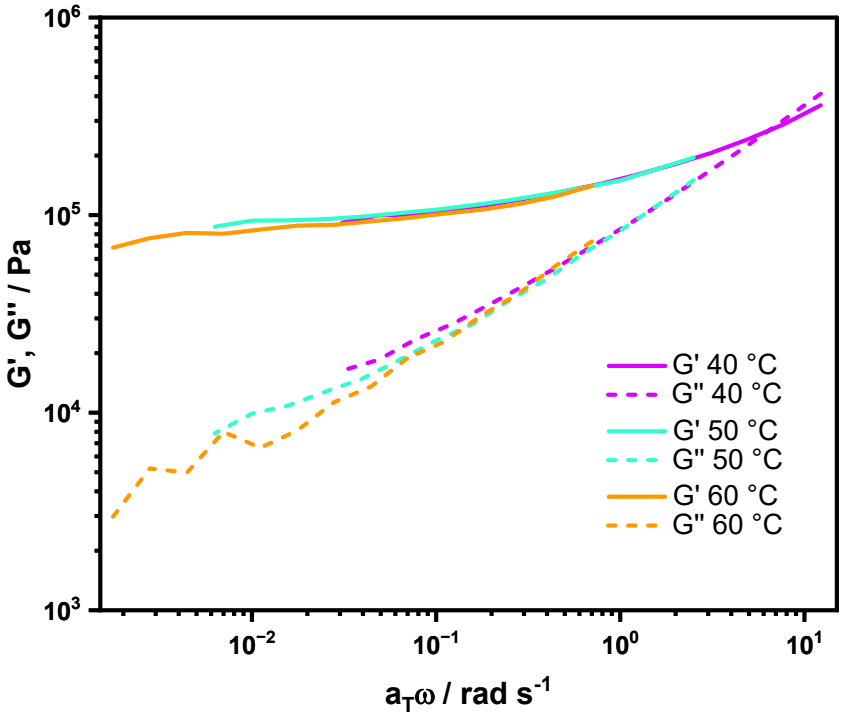

Figure S85. Master curve of **P3-cc** at T_{ref} = 50 °C from 0.00628 to 2.5 rad s^{-1}.

Table S10. Summary of the reference temperatures (bold) and shift factors a_T and b_T for the master curves.

P1-Fe	T / °C	100	110	**120**	130	140	
	a_T	3000	59	1	0.027	0.0015	
	b_T	0.85	1	1	1	1	
P1-Zn	T / °C	100	110	**120**	130	140	
	a_T	3000	55	1	0.05	0.01	
	b_T	0.9	1	1	1	1	
P2-Fe	T / °C	40	50	60	**70**	80	90
	a_T	800	56	6.5	1	0.18	0.043
P2-Zn	T / °C	80	90	100	**110**	120	130
	a_T	490	55	7	1	0.21	0.06
P3-Fe	T / °C	40	50	60	**70**	80	90
	a_T	380	45	6.1	1	0.21	0.06
P3-Zn	T / °C	70	80	90	**100**	110	120
	a_T	150	15	3	1	0.3	0.1
P1-cc	T / °C	90	100	110	**120**	130	140
	a_T	4500	120	7	1	0.23	0.1
	b_T	0.85	0.9	0.95	1	1.05	1.1
P2-cc	T / °C	40	50	**60**	70		
	a_T	67	8	1	0.19		
P3-cc	T / °C	40	**50**	60			
	a_T	4.9	1	0.28			

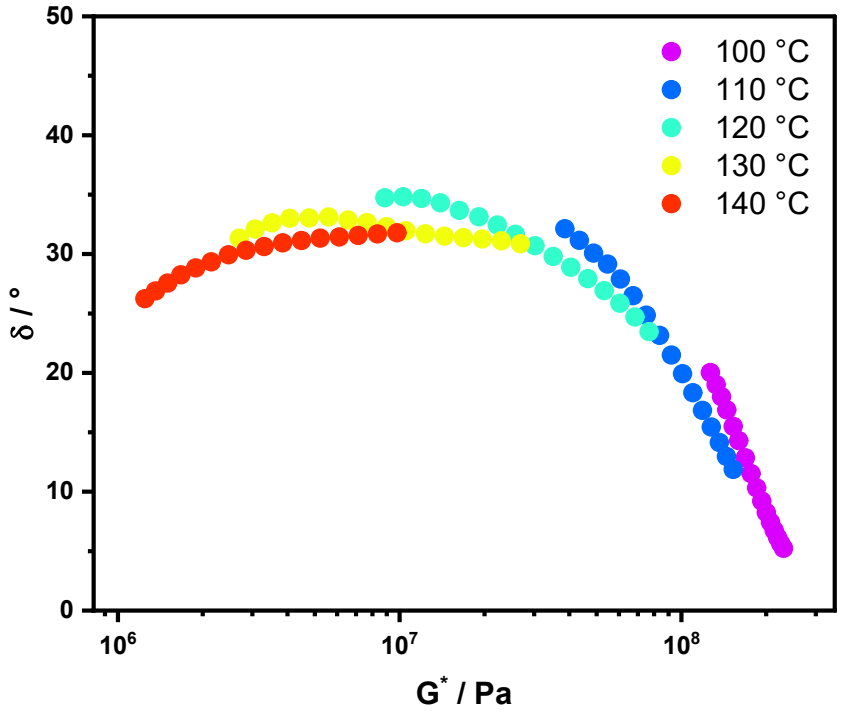

Figure S86. Van Gurp-Palmen plot of **P1-Fe**.

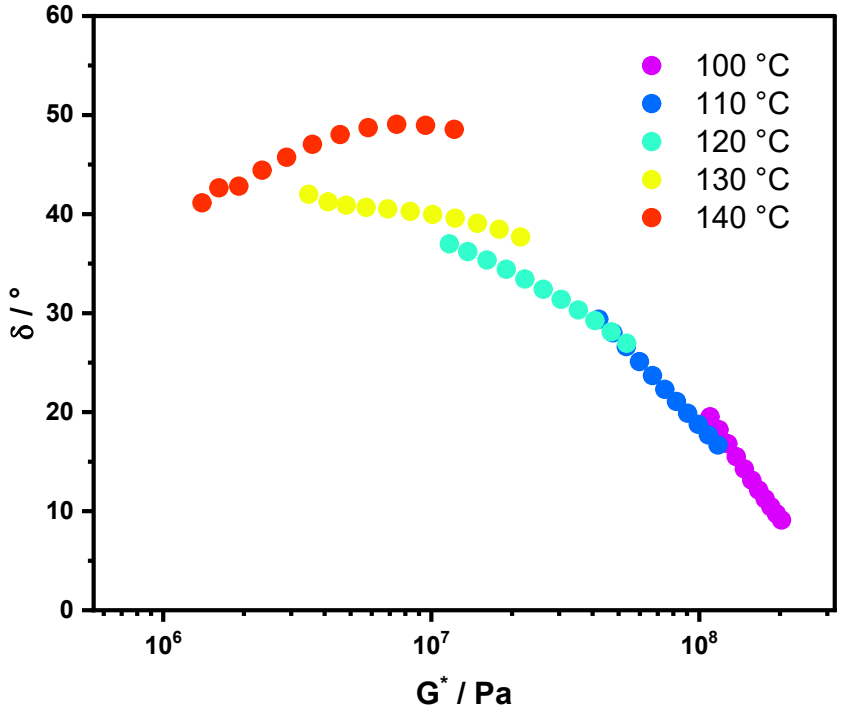

Figure S87. Van Gurp-Palmen plot of **P1-Zn**.

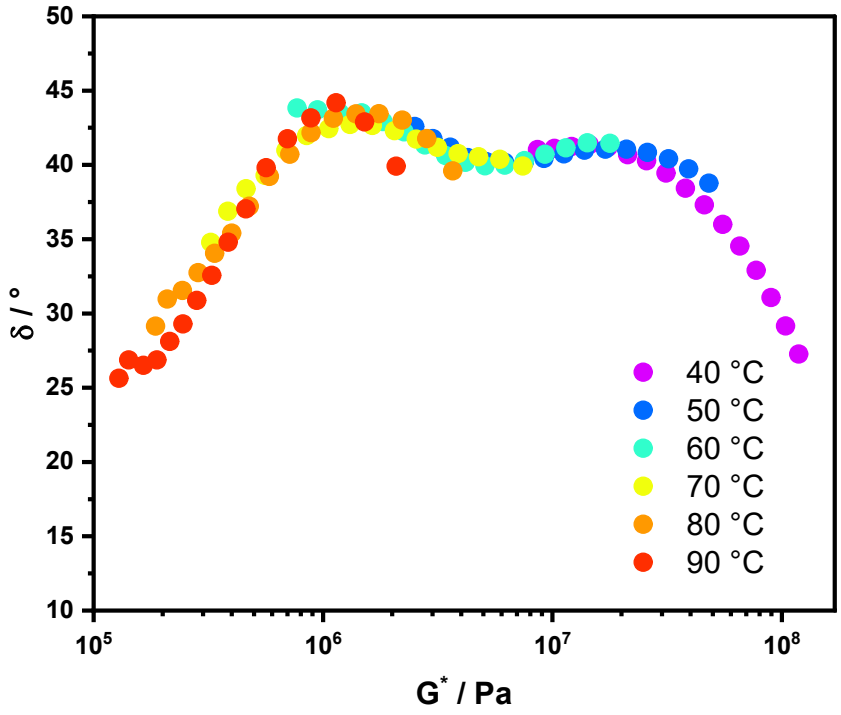

Figure S88. Van Gurp-Palmen plot of **P2-Fe**.

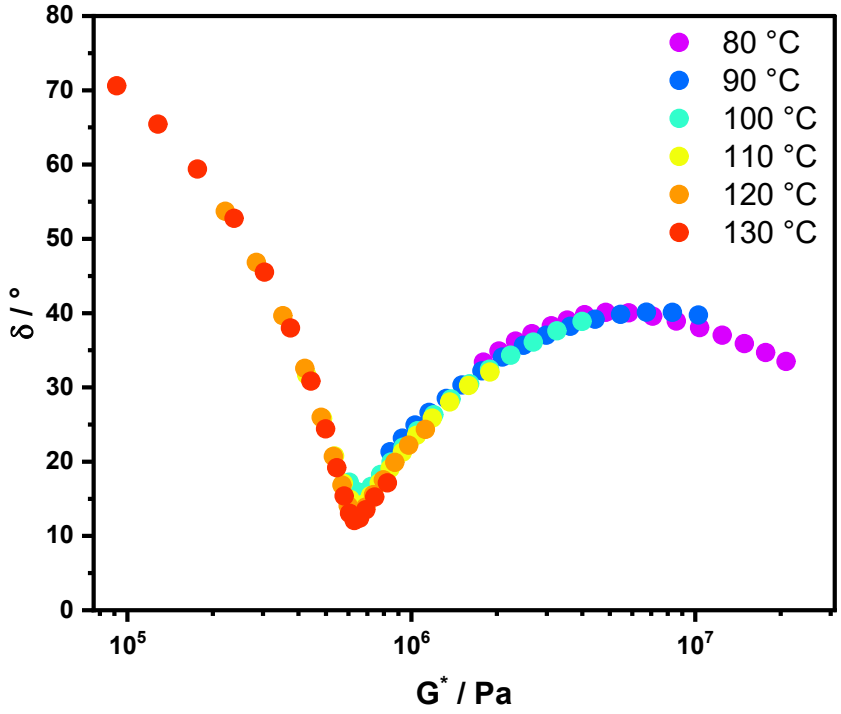

Figure S89. Van Gurp-Palmen plot of **P2-Zn**.

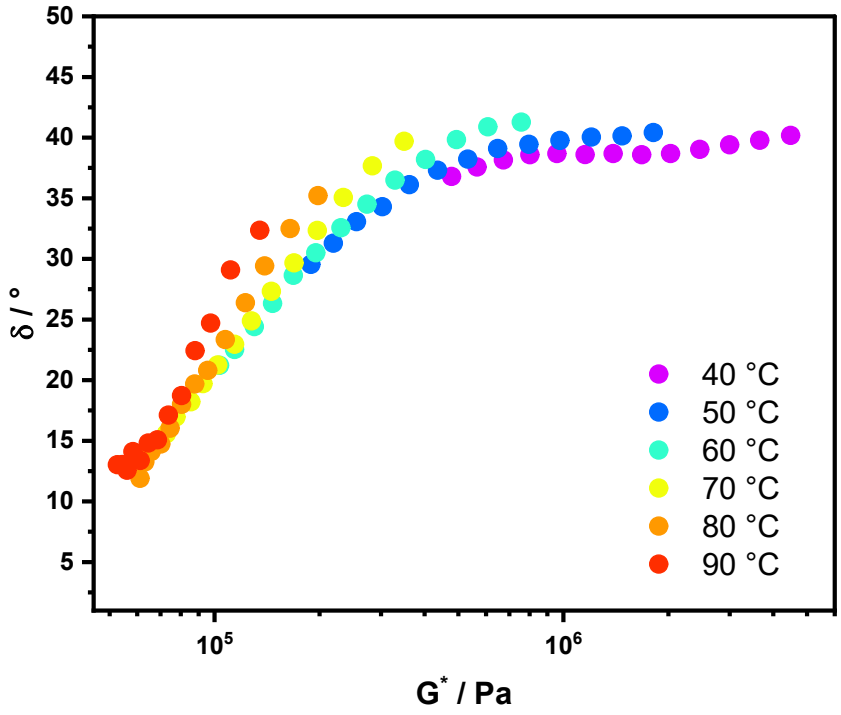

Figure S90. Van Gurp-Palmen plot of **P3-Fe**.

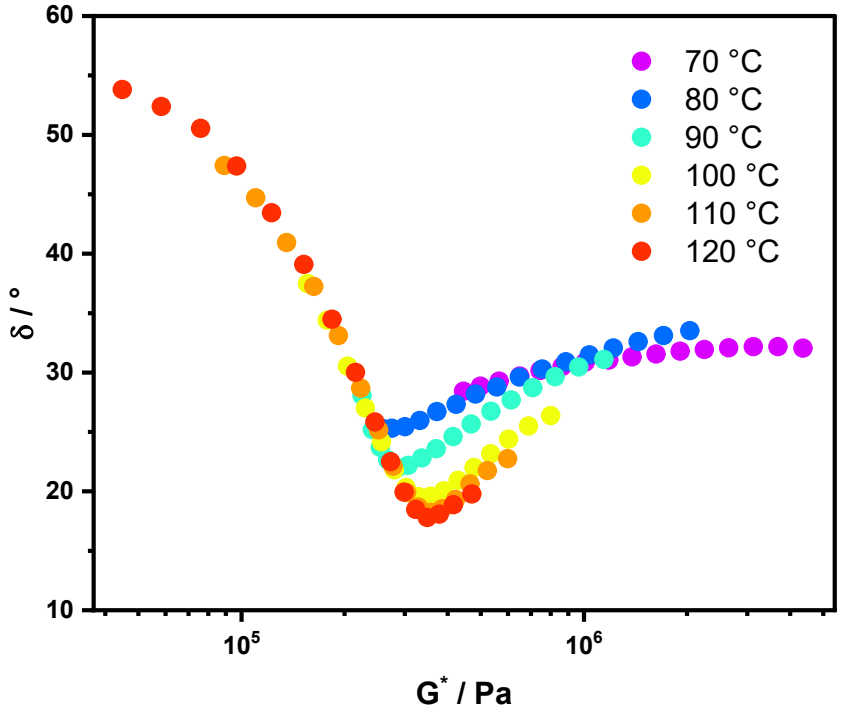

Figure S91. Van Gurp-Palmen plot of **P3-Zn**.

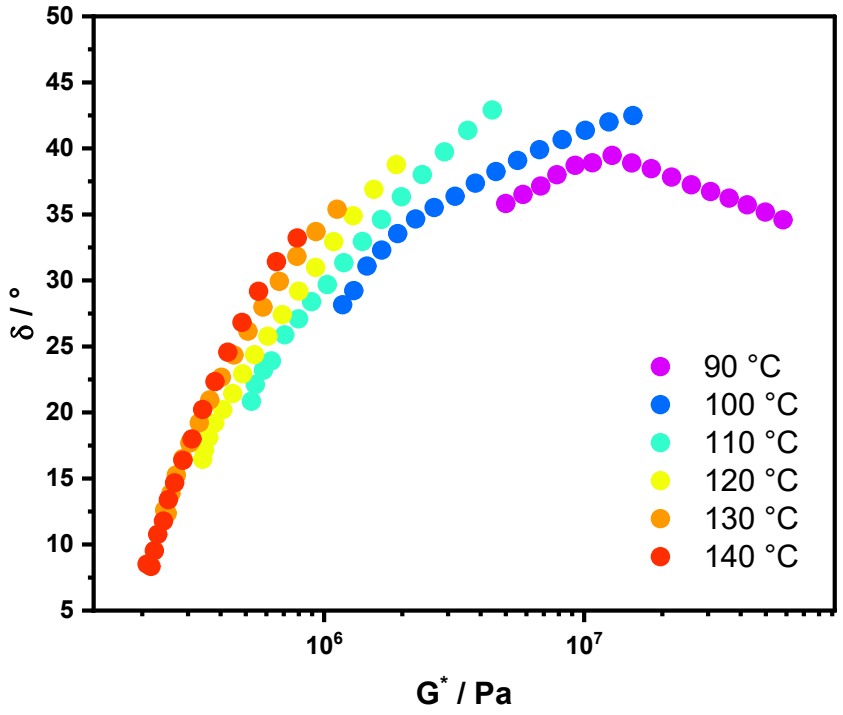

Figure S92. Van Gurp-Palmen plot of **P1-cc**.

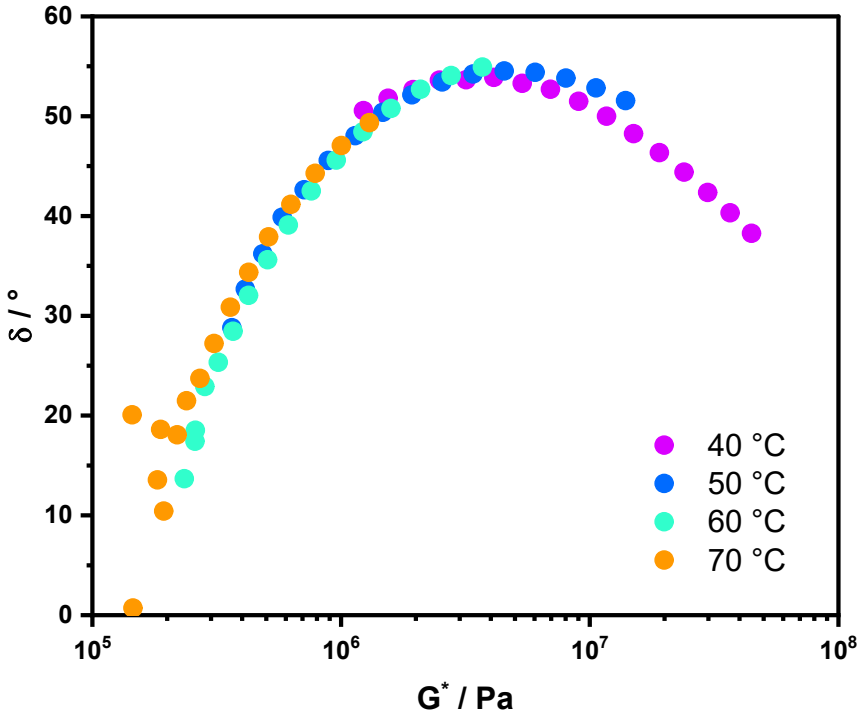

Figure S93. Van Gurp-Palmen plot of **P2-cc**.

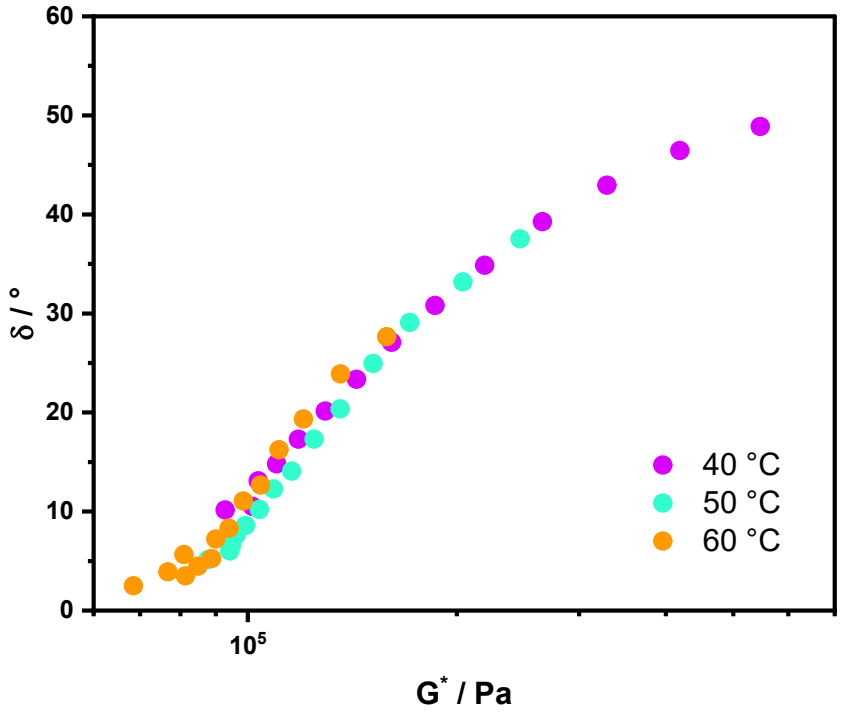

Figure S94. Van Gurp-Palmen plot of **P3-cc**.

10 Williams-Landel-Ferry (WLF) parameters

The Williams-Landel-Ferry (WLF) equation (**S1**) was linearized (**S2**) to enable parameter determination. The shift factors (a_T) were derived from the master curves of the TTS. The data were plotted, and a linear regression was applied. The WLF parameters C_1 and C_2 were obtained from the slope and intercept of the fit. The results of these plots are shown in **Figure S95** to **S103**. Data processing and analysis were carried out using Origin 2024b.

$$\log a_T = \log\left(\frac{\eta}{\eta_r}\right) = -\frac{C_1(T - T_{ref})}{C_2 + (T - T_{ref})} \quad \textbf{(S1)}$$

$$-\frac{1}{\log(a_T)} = \frac{C_2}{C_1(T - T_{ref})}\frac{1}{} + \frac{1}{C_1} \quad \textbf{(S2)}$$

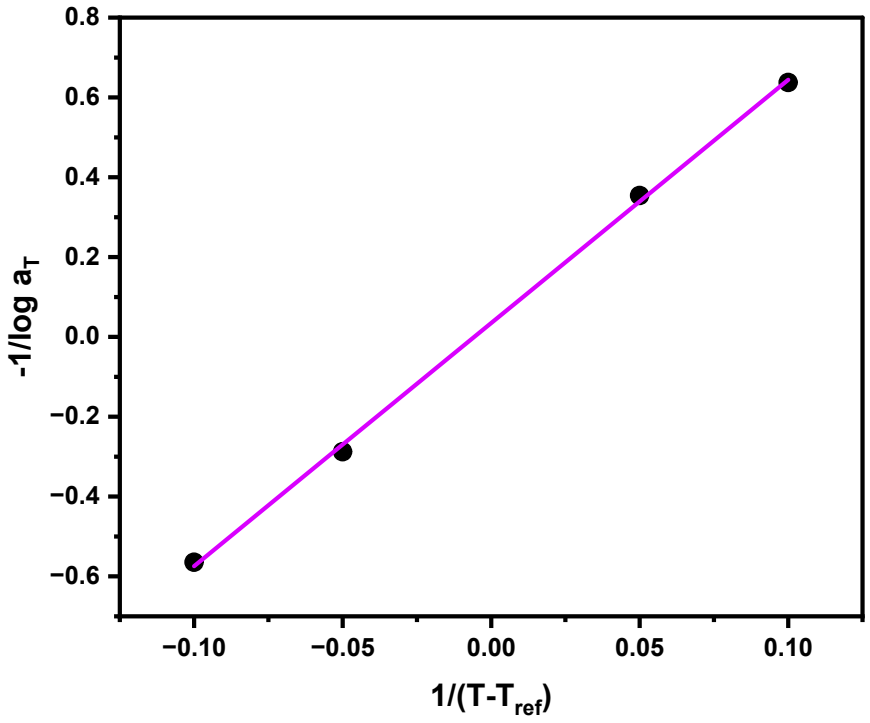

Figure S95. Linear WLF fit for C_1 and C_2 of **P1-Fe** (slope = 6.09221 °C, intercept = 0.03483).

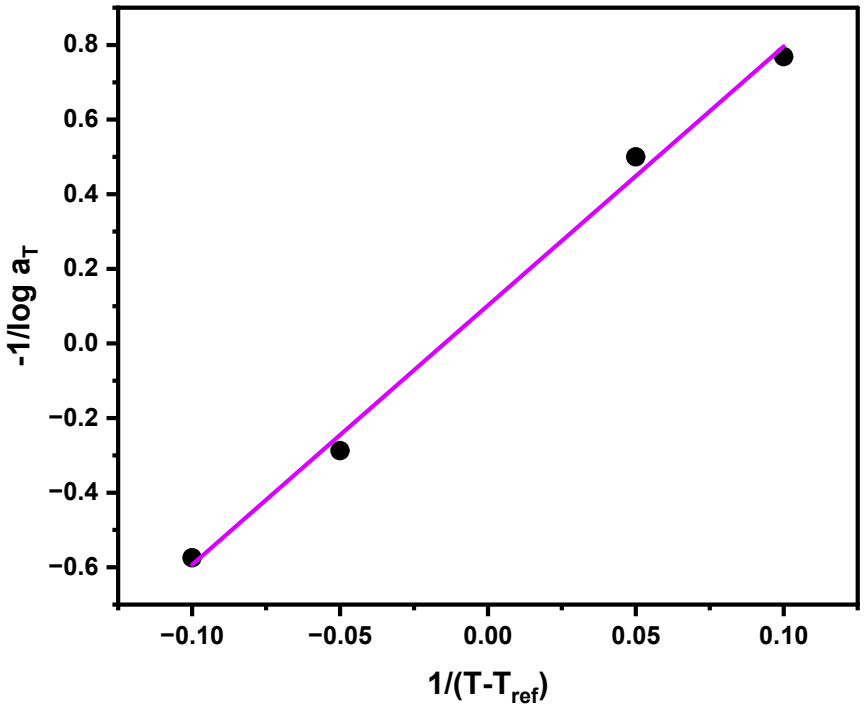

Figure S96. Linear WLF fit for C_1 and C_2 of **P1-Zn** (slope = 6.94805 °C, intercept = 0.10161).

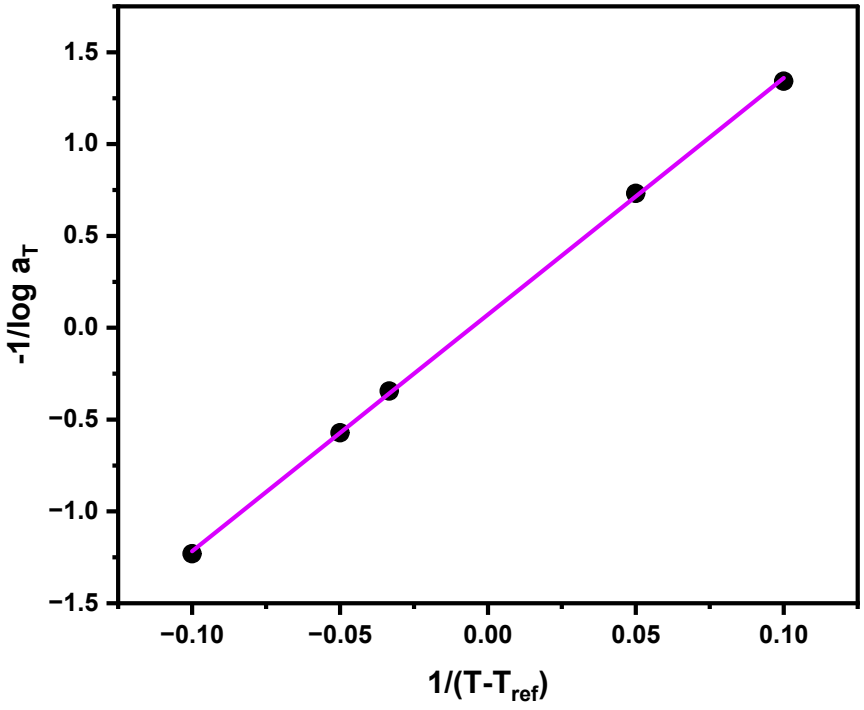

Figure S97. Linear WLF fit for C_1 and C_2 of **P2-Fe** (slope = 12.88133 °C, intercept = 0.07146).

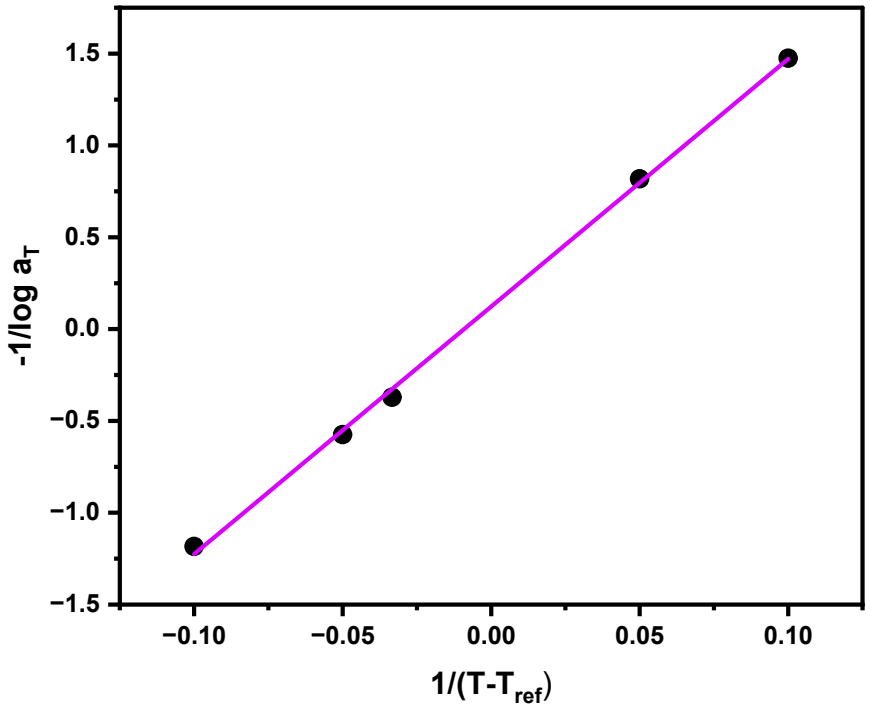

Figure S98. Linear WLF fit for C_1 and C_2 of **P2-Zn** (slope = 13.48094 °C, intercept = 0.12272).

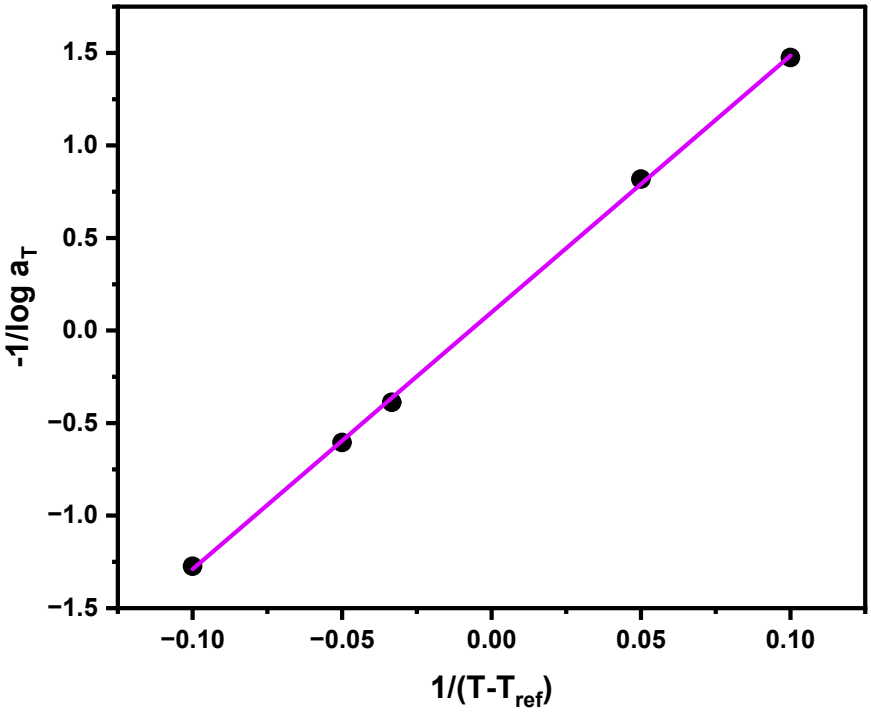

Figure S99. Linear WLF fit for C_1 and C_2 of **P3-Fe** (slope = 13.87269 °C, intercept = 0.09808).

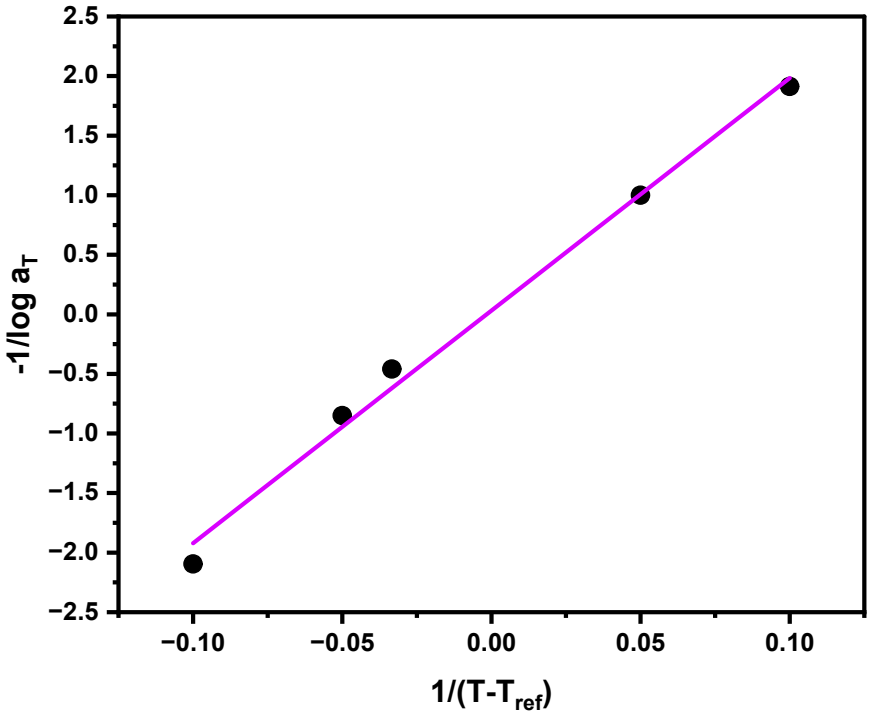

Figure S100. Linear WLF fit for C_1 and C_2 of **P3-Zn** (slope = 19.52122 °C, intercept = 0.0315).

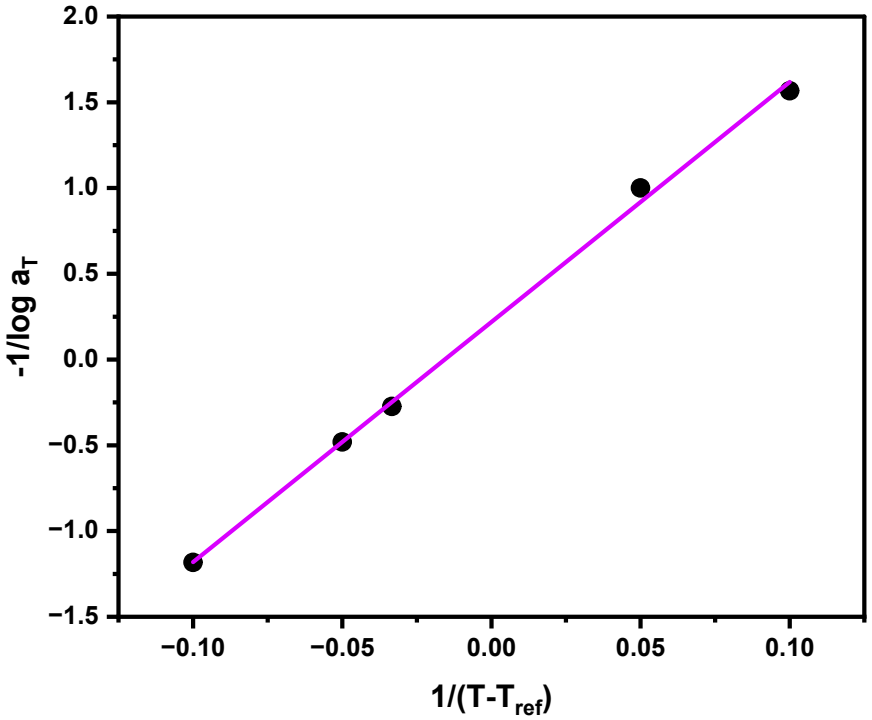

Figure S101. Linear WLF fit for C_1 and C_2 of **P1-cc** (slope = 13.99699 °C, intercept = 0.21906).

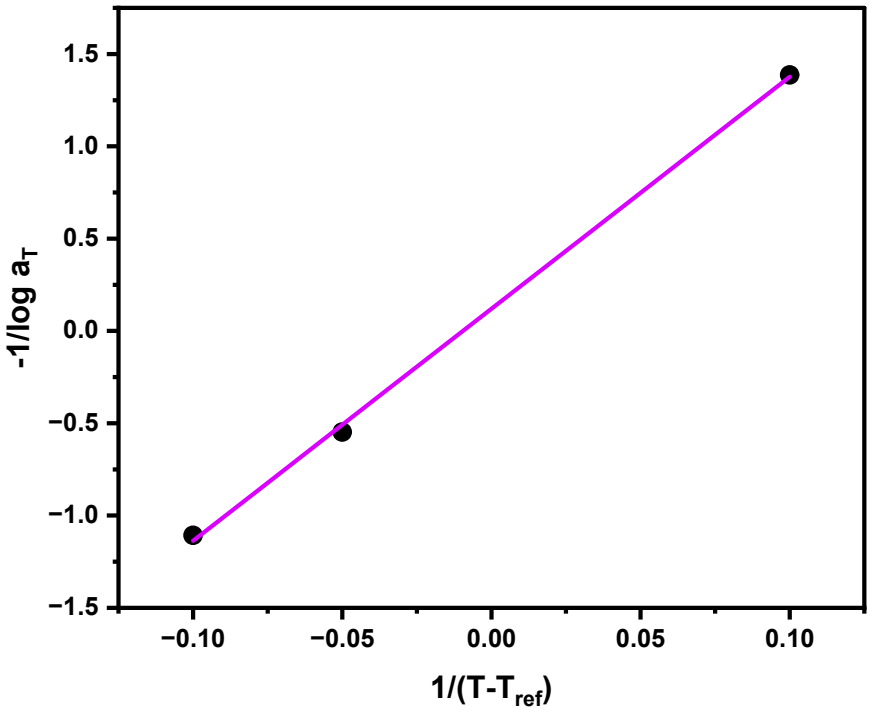

Figure S102. Linear WLF fit for C_1 and C_2 of **P2-cc** (slope = 12.56709 °C, intercept = 0.11997).

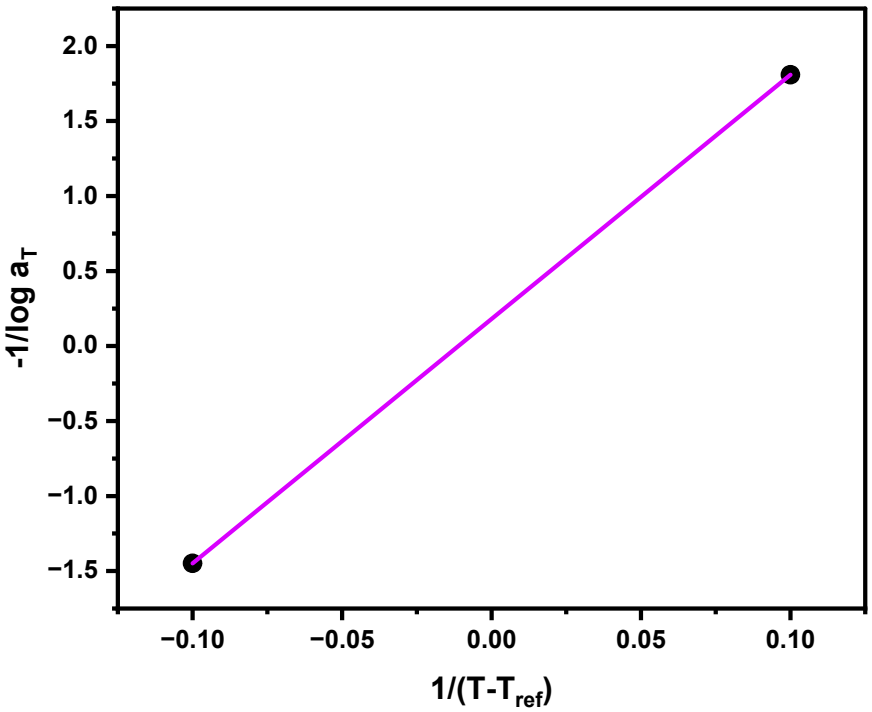

Figure S103. Linear WLF fit for C_1 and C_2 of **P3-cc** (slope = 16.28849 °C, intercept = 0.17999).

11 Computational rheology methods (RheoSpec)

Time temperature superposition

For thermo-rheological simple materials, a change in temperature is equivalent to a scaling of the experimental timescale.[11] Data measured at a temperature *T* can be mapped onto a reference temperature, T_{ref} by shifting the frequency axis by a factor a_T:

$$\omega_{\text{red}} = \omega a_T\left(T, T_{\text{ref}}\right) \qquad \textbf{(S3)}$$

A vertical shift factor, b_T, to correct for density changes is sometimes included but is assumed to be negligible for the polymers in this study.[12] This principle allows isothermal data sets to be collapsed onto a single, smooth master curve.

The temperature dependence of the shift factor a_T near the glass transition temperature (T_g) is often described by the Williams–Landel–Ferry (WLF) equation (see **Equation S1**),[13] where C_1 and C_2 are empirical material constants specific to the chosen T_{ref}.

The horizontal shift $\delta = \log_{10} a_T$ for each non-reference temperature is determined by minimizing a log-space root-mean-square (RMS) error against the progressively constructed master curve. The objective function is:

$$\text{RMSE}(\delta) = \sqrt{\frac{1}{N_{\text{overlap}}} \sum_{i=1}^{N_{\text{overlap}}} \left[\left(\log G_i^{'} - \log \hat{G}^{'}\left(\log \omega_i + \delta\right)\right)^2 + \left(\log G_i^{''} - \log \hat{G}^{''}\left(\log \omega_i + \delta\right)\right)^2\right]} \qquad \textbf{(S4)}$$

where ω_i, $G_i^{'}$ and $G_i^{''}$ are the data points in the overlapping frequency range, and $\hat{G}^{'}(\cdot)$ and $\hat{G}^{''}(\cdot)$ are interpolants of the current master curve. This one-dimensional minimization is performed using a robust, bounded scalar optimization algorithm (RheoSpec utilized SciPy's implementation of Brent's method).[14]

Once all shift factors are found, a continuous master curve is generated:

1. Grid generation: A uniform logarithmic frequency grid, (ω_k), is created to span the full range of all shifted data.
2. Weighted averaging: Each shifted dataset is interpolated onto the grid. To ensure a smooth transition between datasets and minimize edge artifacts, a Gaussian weighting function is applied to each dataset before averaging them together. The weight for each dataset is highest at the center of its frequency range and decays towards its edges.
3. Final smoothing: The resulting composite curve is smoothed using a low-order Savitzky–Golay filter to reduce residual noise while preserving key viscoelastic features.[15]

In RheoSpec the final master curve includes the derived quantities of complex viscosity $\eta^*(\omega) = |G^*(\omega)|/\omega$ and loss tangent ($\tan\delta = G^{''}/G^{'}$).

The resulting master curves are shown in **Figure S104** to **S111**.

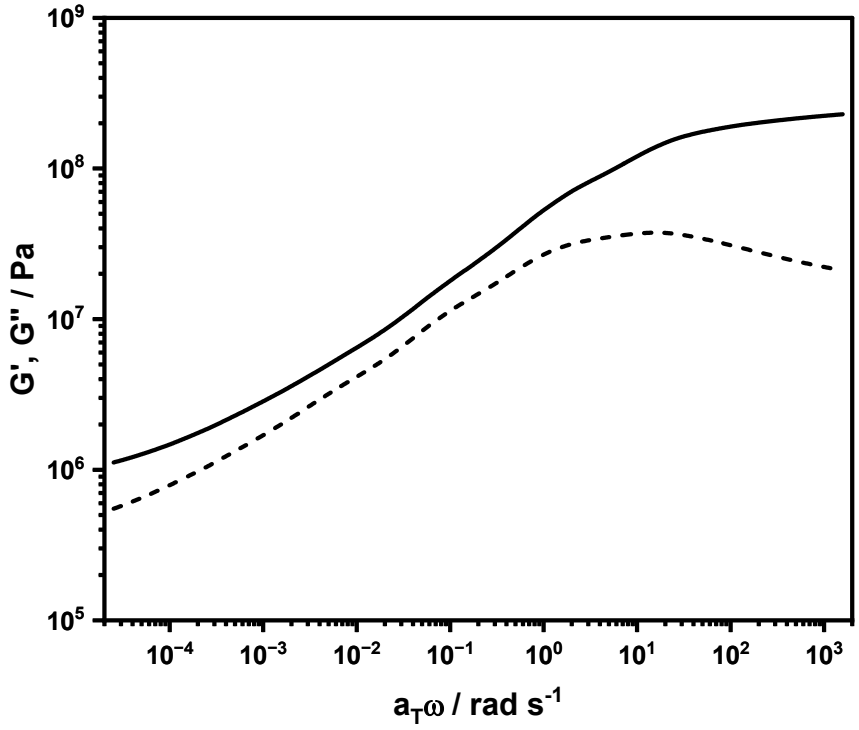

Figure S104. Computational master curve of **P1-Fe** at T_{ref} = 120 °C from 0.00628 to 6.28 rad s^{-1} with the storage modulus G' (black) and the loss modulus G'' (black dotted).

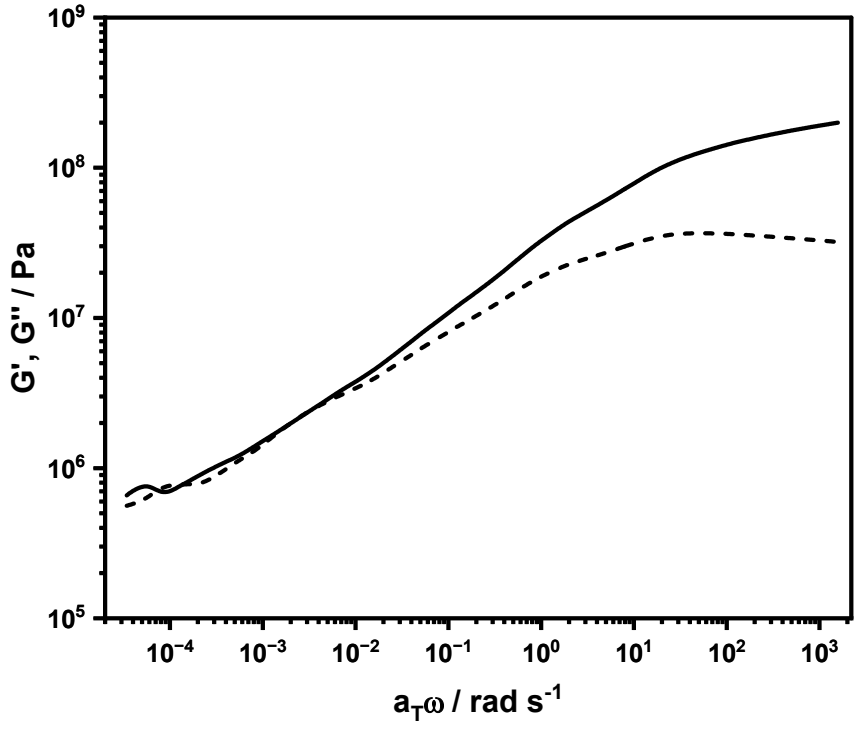

Figure S105. Computational master curve of **P1-Zn** at T_{ref} = 120 °C from 0.0628 to 6.28 rad s^{-1} with the storage modulus G' (black) and the loss modulus G'' (black dotted).

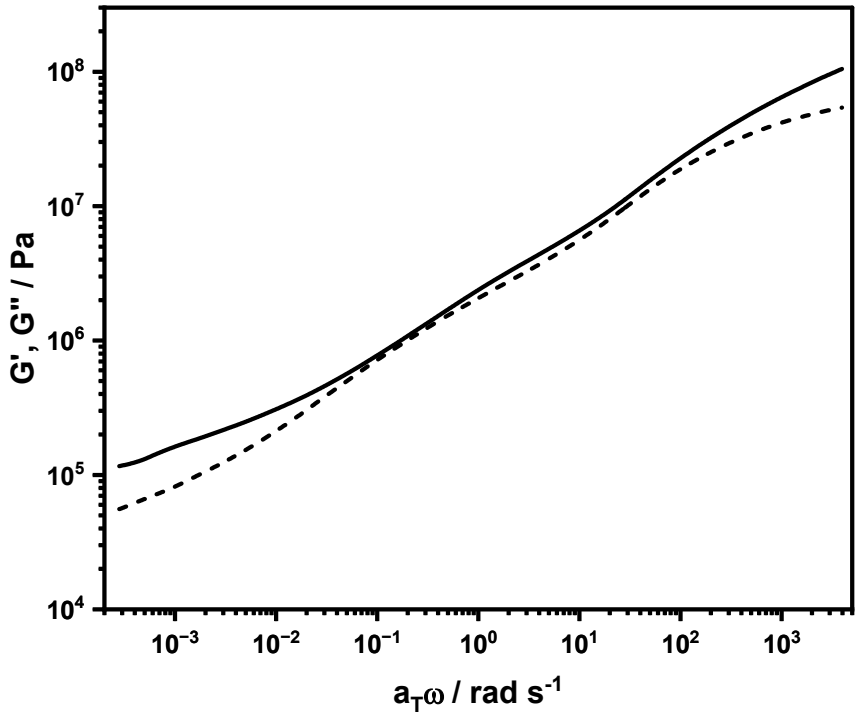

Figure S106. Computational master curve of **P2-Fe** at T_{ref} = 70 °C from 0.00628 to 6.28 rad s^{-1} with the storage modulus G' (black) and the loss modulus G'' (black dotted).

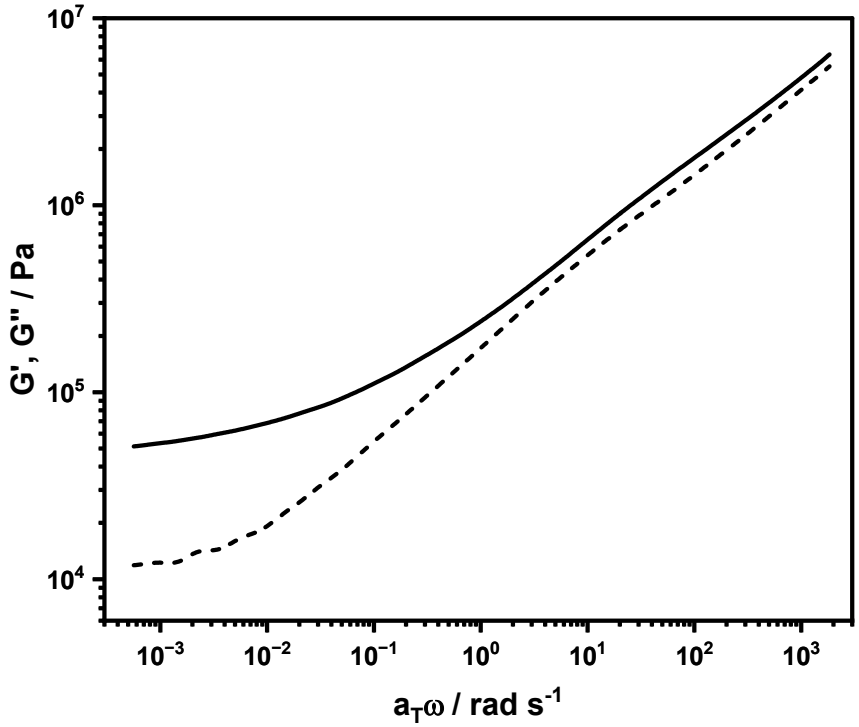

Figure S107. Computational master curve of **P3-Fe** at T_{ref} = 70 °C from 0.00628 to 1.58 rad s^{-1} with the storage modulus G' (black) and the loss modulus G'' (black dotted).

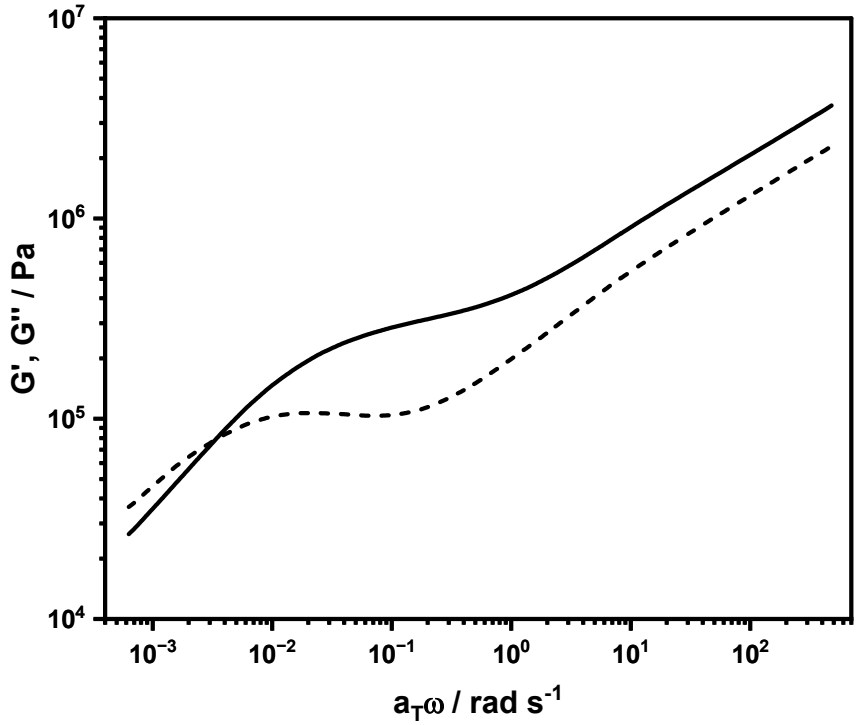

Figure S108. Computational master curve of **P3-Zn** at T_{ref} = 100 °C from 0.00628 to 6.28 rad s^{-1} with the storage modulus G' (black) and the loss modulus G'' (black dotted).

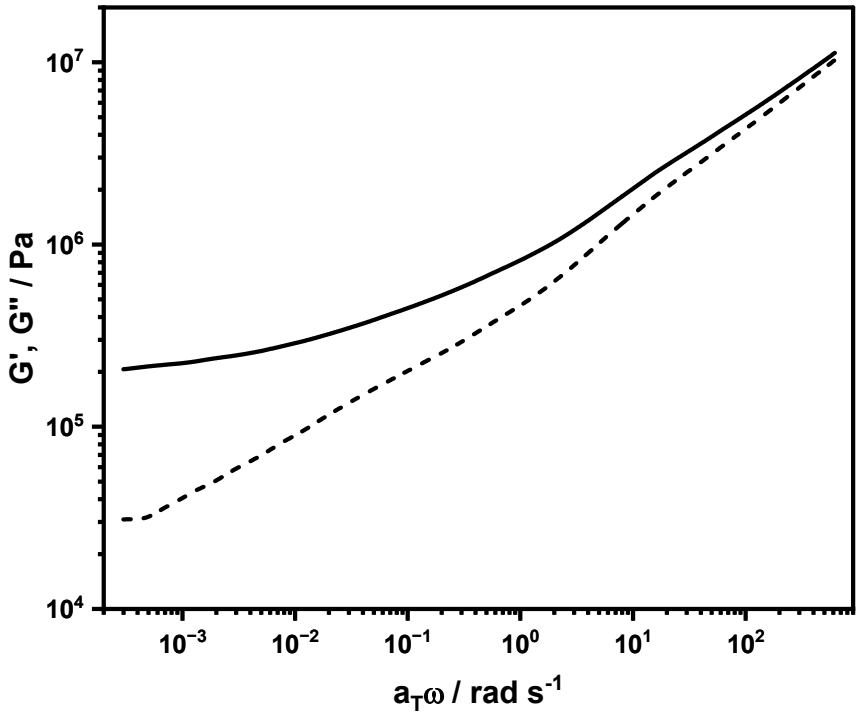

Figure S109. Computational master curve of **P1-cc** at T_{ref} = 120 °C from 0.00628 to 6.28 rad s^{-1} with the storage modulus G' (black) and the loss modulus G'' (black dotted).

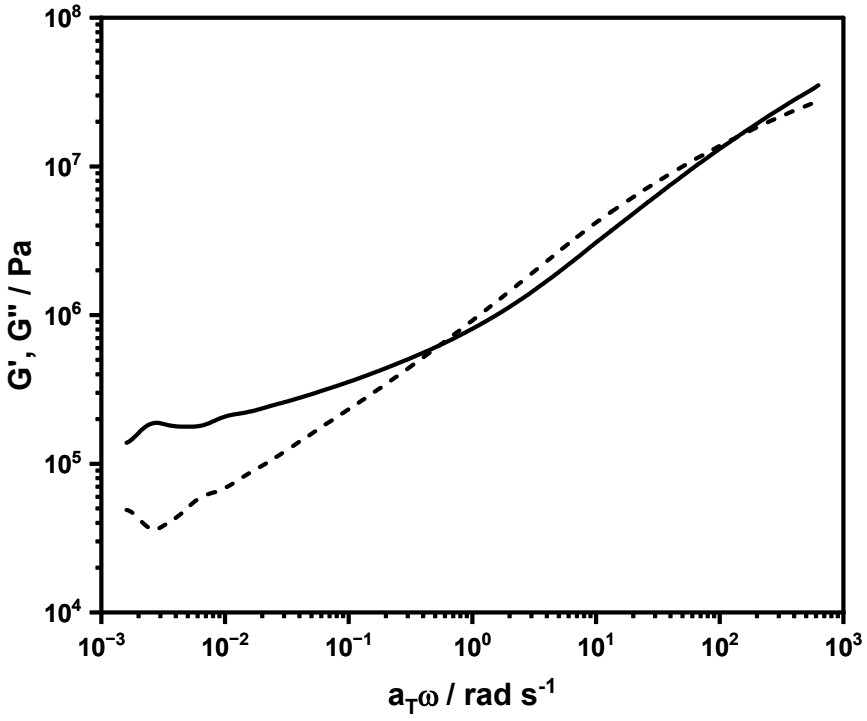

Figure S110. Computational master curve of **P2-cc** at T_{ref} = 60 °C from 0.628 to 62.8 rad s^{-1} with the storage modulus G' (black) and the loss modulus G'' (black dotted).

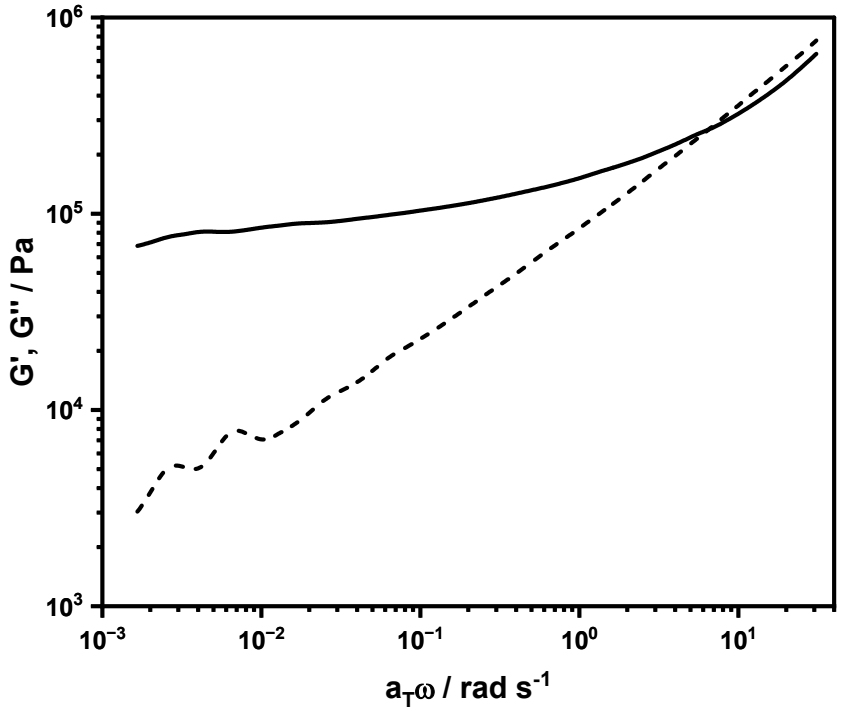

Figure S111. Computational master curve of **P3-cc** at T_{ref} = 50 °C from 0.00628 to 2.5 rad s^{-1} with the storage modulus G' (black) and the loss modulus G'' (black dotted).

Continuous relaxation spectrum

The frequency-dependent moduli of a linear viscoelastic material can be expressed as integrals over the continuous relaxation spectrum $H(\tau)$:[16,17]

$$G'(\omega) = G_e + \int_{-\infty}^{+\infty} H(\tau)\frac{\omega^2\tau^2}{1+\omega^2\tau^2}d(\ln\tau) \quad \textbf{(S5)}$$

$$G''(\omega) = \int_{-\infty}^{+\infty} H(\tau)\frac{\omega\tau}{1+\omega^2\tau^2}d(\ln\tau) \quad \textbf{(S6)}$$

where $H(\tau) \geq 0$ is the relaxation spectrum density (in units of Pa), and $G_e \geq 0$ is the equilibrium modulus, representing a purely elastic contribution for solid-like materials.[18] From the spectrum, macroscopic properties such as the zero-shear viscosity η_0 and the glassy modulus contribution ($G_g - G_e$) can be calculated:

$$\eta_0 = \int_{-\infty}^{+\infty} \tau H(\tau)\, d(\ln\tau), \quad G_g - G_e = \int_{-\infty}^{+\infty} H(\tau)\, d(\ln\tau) \quad \textbf{(S7)}$$

Determining $H(\tau)$ from experimental G',G'' data is a mathematically ill-posed inverse problem, meaning small amounts of noise in the data can cause large changes in the solution. To obtain a stable and physically meaningful result a regularization algorithm can be applied.[19,20]

The integrals are approximated by quadrature over a logarithmically spaced grid of relaxation times, ($\tau_j * j = 1^{n*\tau}$). This transforms the problem into a linear system, ($g = Kh$), where g is the vector of stacked (G',G'') data, h is the vector of unknown spectral amplitudes $H(\tau_j)$, and K is the kernel matrix representing the discretized integrals.

To enforce non-negativity for $H(\tau)$ and ensure a smooth solution, the problem is reparametrized in terms of $h_j = \log H(\tau_j)$, such that $H(\tau_j) = e^{h_j}$ is always positive. The optimal spectrum is found by minimizing a Tikhonov-style objective function that balances data fidelity with solution smoothness:[21]

$$\min_{h,G_0 \geq 0} \Phi(h,G_e;\lambda) = \left\| W\left(1 - \frac{\hat{g}(h,G_e)}{g_{\text{exp}}}\right) \right\|_2^2 + \lambda^2 \|Lh\|_2^2 \quad \textbf{(S8)}$$

With:

- $\hat{g}(h,G_0)$ is the predicted modulus vector using $H(\tau_j) = e^{h_j}$. The misfit term uses relative residuals, making the fit robust to variations in modulus magnitude across many decades.
- W is a diagonal weighting matrix.

- L is a second-difference operator that penalizes the curvature of $\log H(\tau)$, promoting smoothness.
- $\lambda \geq 0$ is the regularization parameter controlling the trade-off between fit quality and smoothness.

This non-linear least-squares problem is solved using a Trust-Region Reflective (TRF) algorithm, which is well-suited for large-scale problems with bound constraints (*e.g.*, $G_e \geq 0$).[14]

The optimal value for λ is determined automatically using a Bayesian evidence framework.[22] This method selects the λ that maximizes the probability of observing the experimental data, thereby providing a principled trade-off between data fidelity and model complexity.

All TTS and spectral analysis procedures described herein were implemented and performed using RheoSpec, a custom software tool developed for this purpose. The numerical back-end relies on algorithms from the SciPy library[14] and utilized functionalities from Numpy,[23] Pandas[24] and Matplotlib[25] including its bounded scalar minimizer and TRF least-squares solver.

The complete source of the program is available online.[26]
https://github.com/JulianKimmig/rheo_spec/

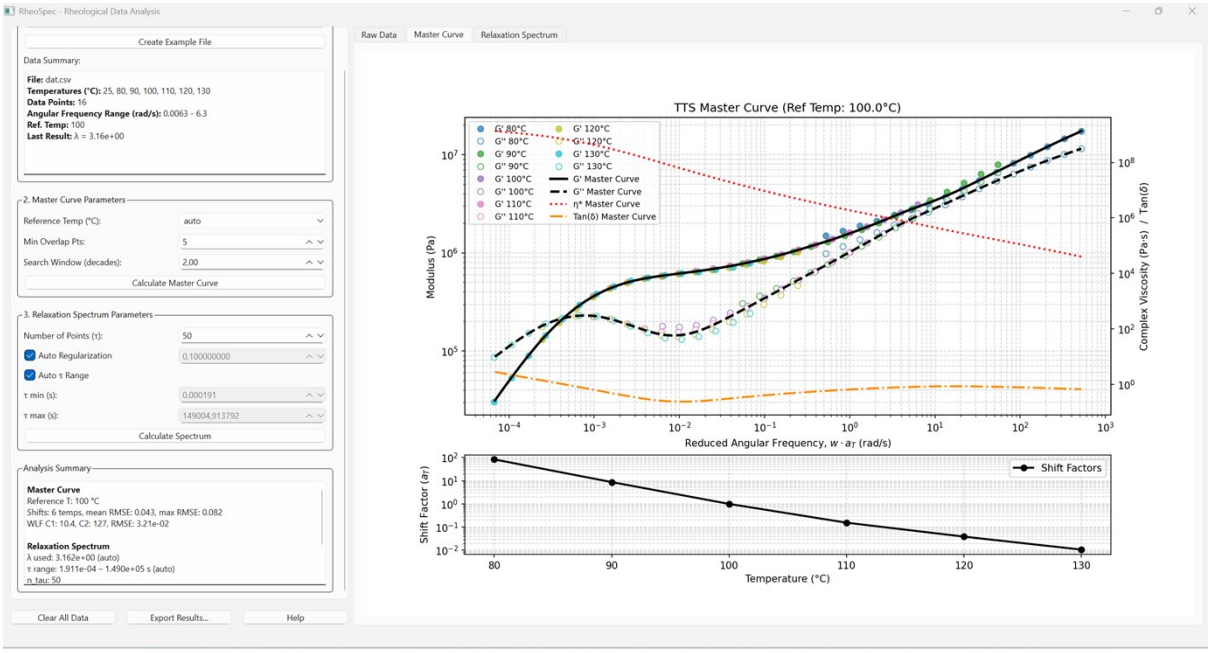

Figure S112. Screenshot of the user interface of RheoSpec.

The resulting relaxation spectra are shown in **Figure S113** to **S125**.

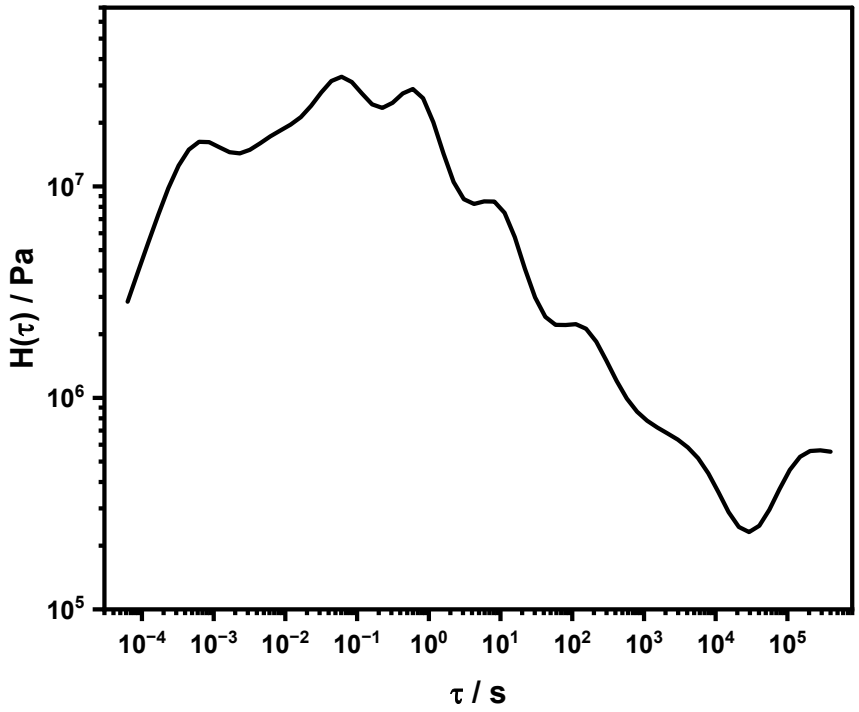

Figure S113. Computational relaxation spectrum of **P1-Fe**.

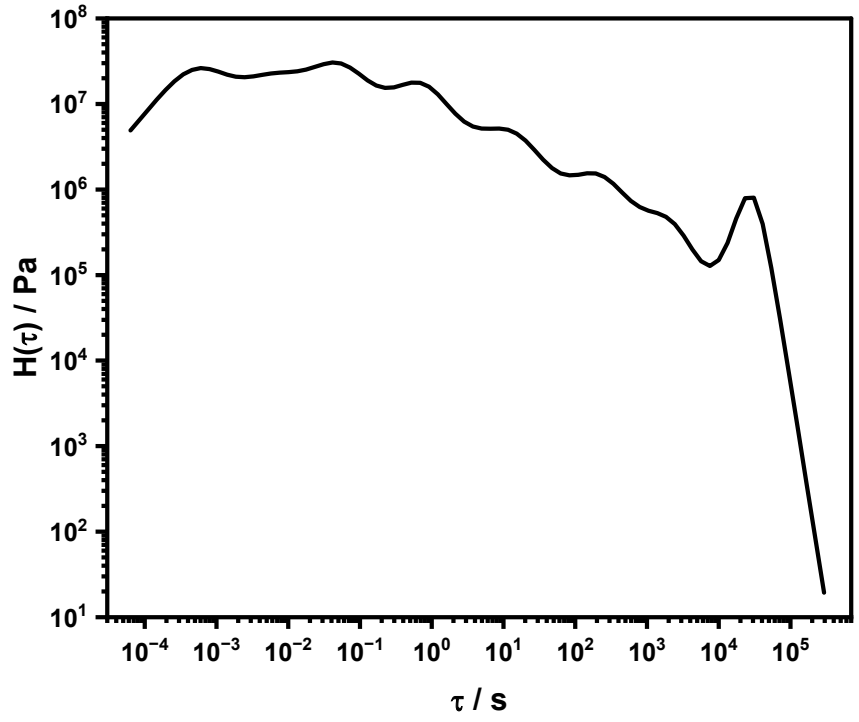

Figure S114. Computational relaxation spectrum of **P1-Zn**.

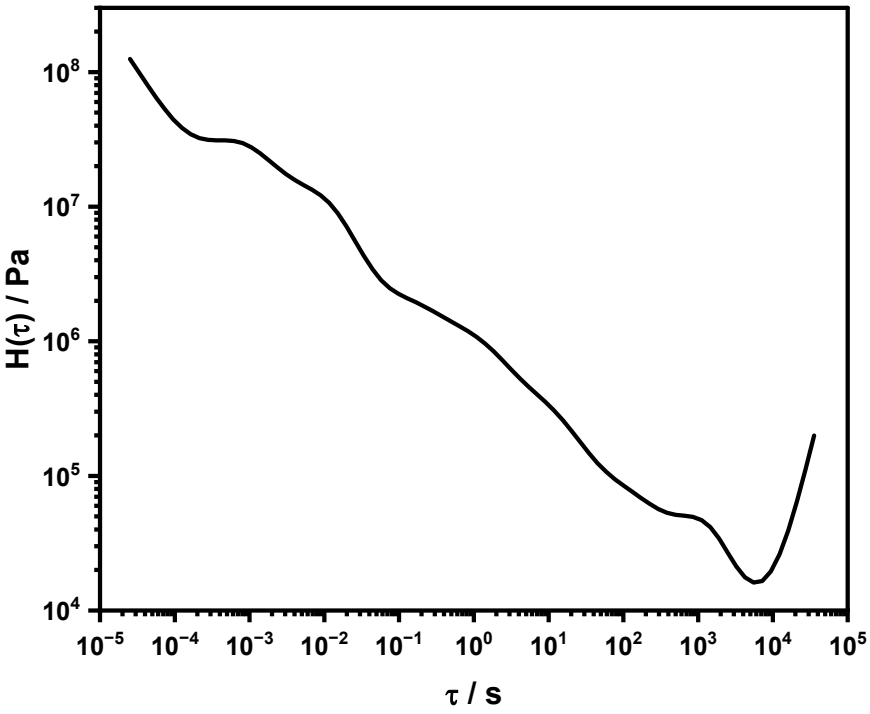

Figure S115. Computational relaxation spectrum of **P2-Fe**.

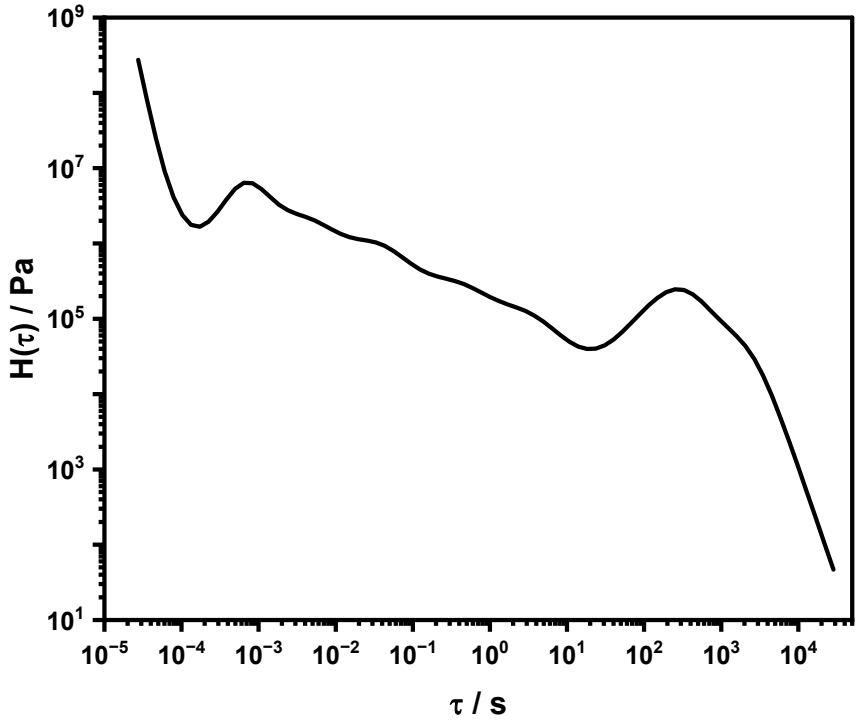

Figure S116. Computational relaxation spectrum of **P2-Zn**.

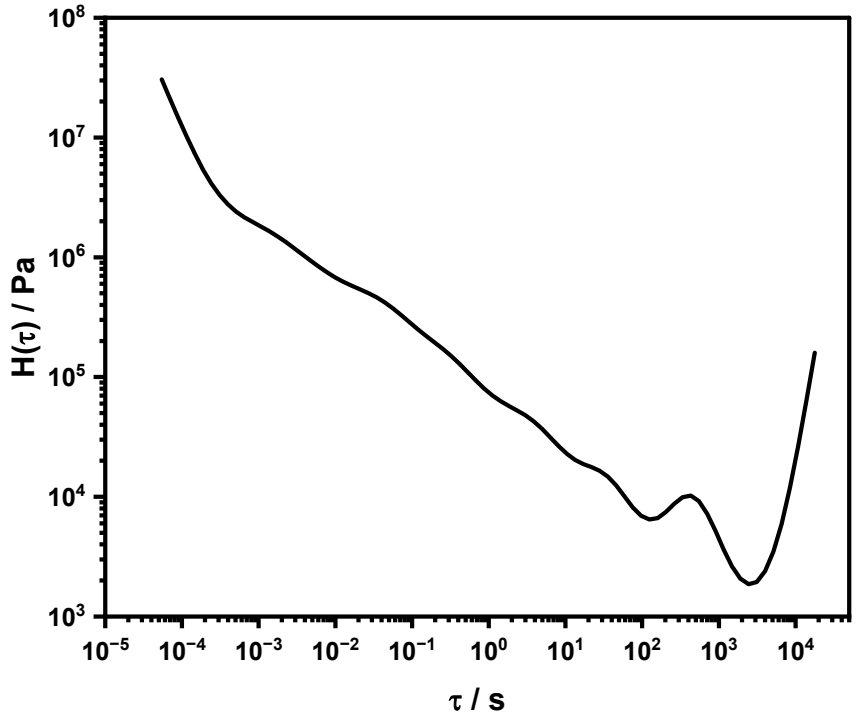

Figure S117. Computational relaxation spectrum of **P3-Fe**.

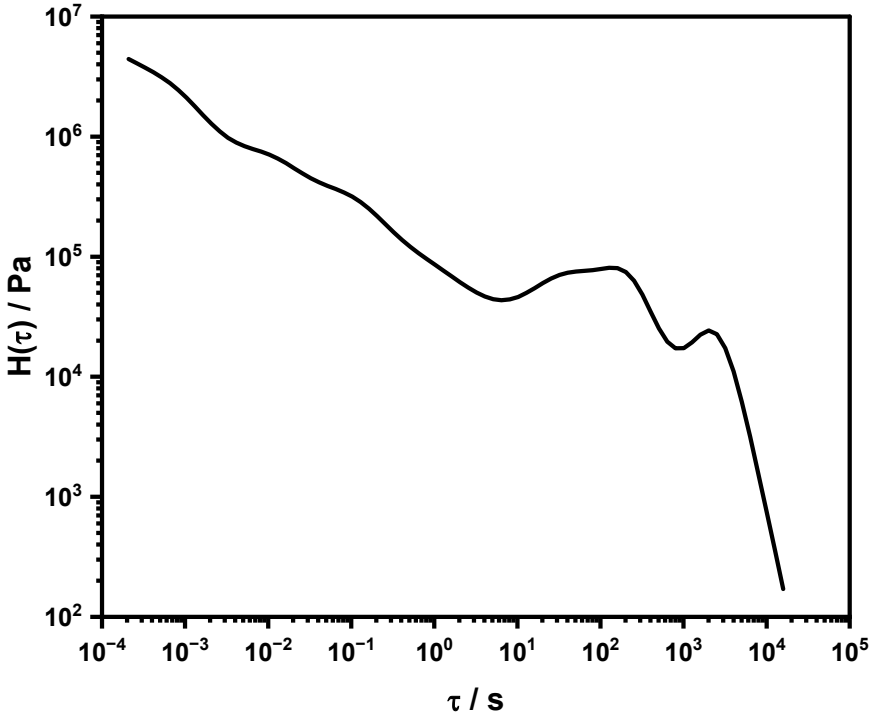

Figure S118. Computational relaxation spectrum of **P3-Zn**.

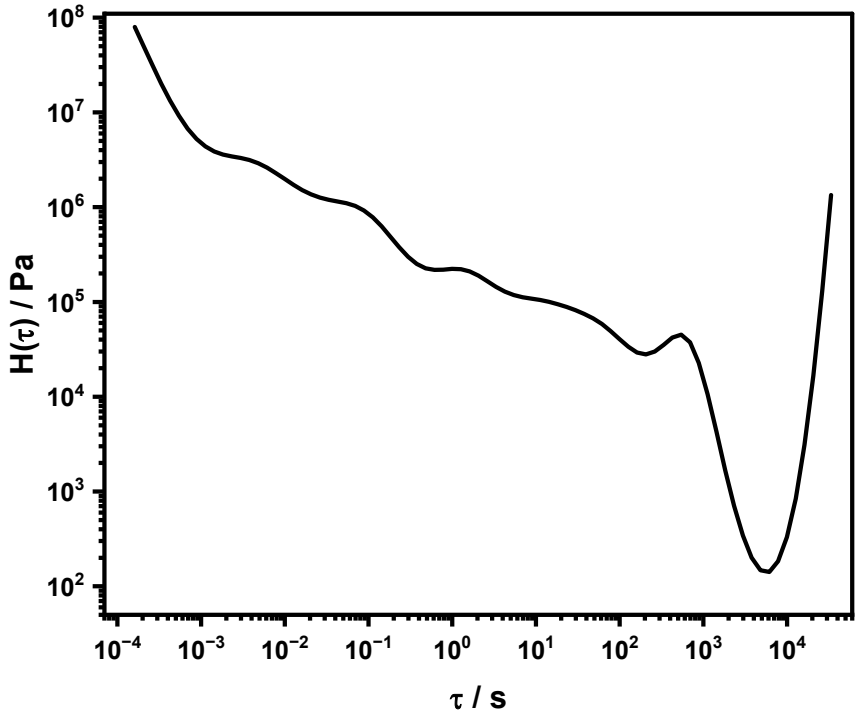

Figure S119. Computational relaxation spectrum of **P1-cc**.

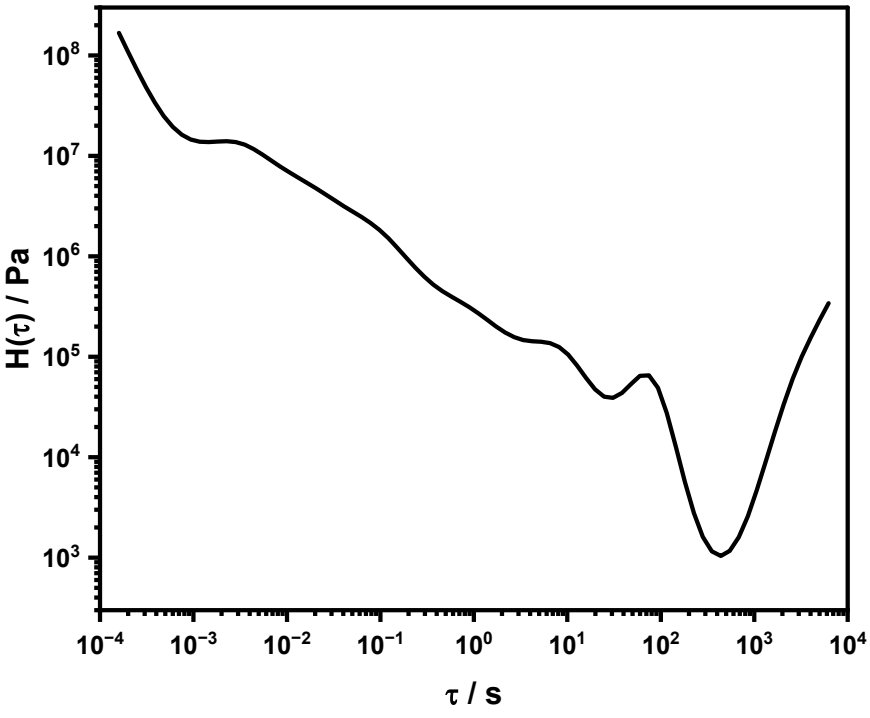

Figure S120. Computational relaxation spectrum of **P2-cc**.

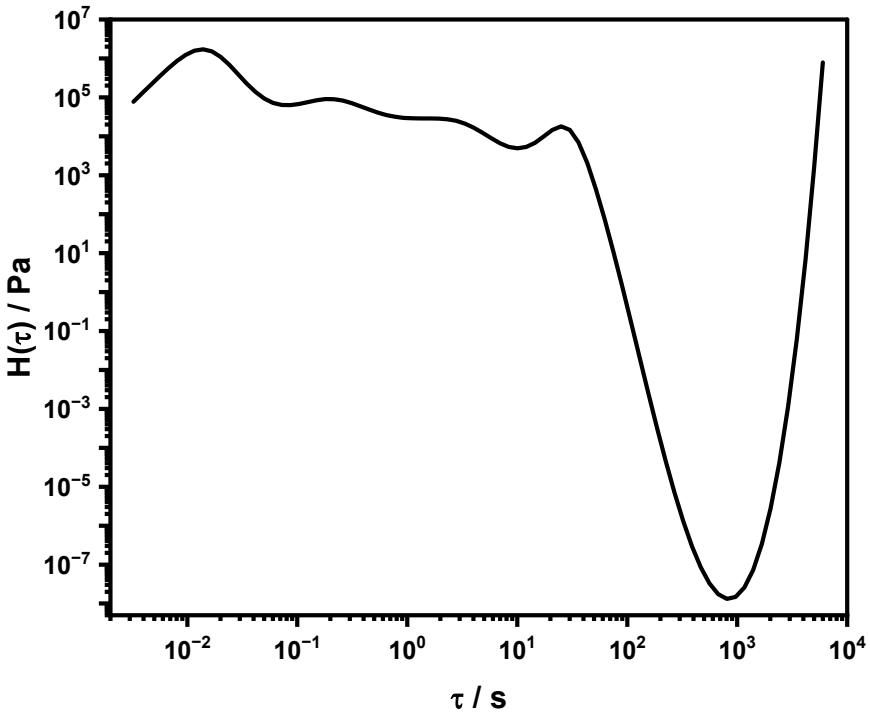

Figure S121. Computational relaxation spectrum of **P3-cc**.

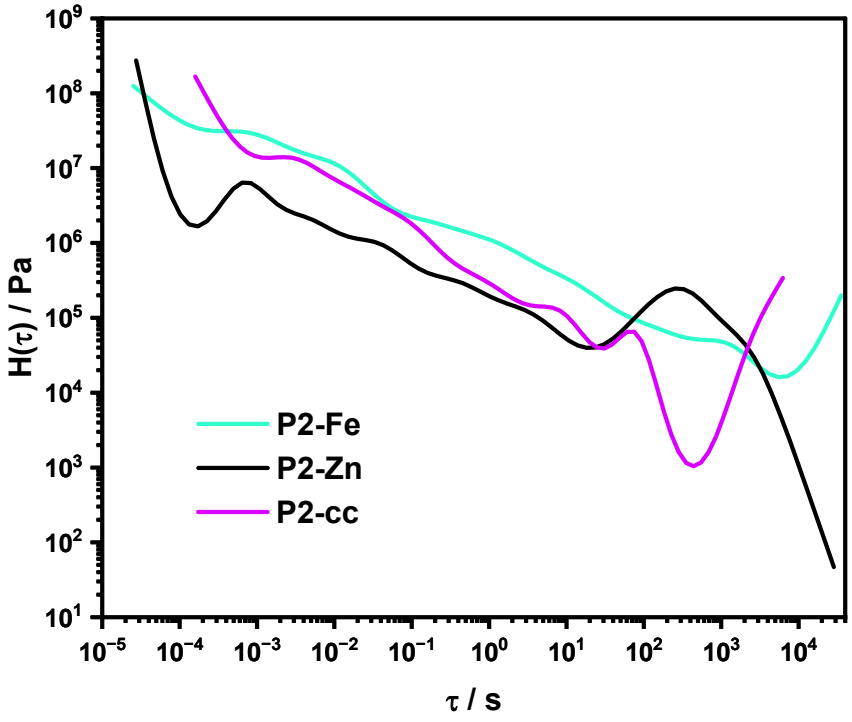

Figure S122. Computational relaxation spectra of all polymers containing BMA.

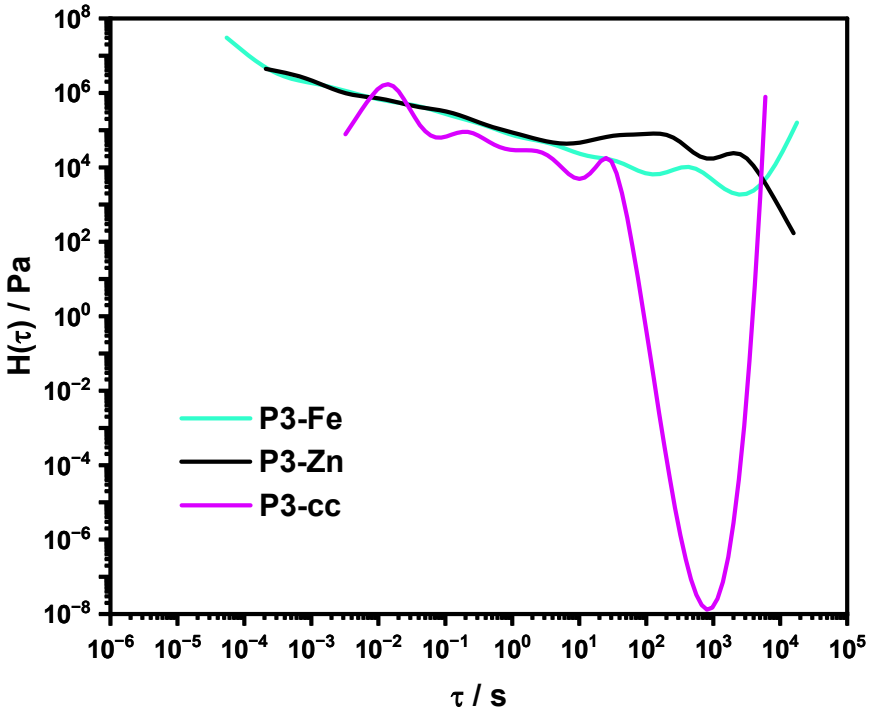

Figure S123. Computational relaxation spectra of all polymers containing EHMA.

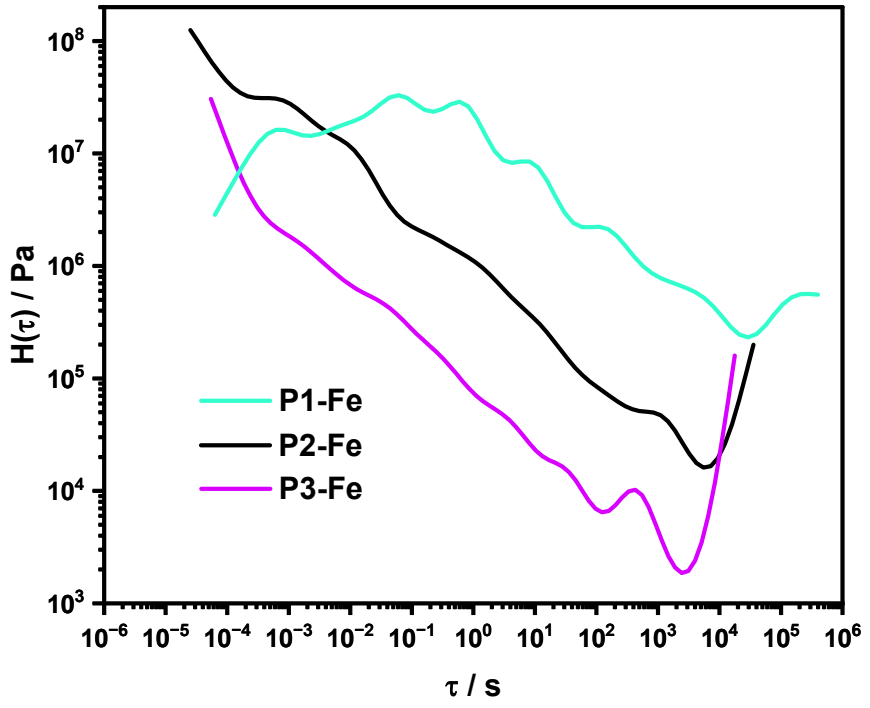

Figure S124. Computational relaxation spectra of all metallopolymers containing Fe(II).

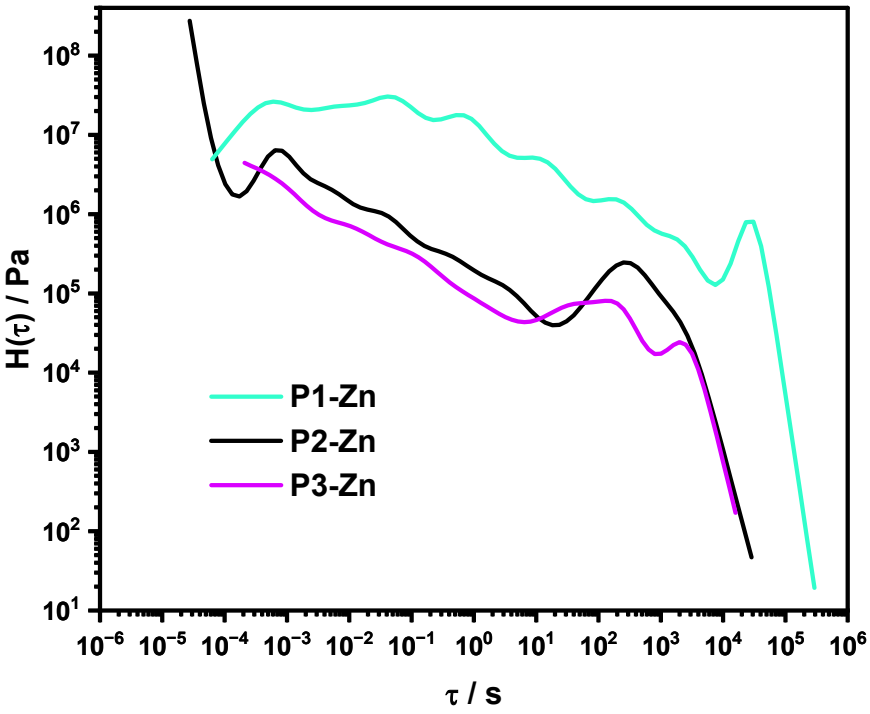

Figure S125. Computational relaxation spectra of all metallopolymers containing Zn(II).

12 Raman spectroscopy

Raman spectroscopy measurements were conducted over the spectral range of 0 to 4000 cm^{-1} with a resolution of 4 cm^{-1} using a MultiRam Fourier-transform Raman spectrometer (Bruker Corporation, Billerica, MA, USA). The 1064 nm excitation source was provided by a Nd:YAG laser (Klastech DeniCAFC-LC-3/40, Dortmund, Germany). The laser power reaching the sample plane was varied based on the photothermal stability of the samples and the number of scans per sample, aimed at enhancing the signal-to-noise ratio, are documented in **Table S11**.

For temperature dependent Raman measurement, sample heating was performed using a Linkam LTS420 stage (old model) (Linkam Scientific Instruments Ltd., Waterfield, Tadworth, Surrey) controlled by Linkam TP93 controller. The temperature was incrementally adjusted from 30 °C to 150 °C in steps of 10 °C at a heating rate of 5 °C min^{-1}. At each target temperature, the heat distribution in the sample was allowed to stabilize for 3 to 5 minutes before Raman measurements were taken. This was done to ensure consistent thermal equilibrium.

Data preprocessing was then carried out using an in-house developed Raman software called Ramanmetrix[27] and Sensitive Nonlinear Iterative Peak (SNIP) clipping algorithm with 60 iterations was used to remove any unwanted background signals. Subsequently, the spectra were confined to the 100 to 3500 cm^{-1} range. To reduce intensity variability and facilitate sample comparison, vector normalization was enough to normalize the Raman data set.

Table S11. Laser power at the sample plane for the FT-Raman measurements conducted at room temperature and at elevated temperatures, along with the number of scans performed to enhance the signal-to-noise ratio.

Samples	Room temperature		Elevated temperature	
	Laser power [mW]	Number of scans	Laser power [mW]	Number of scans at each temperature
Tpy-MA	345	250	-	-
$[(Tpy)_2Zn]^{2+}$	345	250	-	-
$[(Tpy)_2Fe]^{2+}$	20	1000	-	-
P1	345	250	-	-
P2	345	250	-	-
P3	345	500	-	-
P1-Zn	345	500	345	250
P2-Zn	345	500	345	250
P3-Zn	345	500	345	250
P1-Fe	115	1000	45	1000
P2-Fe	155	1000	83	500
P3-Fe	190	1000	83	500
PMMA	345	500	-	-
P1-cc	345	500	-	-

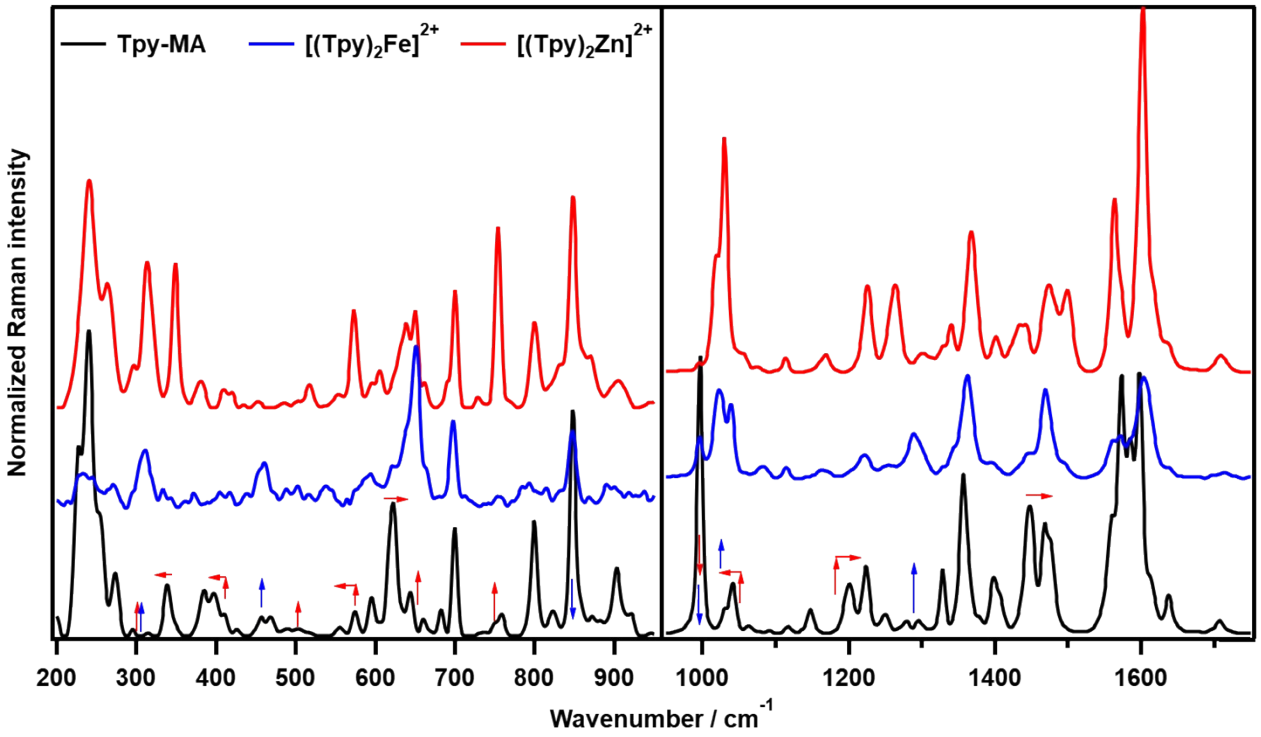

Figure S126. Normalized FT-Raman spectra (200 to 1750 cm^{-1}) of the terpyridine monomer (**Tpy-MA**, black), terpyridine-iron complex(**[(Tpy)$_2$Fe]$^{2+}$**, blue) and the terpyridine-zinc complex (**[(Tpy)$_2$Zn]$^{2+}$**, red) measured at room temperature. The arrows indicate the direction of the shifts and whether the band is decreasing or increasing in peak intensity. For clarity and ease of comparison, only the wavenumber region between 200 and 950 cm^{-1} has been zoomed in.

Table S12. FT-Raman band positions of the terpyridine monomer and the corresponding wavenumber shifts upon metal complexation.

Tpy-MA	[(Tpy)$_2$Zn]$^{2+}$	[(Tpy)$_2$Fe]$^{2+}$	Band assignments
	312.7	310.8	vs(N-Zn), central vs(N-Fe), central
339.7	349.3		
457		452	
469		461.2	
	517		
573	573		
594.3	594.3		

Tpy-MA	$[(Tpy)_2Zn]^{2+}$	$[(Tpy)_2Fe]^{2+}$	Band assignments
623.2	638.6	638.6	
644.4	650.2	650.2	
700.3	700.3	698.4	δ(C-C), in plane
	754.3		δ(C-C), in plane
847	847	846.9	
997.3	995.4	995.4	δ(C-C), scissoring
1032	1018.5	1022.4	δ(C-C), scissoring
1041.6	1030.1	1039.7	δ(C-H), in plane
1201.7	1263.4		vas(C-C), ring
1222.9	1226.8	1222	
		1288.5	
1446.6	1473.6		
1467.8	1498.7	1469.8	
1560.4	1564.2	1560.4	
1573.9		1572	v(C-C), ring
1585.5			vs(C-C), central ring
1599	1602.8	1604.7	vs(N-C), central

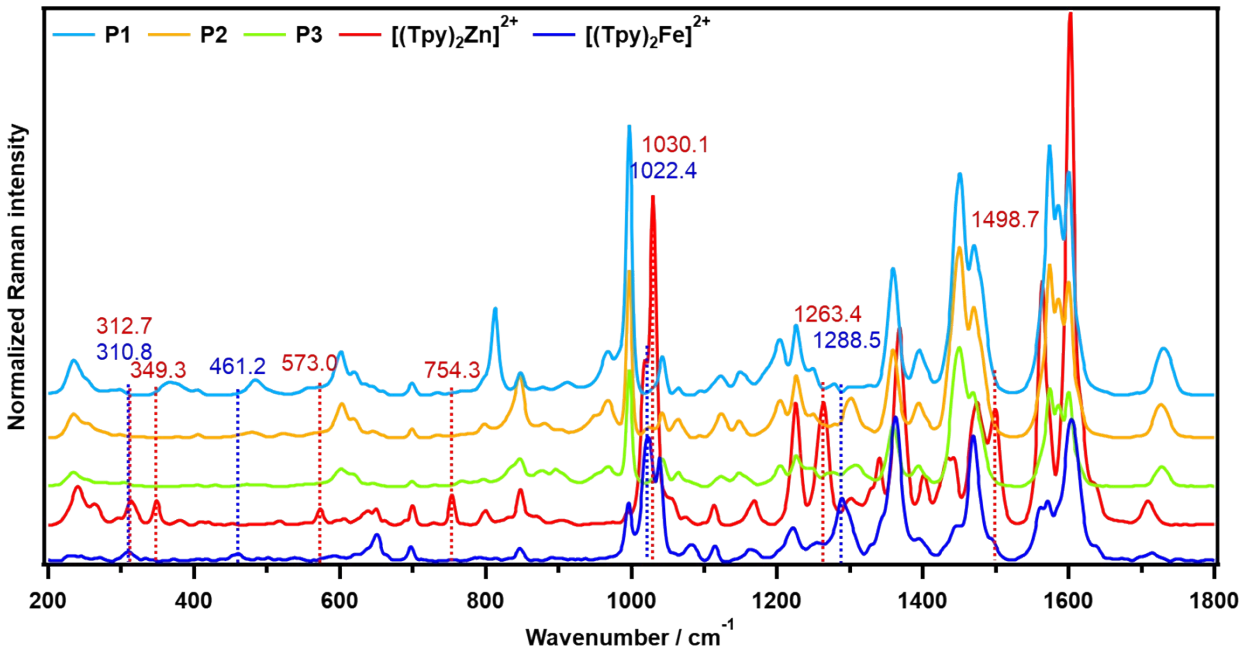

Figure S127. Normalized FT-Raman spectra of the model polymers (**P1** to **P3**) compared to the metal complexes, demonstrating that the identified characteristics bands do not interfere with the polymer matrix. All spectra are measured at room temperature.

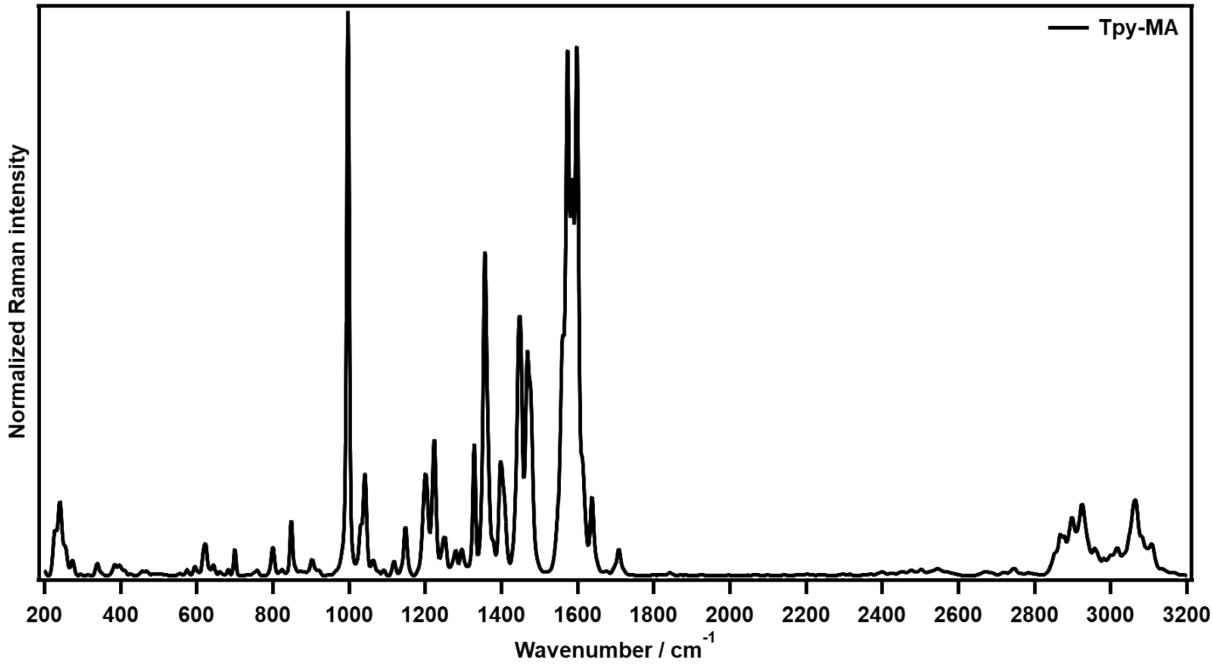

Figure S128. Normalized FT-Raman spectrum of the terpyridine monomer (**Tpy-MA**) measured at room temperature confined in the range of 200 to 3200 cm^{-1}, using a laser power of 345 mW at the sample plane.

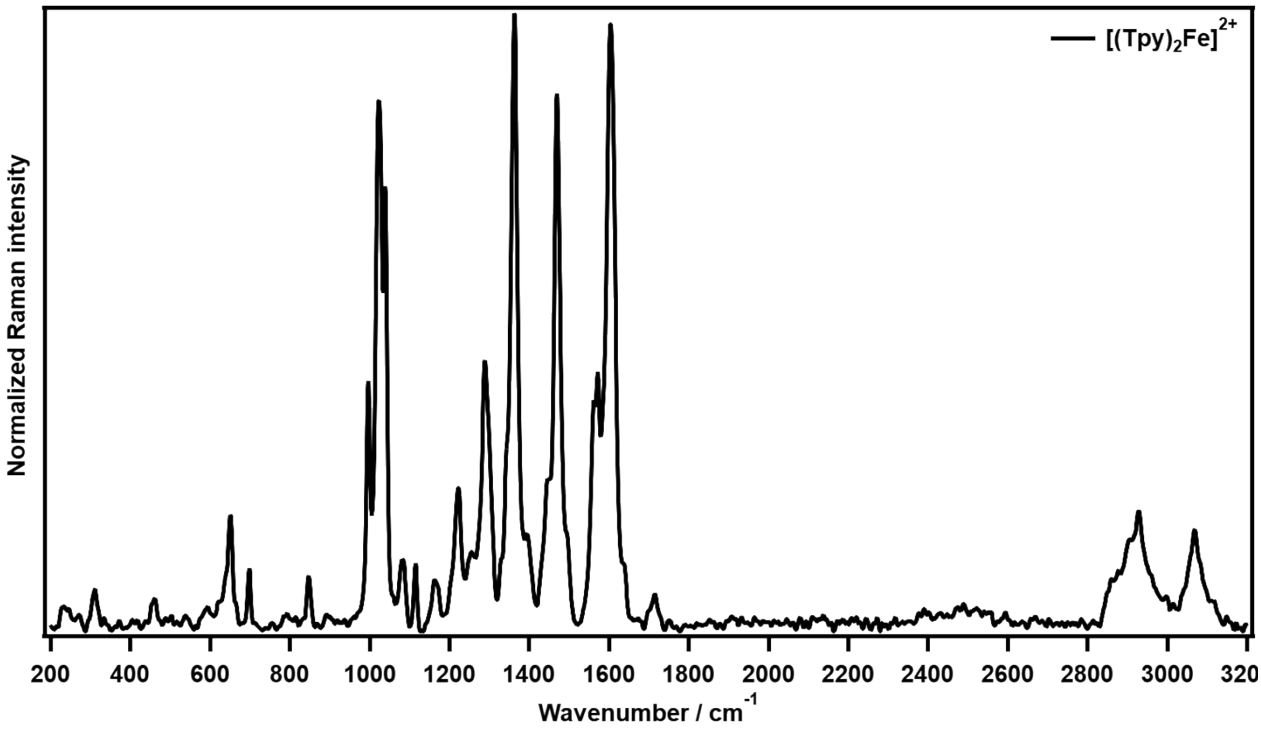

Figure S129. Normalized FT-Raman spectrum of the terpyridine-iron complex **[(Tpy)$_2$Fe]$^{2+}$** measured at room temperature confined in the range of 200 to 3200 cm^{-1}, using a laser power of 20 mW at the sample plane.

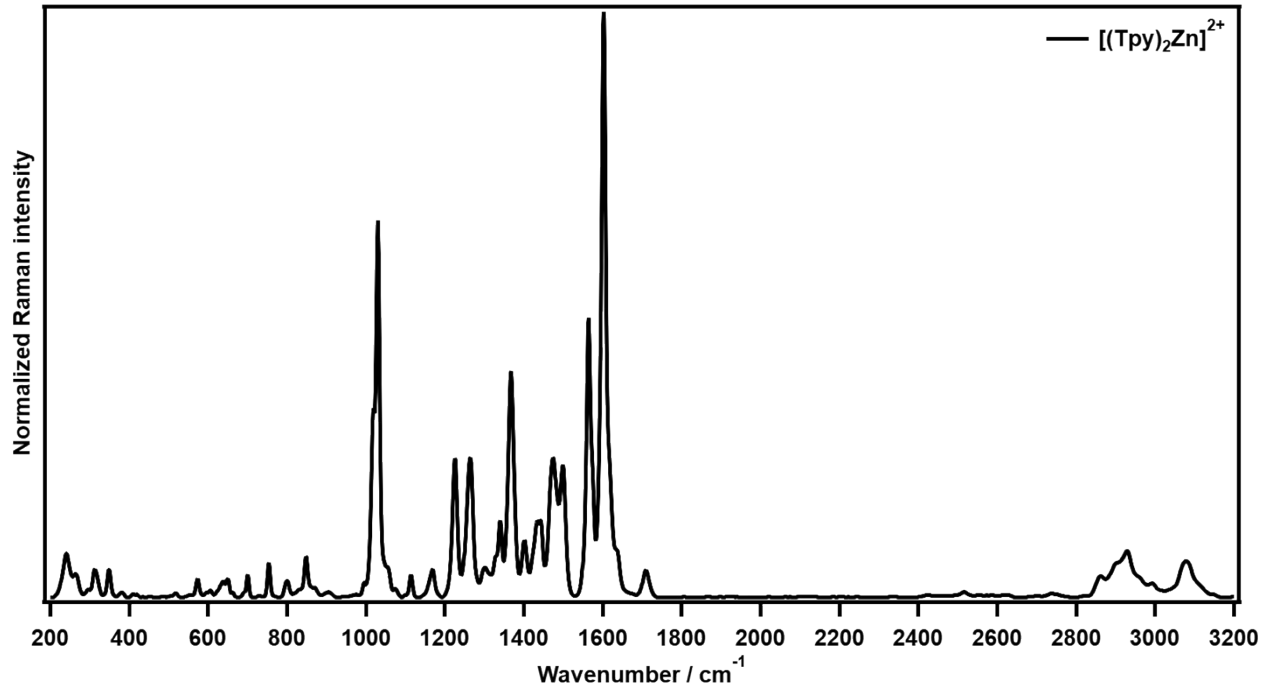

Figure S130. Normalized FT-Raman spectrum of the terpyridine-zinc complex **[(Tpy)$_2$Zn]$^{2+}$** measured at room temperature confined in the range of 200 to 3200 cm^{-1}, using a laser power of 345 mW at the sample plane.

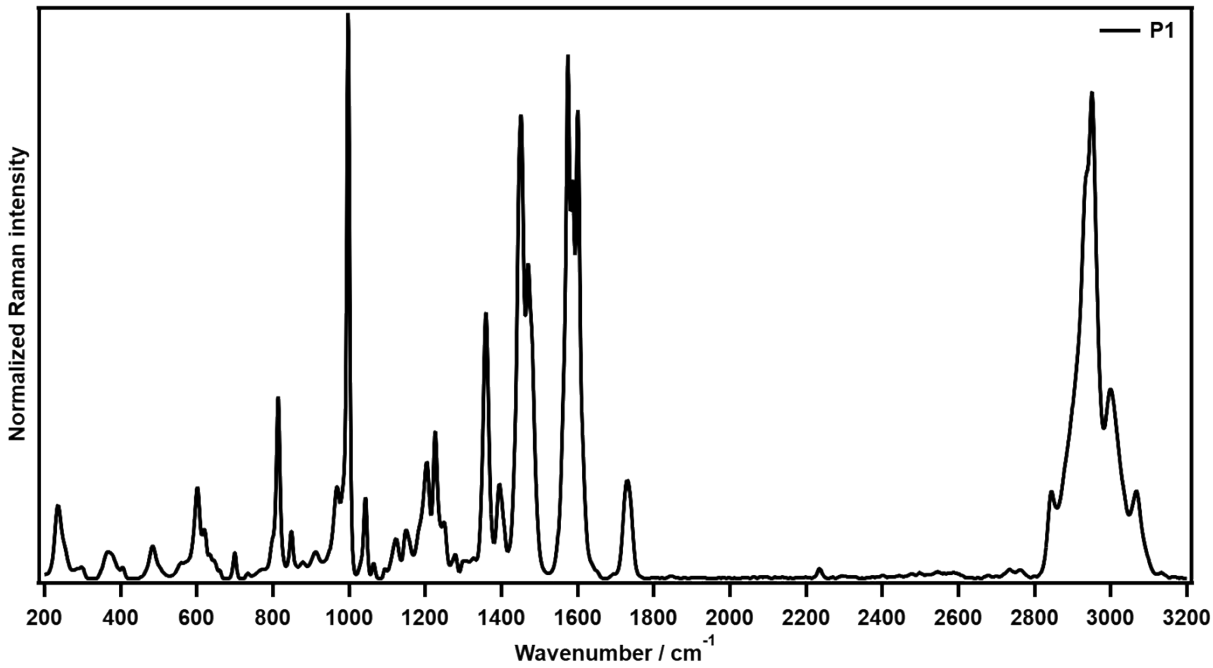

Figure S131. Normalized FT-Raman spectrum of the polymer **P1** measured at room temperature confined in the range of 200 to 3200 cm^{-1}, using a laser power of 345 mW at the sample plane.

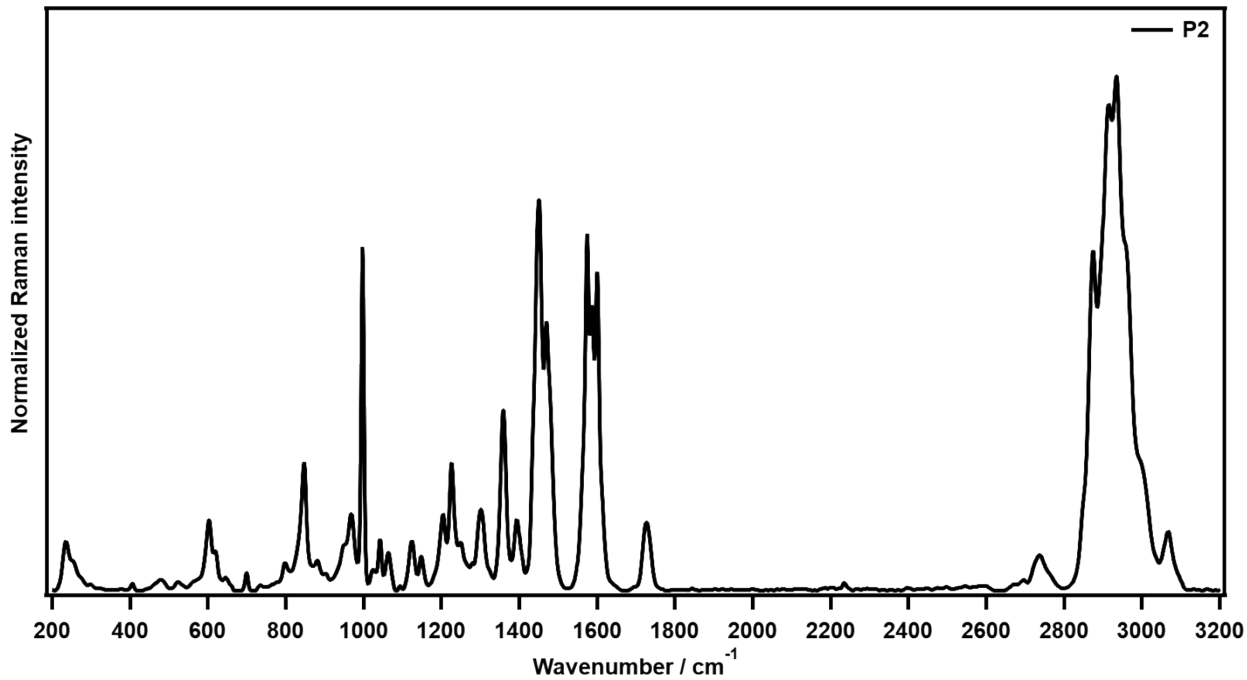

Figure S132. Normalized FT-Raman spectrum of the polymer **P2** measured at room temperature confined in the range of 200 to 3200 cm^{-1}, using a laser power of 345 mW at the sample plane.

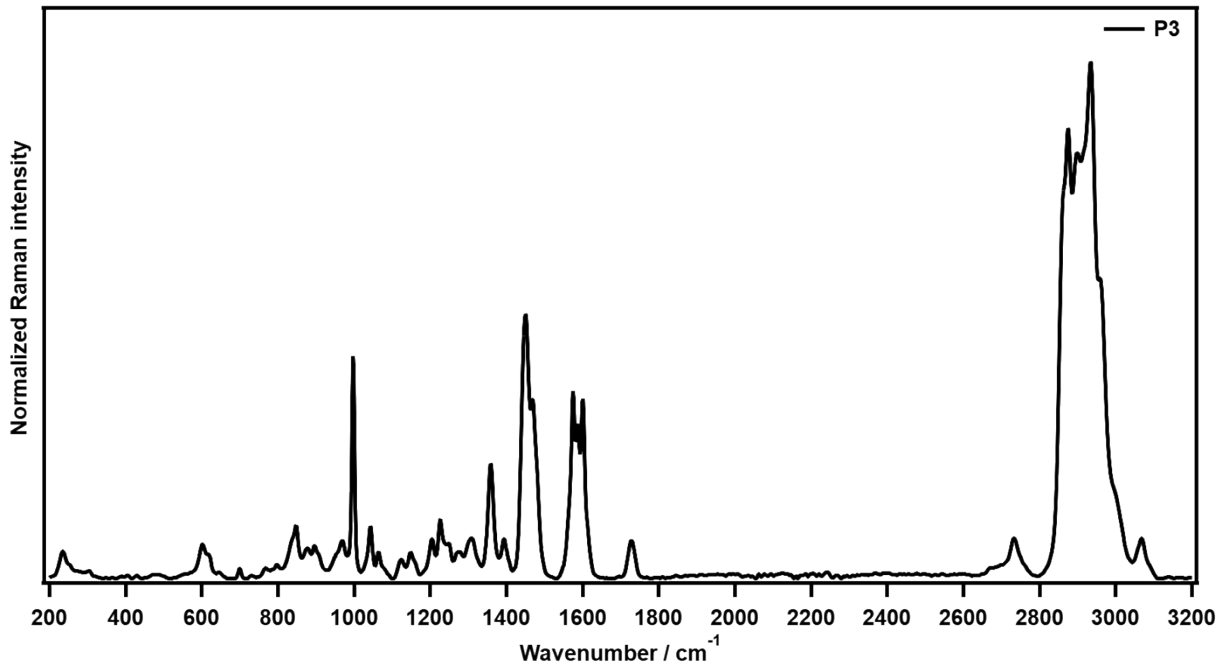

Figure S133. Normalized FT-Raman spectrum of the polymer **P3** measured at room temperature confined in the range of 200 to 3200 cm^{-1}, using a laser power of 345 mW at the sample plane.

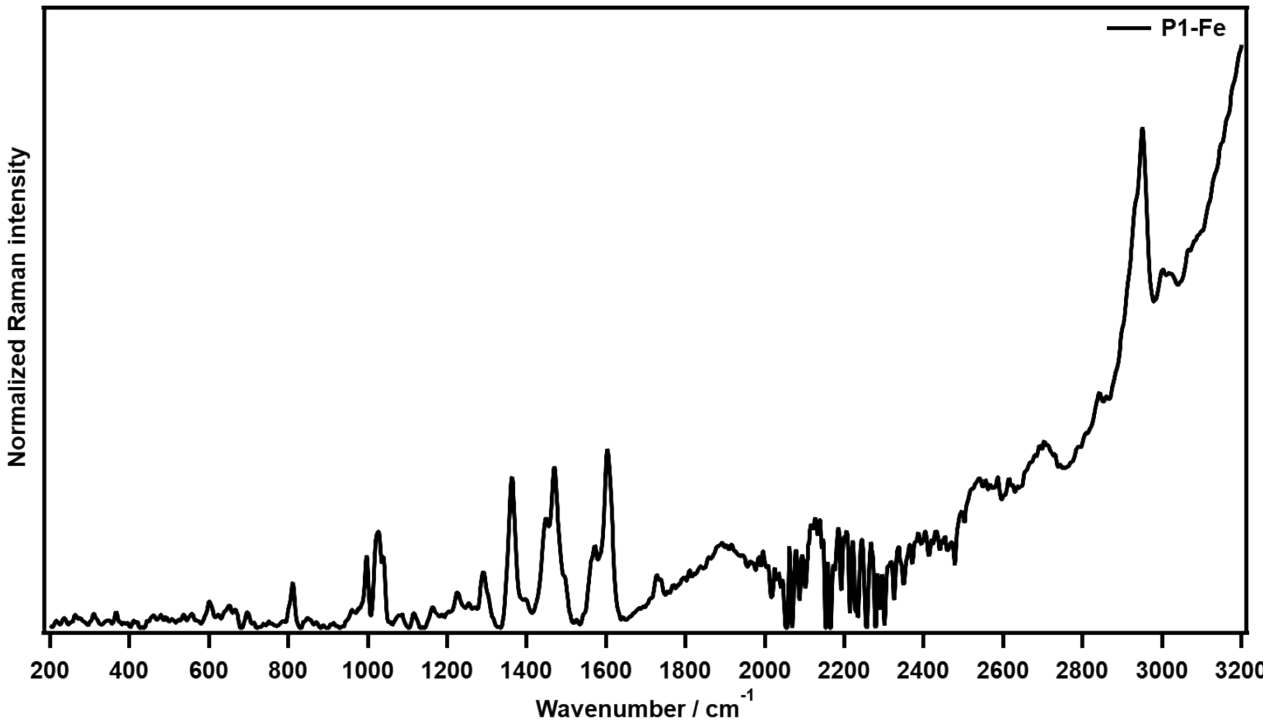

Figure S134. Normalized FT-Raman spectrum of the metallopolymer **P1-Fe** measured at room temperature confined in the range of 200 to 3200 cm^{-1}, using a laser power of 115 mW at the sample plane.

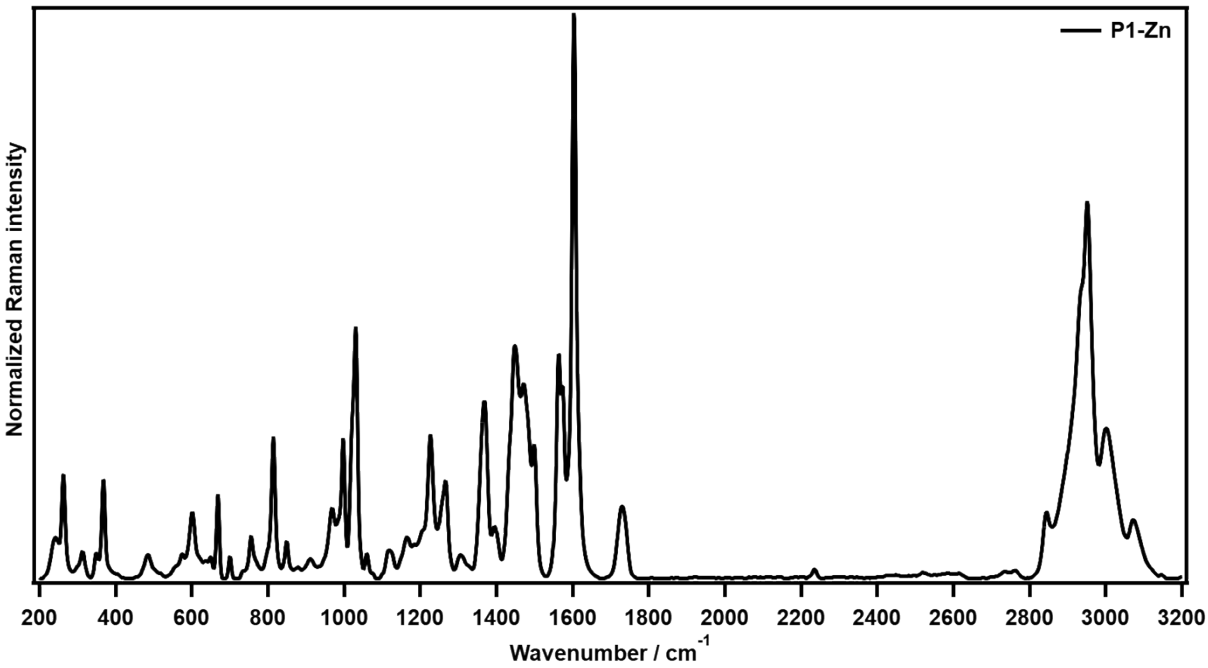

Figure S135. Normalized FT-Raman spectrum of the metallopolymer **P1-Zn** measured at room temperature confined in the range of 200 to 3200 cm^{-1}, using a laser power of 345 mW at the sample plane.

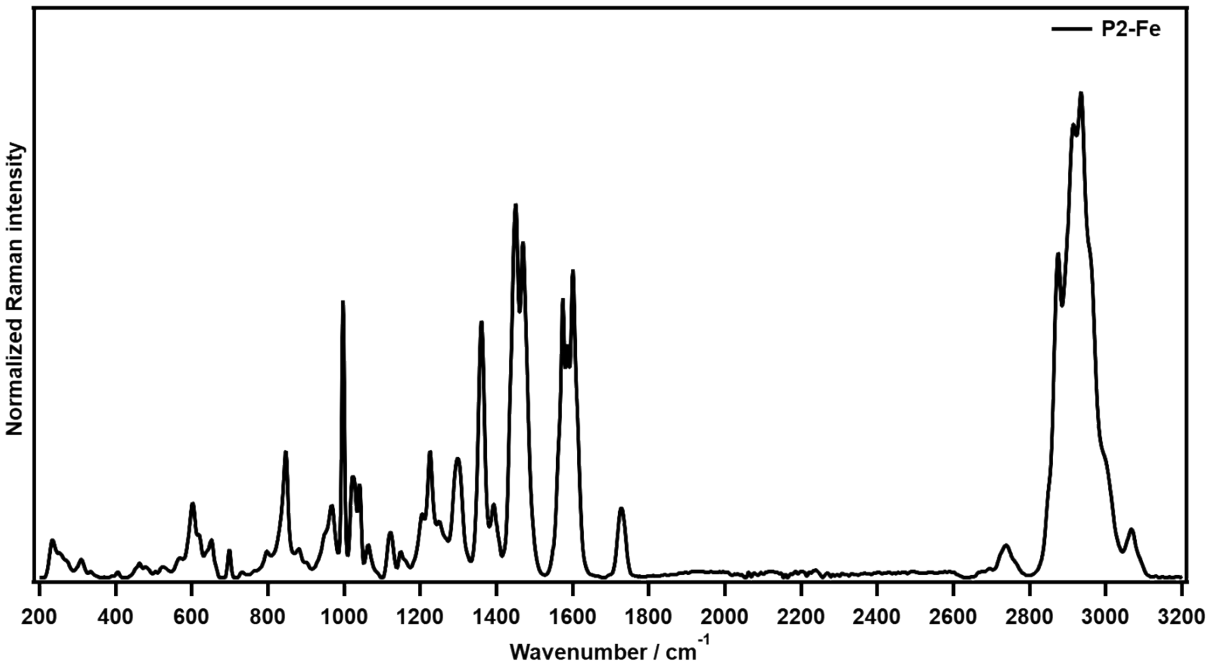

Figure S136. Normalized FT-Raman spectrum of the metallopolymer **P2-Fe** measured at room temperature confined in the range of 200 to 3200 cm^{-1}, using a laser power of 155 mW at the sample plane.

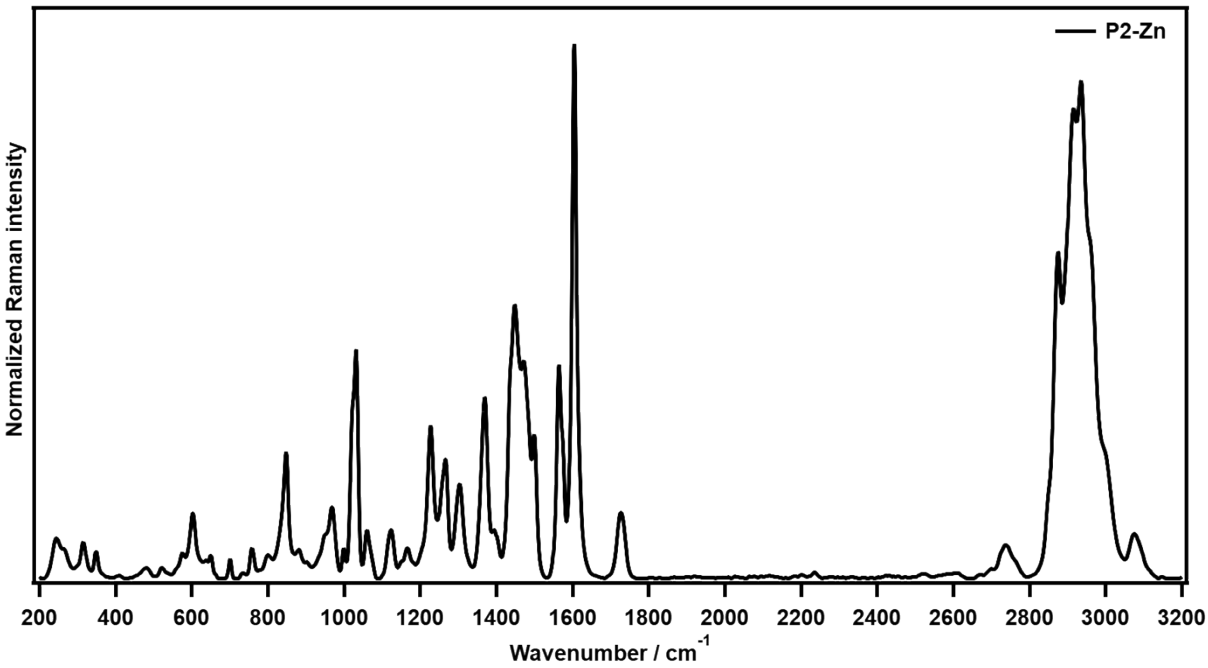

Figure S137. Normalized FT-Raman spectrum of the metallopolymer **P2-Zn** measured at room temperature confined in the range of 200 to 3200 cm^{-1}, using a laser power of 345 mW at the sample plane.

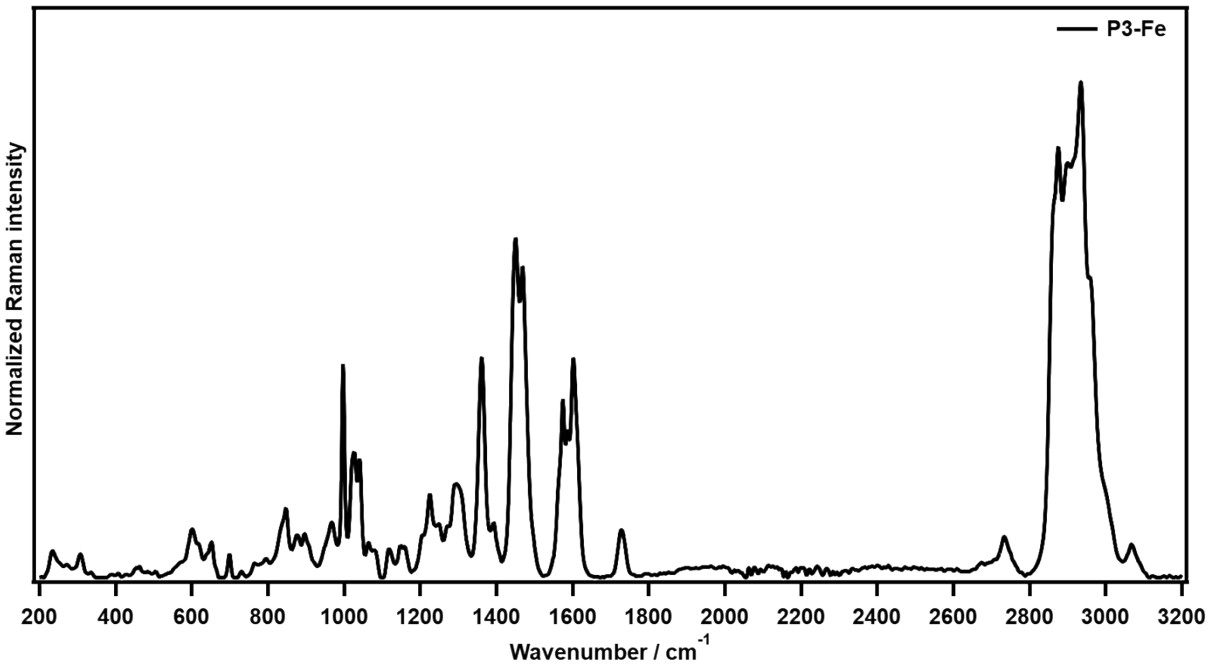

Figure S138. Normalized FT-Raman spectrum of the metallopolymer **P3-Fe** measured at room temperature confined in the range of 200 to 3200 cm^{-1}, using a laser power of 190 mW at the sample plane.

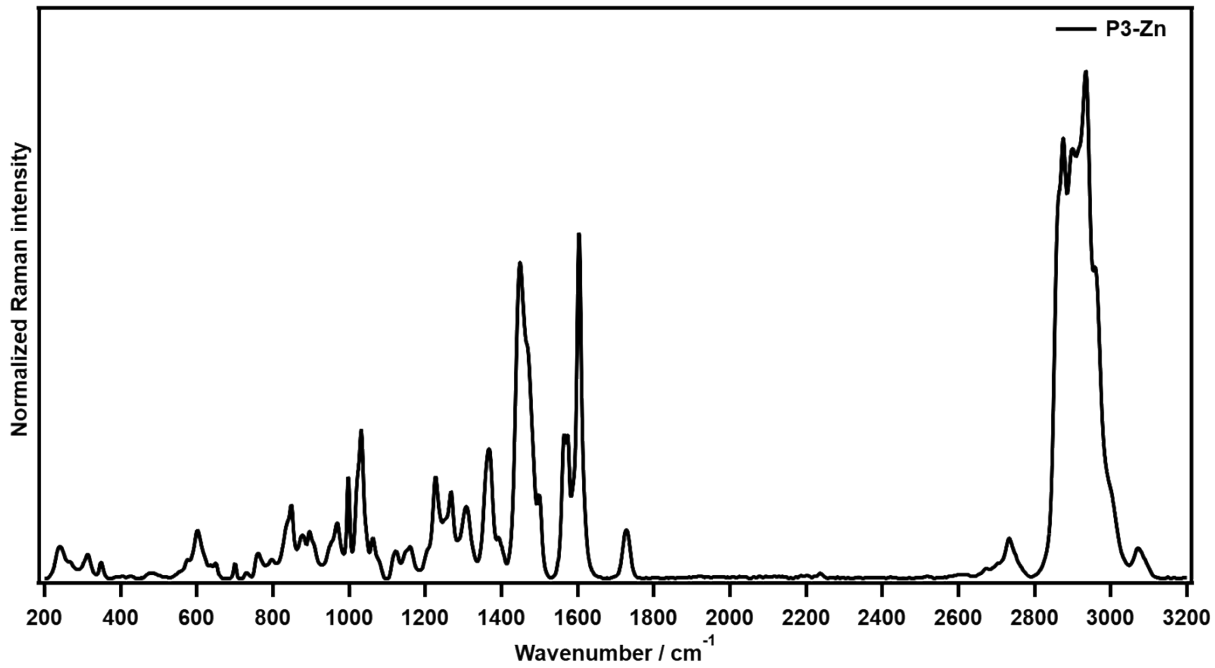

Figure S139. Normalized FT-Raman spectrum of the metallopolymer **P3-Zn** measured at room temperature confined in the range of 200 to 3200 cm^{-1}, using a laser power of 345 mW at the sample plane.

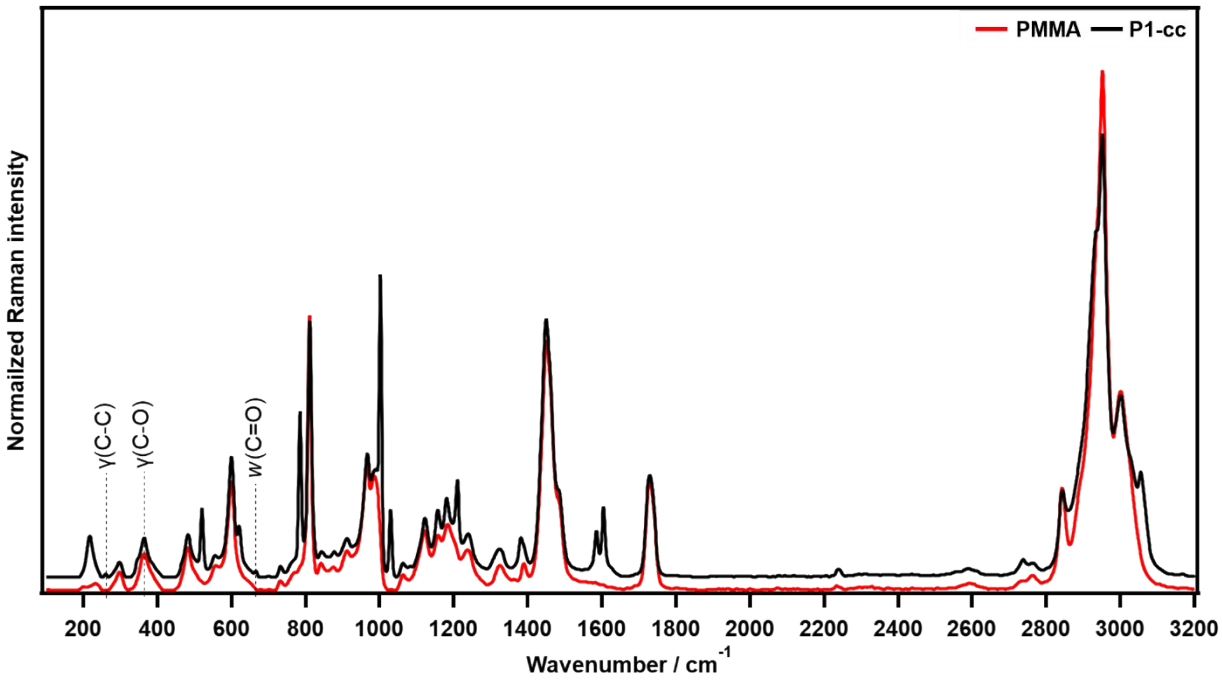

Figure S140. Normalized FT-Raman spectra of **PMMA** and **P1-cc** measured at room temperature confined in the range of 200 to 3200 cm^{-1}, using a laser power of 345 mW at the sample plane. Insert is the zoom region to highlight the weak C-C, C=O, and C-O signals.

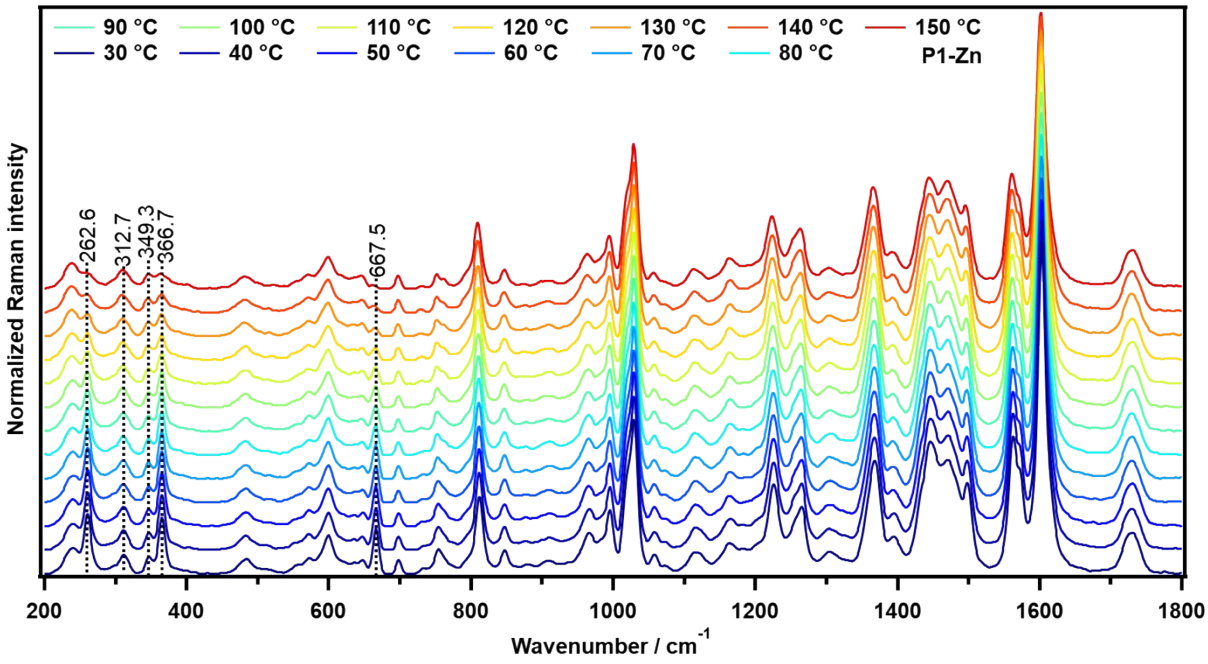

Figure S141. Normalized, temperature-dependent FT-Raman spectra of **P1-Zn**, presented in the range of 200 to 1800 cm^{-1}. The measurements were conducted using a laser power of 345 mW at the sample plane, across a temperature range of 30 to 150 °C. Preprocessing included baseline correction was performed using the Snip algorithm with 60 iterations.

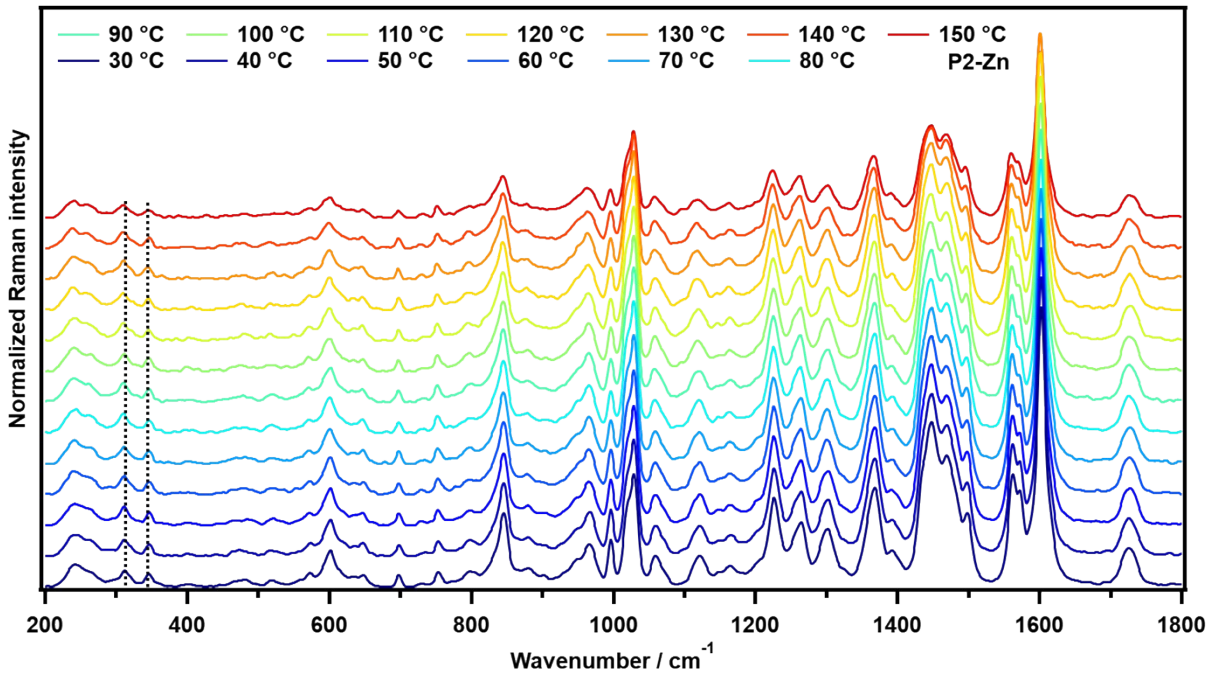

Figure S142. Normalized, temperature-dependent FT-Raman spectra of **P2-Zn**, presented in the range of 200 to 1800 cm^{-1}. The measurements were conducted using a laser power of 345 mW at the sample plane, across a temperature range of 30 to 150 °C. Preprocessing included baseline correction using the Snip algorithm with 60 iterations.

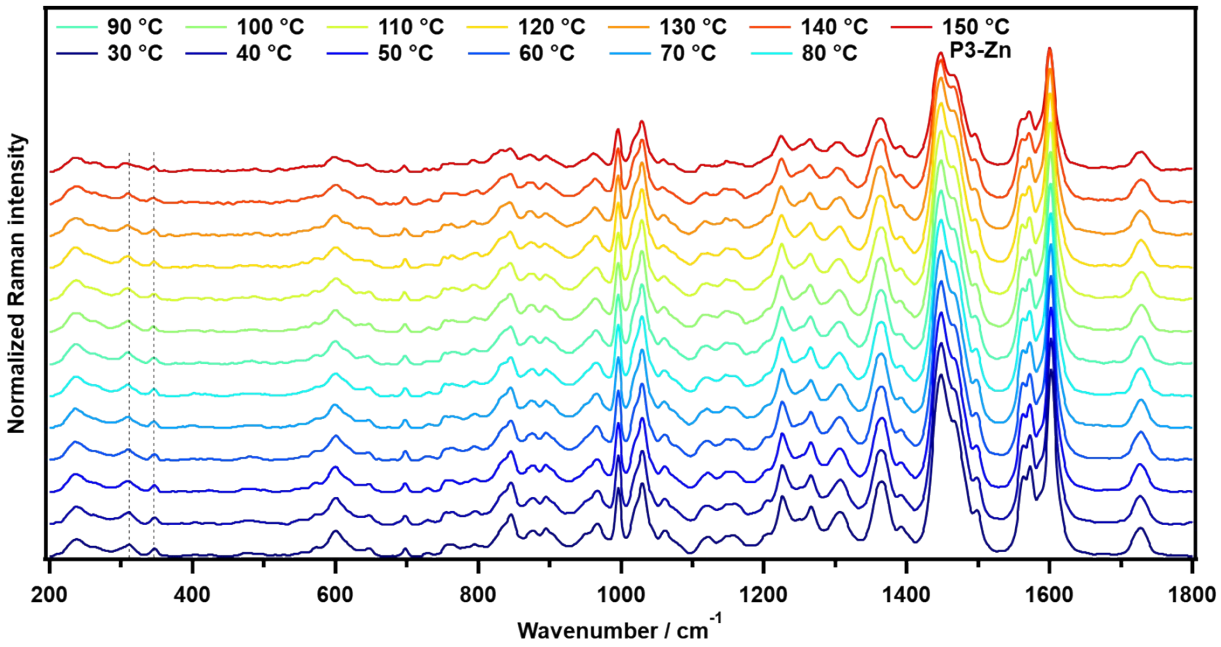

Figure S143. Normalized, temperature-dependent FT-Raman spectra of **P3-Zn**, presented in the range of 200 to 1800 cm^{-1}. The measurements were conducted using a laser power of 345 mW at the sample plane, across a temperature range of 30 to 150 °C. Preprocessing included baseline correction using the Snip algorithm with 60 iterations.

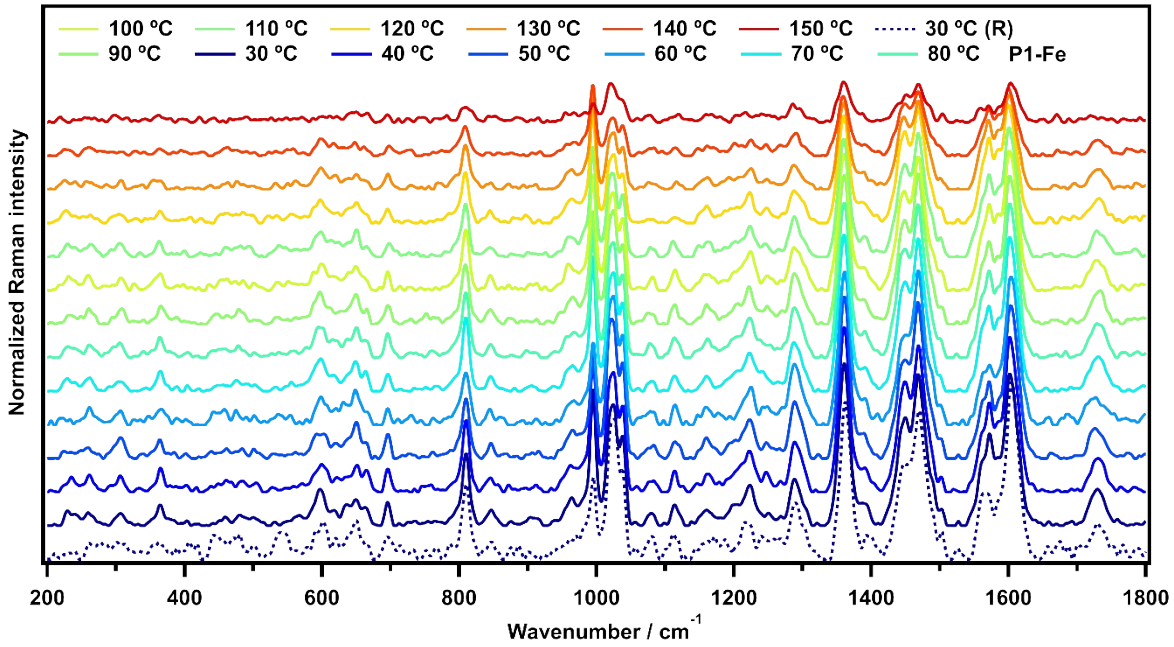

Figure S144. Normalized, temperature-dependent FT-Raman spectra of a pressed sample of **P1-Fe**, presented in the range of 200 to 1800 cm^{-1}. The measurements were conducted using a laser power of 45 mW at the sample plane, across a temperature range of 30 to 150 °C and at 30 °C after cooling. Preprocessing included baseline correction using the Snip algorithm with 80 iterations.

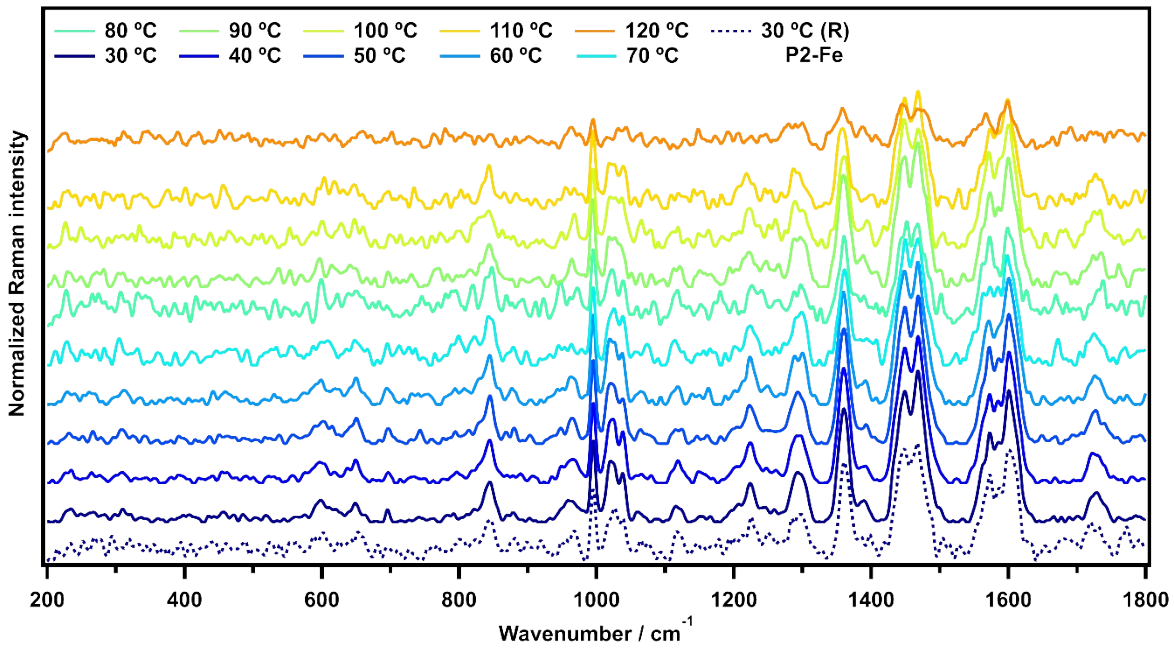

Figure S145. Normalized, temperature-dependent FT-Raman spectra of **P2-Fe**, presented in the range of 200 to 1800 cm^{-1}. The measurements were conducted using a laser power of 80 mW at the sample plane, across a temperature range of 30 to 120 °C and at 30 °C after cooling. Preprocessing included baseline correction using the Snip algorithm with 40 iterations.

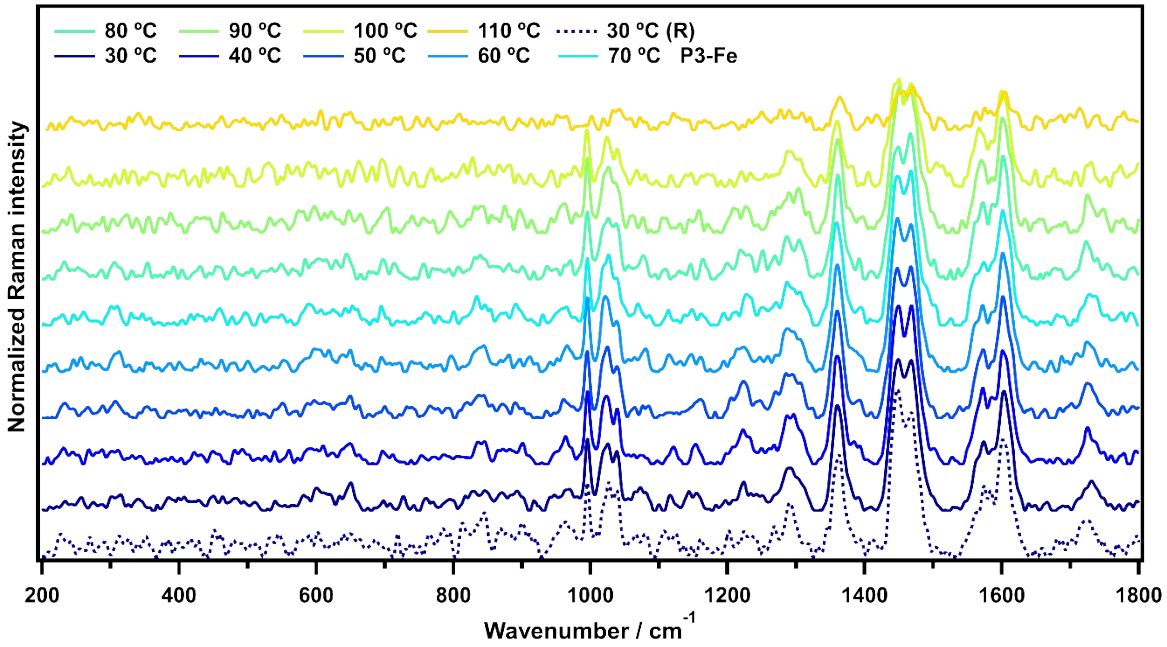

Figure S146. Normalized, temperature-dependent FT-Raman spectra of **P3-Fe**, presented in the range of 200 to 1800 cm^{-1}. The measurements were conducted using a laser power of 80 mW at the sample plane, across a temperature range of 30 to 110 °C and at 30 °C after cooling. Preprocessing included baseline correction using the Snip algorithm with 40 iterations.

13 DFT calculations

Density functional theory calculations have been performed for the terpyridine molecule, as well as the zinc(II) and iron(II) terpyridine complexes.

All calculations have been performed with ORCA 5,[28] using the B3LYP hybrid exchange-correlation functional with the def2-SVP Karlsruhe basis set, combined with the D4 dispersion correction and the geometrical counter poise-correction.

Geometry optimizations for all molecules in the gas phase have been carried out utilizing the external optimizer *pysisyphus*.[29] All eigenvalues of the Hessians are positive, indicating stable minima. Initial geometries use the lowest-energy conformers obtained with CREST[30] using xTB[31] at the GFN2 level of theory.

The modeled Raman spectra have been scaled by a factor of 0.9671[32] to account for anharmonicity effects. The calculated stick spectra have been broadened with a Voigt function using a full width at half maximum of 10 cm^{-1}.

To calculate the free Gibbs energies and association constants, additional geometry optimizations were performed using the C-PCM implicit-solvent model with methanol as the solvent. The investigated reaction (with M being Fe or Zn) reads

$$\left[M(CH_4O)_6\right]^{2+} + 2Tpy \rightarrow \left[M(Tpy)_2\right]^{2+} + 6CH_4O$$

Following the thermodynamic cycle,[33] the complexation free energy G can be calculated as

$$G = \Delta G_g^0 + \Delta\Delta G_{solv}^0 + (6-1)\Delta G^{0\rightarrow *} + 6RTln([CH_4O])$$

with $^{\Delta G_g^0}$ being the complexation free energy in gas phase and $^{\Delta\Delta G_{solv}^0}$ being the changes in solvation free energies. $^{\Delta G^{0\rightarrow *}}$ is the change in free energy when transferring an ideal gas (1 atm) to solution (1 M) at 303 K and is given with 1.943 kcal/mol. $^{RTln([CH_4O])}$ is the change in free energy when transferring 1 mol of methanol from the solvent phase to pure methanol (24.72 M) and is given as 1.943 kcal/mol at 303 K.

Table S13. Summary of the calculated free Gibbs energy (G) and association constants (K) of the bis-terpyridine metal complexes using two chloride-anions to mimic the electrostatic effect of the counter ions.

Complex	G_{calc}	$\ln K_{calc}$
$[(Tpy)_2Fe]^{2+}$	-157.647	62.576
$[(Tpy)_2Zn]^{2+}$	-20.539	8.153

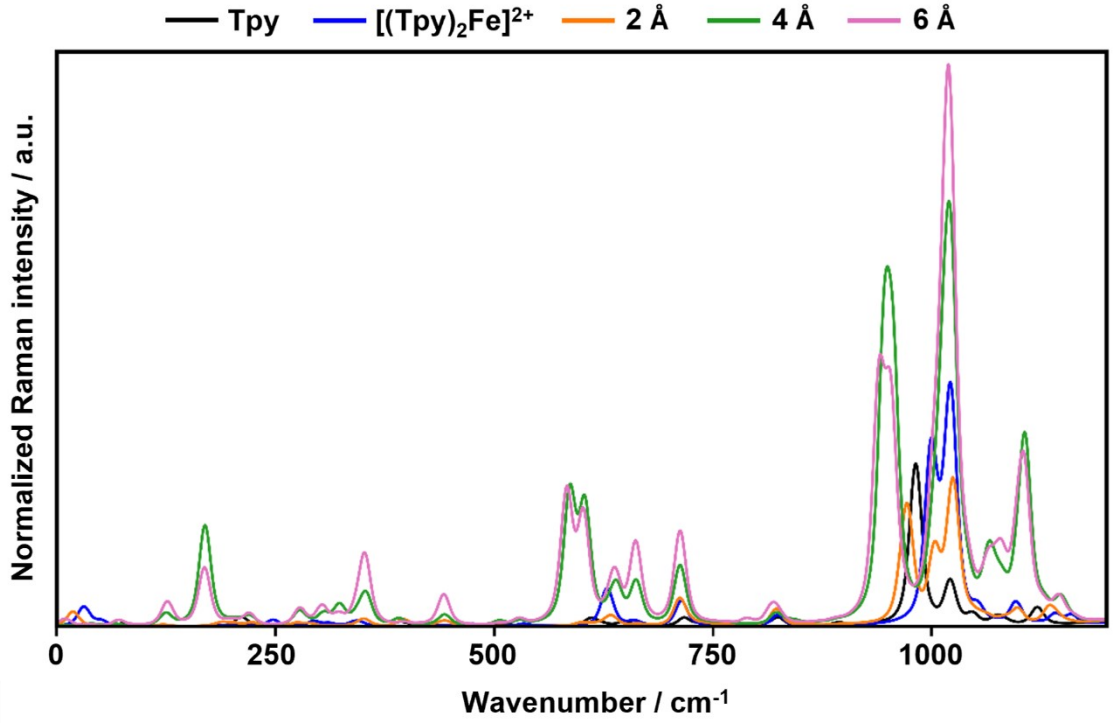

Figure S147. DFT modeled Raman spectra of the terpyridine ligand, the *bis*-terpyridine iron complex and different distances of the ligand to the metal ion.

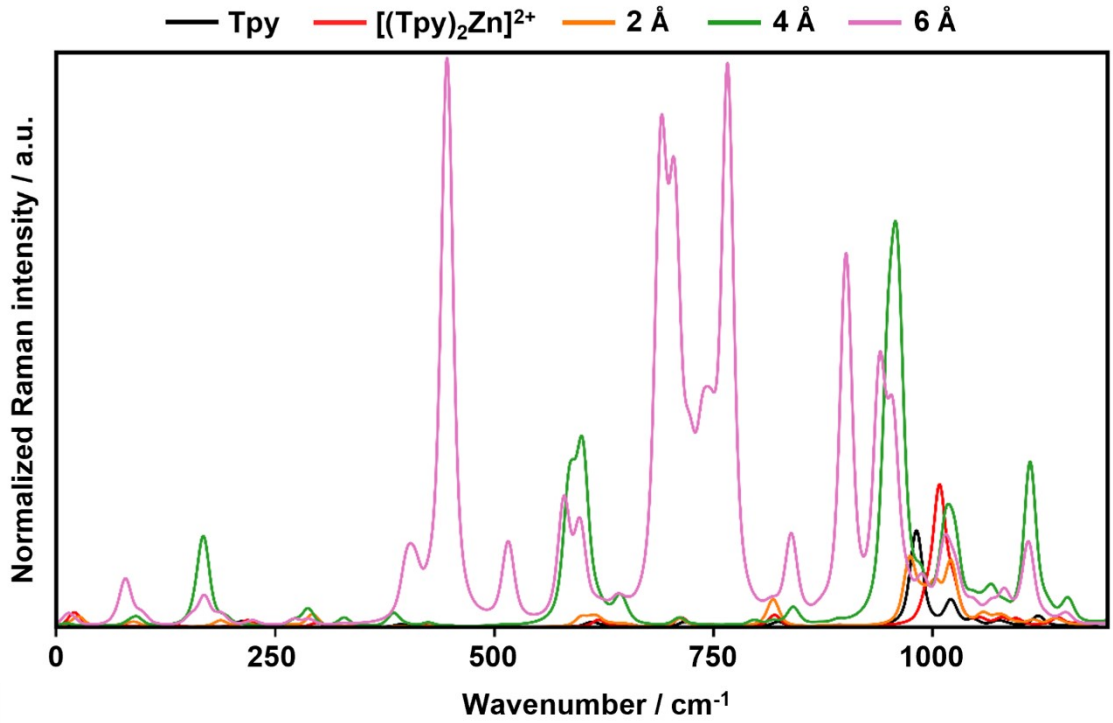

Figure S148. DFT modeled Raman spectrum of the free terpyridine ligand, the *bis*-terpyridine zinc complex and different distances of the ligand to the metal ion.

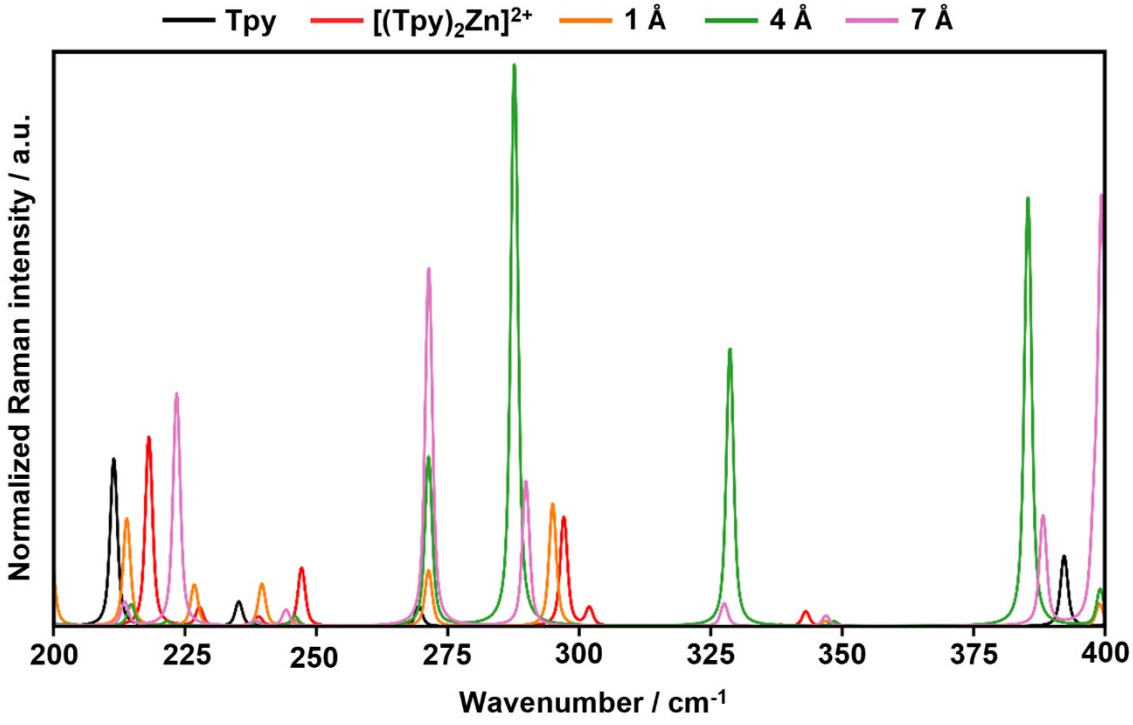

Figure S149. Zoomed in DFT modeled Raman spectrum of the free terpyridine ligand, the *bis*-terpyridine zinc complex and different distances of the ligand to the metal ion.

Table S14. Summary of the experimentally determined band positions by FT-Raman and by DFT calculations of the terpyridine monomer and the corresponding wavenumber shifts upon metal complexation.

Vibration	Raman	DFT
v(N-Zn)	313	301
v(Fe-N)	310	311
v(N-Fe)	461	475

14 References

1 S. Bode, L. Zedler, F. H. Schacher, B. Dietzek, M. Schmitt, J. Popp, M. D. Hager and U. S. Schubert, *Adv. Mater.*, 2013, **25**, 1634–1638.

2 J. Meurer, T. Bätz, J. Hniopek, C. Bernt, S. Zechel, M. Schmitt, J. Popp, M. D. Hager and U. S. Schubert, *J. Mater. Chem. A*, 2022, **10**, 25106–25117.

3 J. Meurer, T. Bätz, J. Hniopek, S. Zechel, M. Schmitt, J. Popp, M. D. Hager and U. S. Schubert, *J. Mater. Chem. A*, 2021, **9**, 15051–15058.

4 J. Meurer, J. Hniopek, T. Bätz, S. Zechel, M. Enke, J. Vitz, M. Schmitt, J. Popp, M. D. Hager and U. S. Schubert, *Adv. Mater.*, 2021, **33**, 2006655.

5 J. Dahlke, J. Kimmig, M. Abend, S. Zechel, J. Vitz, U. S. Schubert and M. D. Hager, *NPG Asia Mater.*, 2020, **12**, 13.

6 M. Enke, S. Bode, J. Vitz, F. H. Schacher, M. J. Harrington, M. D. Hager and U. S. Schubert, *Polymer*, 2015, **69**, 274–282.

7 S. Bode, R. K. Bose, S. Matthes, M. Ehrhardt, A. Seifert, F. H. Schacher, R. M. Paulus, S. Stumpf, B. Sandmann, J. Vitz, A. Winter, S. Hoeppener, S. J. Garcia, S. Spange, S. van der Zwaag, M. D. Hager and U. S. Schubert, *Polym. Chem.*, 2013, **4**, 4966–4973.

8 D. Berne, S. Laviéville, E. Leclerc, S. Caillol, V. Ladmiral and C. Bakkali-Hassani, *ACS Polym. Au*, 2025, **5**, 214–240.

9 L. E. Porath and C. M. Evans, *Macromolecules*, 2021, **54**, 4782–4791.

10 N. Rabiei, S. H. Amirshahi and M. Haghighat Kish, *Phys. Rev. E*, 2019, **99**, 032502.

11 R. G. Ricarte and S. Shanbhag, *Polym. Chem.*, 2024, **15**, 815–846.

12 Yu. S. Urzhumtsev, *Polym. Mech.*, 1975, **11**, 57–72.

13 M. L. Williams, R. F. Landel and J. D. Ferry, *J. Am. Chem. Soc.*, 1955, **77**, 3701–3707.

14 P. Virtanen, R. Gommers, T. E. Oliphant, M. Haberland, T. Reddy, D. Cournapeau, E. Burovski, P. Peterson, W. Weckesser, J. Bright, S. J. van der Walt, M. Brett, J. Wilson, K. J. Millman, N. Mayorov, A. R. J. Nelson, E. Jones, R. Kern, E. Larson, C. J. Carey, İ. Polat, Y. Feng, E. W. Moore, J. VanderPlas, D. Laxalde, J. Perktold, R. Cimrman, I. Henriksen, E. A. Quintero, C. R. Harris, A. M. Archibald, A. H. Ribeiro, F. Pedregosa and P. van Mulbregt, *Nat. Methods*, 2020, **17**, 261–272.

15 Abraham. Savitzky and M. J. E. Golay, *Anal. Chem.*, 1964, **36**, 1627–1639.

16 A. Stankiewicz, *Materials*, 2024, **17**, 1527.

17 J. Song, N. Holten-Andersen and G. H. McKinley, *Soft Matter*, 2023, **19**, 7885–7906.

18 M. Baumgaertel and H. H. Winter, *Rheol. Acta*, 1989, **28**, 511–519.

19 C. Clason, *arXiv*, 2021, preprint, arXiv:arXiv:2001.00617, DOI: 10.48550/arXiv.2001.00617.

20 J. Honerkamp and J. Weese, *Macromolecules*, 1989, **22**, 4372–4377.

21 A. P. Valentine and M. Sambridge, *Geophys. J. Int.*, 2018, **215**, 1003–1021.

22 D. J. C. MacKay, *Neural Comput.*, 1992, **4**, 415–447.

23 C. R. Harris, K. J. Millman, S. J. van der Walt, R. Gommers, P. Virtanen, D. Cournapeau, E. Wieser, J. Taylor, S. Berg, N. J. Smith, R. Kern, M. Picus, S. Hoyer, M. H. van Kerkwijk, M. Brett, A. Haldane, J. F. del Río, M. Wiebe, P. Peterson, P. Gérard-Marchant, K. Sheppard, T. Reddy, W. Weckesser, H. Abbasi, C. Gohlke and T. E. Oliphant, *Nature*, 2020, **585**, 357–362.

24 T. Pandas development team, pandas-dev/pandas Zenodo 2025.

25 J. D. Hunter, *Comput. Sci. Eng.*, 2007, **9**, 90–95.

26 J. Kimmig, JulianKimmig/rheo_spec https://github.com/JulianKimmig/rheo_spec 2025.

27 C. Clason, *arXiv*, 2021, preprint, arXiv:arXiv:2001.00617, DOI: 10.48550/arXiv.2001.00617.

28 F. Neese, *WIREs Comput. Mol. Sci.*, 2022, **12**, e1606.

29 J. Steinmetzer, S. Kupfer and S. Gräfe, *Int. J. Quantum Chem.*, 2021, **121**, e26390.

30 P. Pracht, S. Grimme, C. Bannwarth, F. Bohle, S. Ehlert, G. Feldmann, J. Gorges, M. Müller, T. Neudecker, C. Plett, S. Spicher, P. Steinbach, P. A. Wesołowski and F. Zeller, *J. Chem. Phys.*, 2024, **160**, 114110.

31 C. Bannwarth, E. Caldeweyher, S. Ehlert, A. Hansen, P. Pracht, J. Seibert, S. Spicher and S. Grimme, *WIREs Comput. Mol. Sci.*, 2021, **11**, e1493.

32 M. K. Kesharwani, B. Brauer and J. M. L. Martin, *J. Phys. Chem. A*, 2015, **119**, 1701–1714.

33 A. S. Ivanov and V. S. Bryantsev, *Dalton Trans.*, 2016, **45**, 10744–10751.